CO_2 electroreduction on model catalyst surfaces

(PhD Thesis, September 2019)

Thomas Vagn Hogg

Supervisor: Professor Ib Chorkendorff

Co-Supervisors: Associate Professor Brian Seger and Senior Lecturer Ifan E.L. Stephens

Technical University of Denmark

Department of Physics

Section for Surface Physics and Catalysis (SurfCat)

Technical University of Denmark
Department of Physics
Section for Surface Physics and Catalysis (SurfCat)
Fysikvej, building 307
2800 Kongens Lyngby, Denmark

Abstract

The ongoing rise in global temperature and resulting change in climate strongly motivates discontinuing the combustion of fossil fuels as a source of energy. In place of fossil fuels, we need to transition to renewable energy sources such as solar, wind and hydro. Renewable energy sources are, however, intermittent in nature, necessitating the development and use of energy storage technologies. Electrochemical conversion of carbon dioxide into fuels and chemicals is one such technology and is the focus of this thesis. Chapter 1 is a general motivation for the use of electrochemical CO_2 reduction.

Chapter 2 is an overview of the CO_2 and CO electroreduction field with a focus on Cu and ends with listing areas in need of further investigation, motivating the work presented in the remainder of the thesis; i) a benchmark for CO reduction on polycrystalline Cu, so as to better understand the activity of nanostructured Cu catalysts, ii) the presence (if any) of oxidised phases on polycrystalline Cu during CO reduction conditions and surface reconstruction during reaction conditions, iii) the ability to track surface bound intermediates during CO_2 and CO reduction.

Chapter 3 deals with the experimental tools, methods and related theory used for the experiments described in the following chapters.

Chapter 4 deals with measuring CO reduction on planar polycrystalline Cu in 0.1 M KOH. Selectivity and activity were measured at -0.4, -0.50 and -0.59 V vs RHE using a combination of GC, HS-GC and NMR for analysis. Polycrystalline Cu was found to yield more than 50 % Faradaic efficiency towards CO reduction products, including high selectivity for C_2 and C_3 aldehydes and alcohols and ethene. Polycrystalline Cu was found to have an intrinsic activity comparable to nanostructured Cu catalysts (Cu nanoparticles and oxide-derived Cu), when normalised to electrochemically active surface area, despite the large difference in geometric current densities. Polycrystalline and nanostructured catalysts were seen to have a different selectivity which was attributed to the different potential windows

made available by the different roughness factors of the catalyst materials, increased readsorption and reduction of aldehydes in a porous structure, and the presence of undercoordinated sites. Issues with stability of activity and selectivity were also observed and were linked to Si from the glassware in alkaline conditions.

Chapter 5 describes experiments using grazing incidence X-ray diffraction (GIXRD) with synchrotron radiation to observe the reduction of the native oxide on a polycrystalline Cu thin film. The reduction was performed in Ar and CO saturated 0.1 M KOH in a spectroelectrochemical flow cell whilst monitoring the Cu(111) and Cu_2O(111) diffraction peaks on a 2-dimensional detector. Analysis indicated that all oxidised phases were reduced around +0.3 V vs RHE in a reductive scan. Additionally, there were indications of surface restructuring towards (100)-like facets when going to negative potentials in CO saturated electrolyte.

Chapter 6 uses attenuated total reflection surface enhanced IR absorption spectroscopy (ATR-SEIRAS) to track surface bound CO and other adsorbates at conditions relevant for CO_2 and CO reduction. CO reduction on Cu in 0.1 M $KHCO_3$ from 0.2 to -1.1 V vs RHE revealed record breaking intensities for the CO peak (0.056 a.u.). The CO peak was deconvoluted into two bands which were tracked as a function of potential from the initial adsorption of CO and to the band disappears again at the most cathodic potentials. The possible origins of the two band are discussed along with variations from other reported literature. CO was used as a probe molecule on Au to investigate the interaction of different electrolytes with the catalyst surface. Stronger competition for the surface in bicarbonate resulted in a vastly smaller potential window for adsorbed CO compared to perchlorates ($NaClO_4$, $HClO_4$). The combined use of ATR-SEIRAS and Pb UPD on Au revealed that the CO signal on Au is related to (211) and (110) type sites rather than the (111) facets.

Chapter 7 is a general conclusion. Areas in need of continued research and procedures for improved investigation are suggested.

The main results of chapters 4 and 5 have already been published as papers and these are attached in the appendix. Papers based on the content of chapter 6 are planned.

Resumé

Global opvarmning og resulterende klimaforandringer motiverer imod fortsat brug af fossile brændsler som energikilde. I stedet skal vi overgå til brug af fornybare energikilder så som sol, vind og vandkraft. Fornybare energikilder fluktuerer dog meget i mængden af energi de leverer, hvorfor de skal kombineres med energilagringsteknologier. Elektrokemisk reduktion af CO_2 til produktion af brændsler og kemikalier er et eksempel på en sådan teknologi og er emnet for denne afhandling. Kapitel 1 er en general motivation for brugen af elektrokemisk CO_2 reduktion.

Kapitel 2 er et overblik over feltet for CO_2 og CO elektroreduktion med et fokus på Cu og slutter af med at præsentere områder med behov for videre undersøgelse, hvilket leder til fokuspunkterne for resten af afhandlingen: i) et referencepunkt for CO reduktion på polykrystallinsk Cu som et sammenligningsgrundlag for nanostruktureret Cu, ii) tilstedeværelsen af oxiderede faser på polykrystallinsk Cu under reaktionsbetingelser samt restrukturering af overfladen under reaktionen, iii) at observere og følge adsorbater på overfladen under CO_2 og CO reduktion.

Kapitel 3 gennemgår de eksperimentelle værktøjer, metoder og tilhørende teorier som benyttes i eksperimenterne beskrevet i de efterfølgende kapitler.

Kapitel 4 omhandler CO reduktion på plant polykrystallinsk Cu i 0.1 M KOH. Selektivitet og aktivitet blev målt ved -0.4, -0.5 og -0.59 V vs RHE med en kombination GC, HS-GC og NMR til analyse. Polykrystallinsk Cu gav mere end 50 % Faraday effektivitet for CO reduktionsprodukter og havde høj selektivitet for C_2 og C_3 aldehyder og alkoholer samt ethen. Den intrinsiske aktivitet af polykrystallinsk Cu blev fundet sammenlignelig med nanostrukturerede Cu katalysatorer (Cu nanopartikler og OD-Cu), når den blev normaliseret til det elektrokemisk aktive overfaldeareal (ECSA), på trods af store forskelle i geometriske strømdensiteter. Forskelle i selektivitet mellem plant polykrystallinsk og nanostruktureret Cu blev forklaret ved: forskellige tilgængelige potentialevinduer for forskellige niveauer

af strukturering, forøget re-adsorption af aldehyder i en porøs struktur, og flere underkoordinerede sites for nanostrukturerede katalysatorer. Problemer med stabilitet af selektiviteten og aktiviteten blev forbundet med Si fra glasudstyret under basiske forhold.

Kapitel 5 omhandler eksperimenter med brug af grazing incidence røntgen diffraktion (GIXRD) med en synkrotron kilde til at observere reduktionen af det naturlige overfladeoxidlag på en polykrystallinsk Cu tyndfilm. Reduktionen blev udført i Ar eller CO mættet 0.1 M KOH i en spektroelektrokemisk flowcelle mens diffraktionssignalerne fra Cu(111) og Cu_2O(111) blev opfanget på en 2-D detektor. Målingerne indikerede at alle oxiderede faser blev reduceret omkring +0.3 V vs RHE i et reduktivt scan. Der var også tegn på restrukturering af overfladen mod (100)-lignende facetter ved negative potentialer i CO mættet elektrolyt.

Kapitel 6 omhandler brug af IR teknikken attenuated total reflection surface enhanced infrared absorption spectroscopy (ATR-SEIRAS) til at følge overfladebundet CO og andre adsorbater under CO og CO_2 reduktionsbetingelser. CO reduktion på Cu i 0.1 M $KHCO_3$ mellem +0.2 og 1.1 V vs RHE viste et rekordhøjt signal for CO båndet (0.056 a.u.). CO båndet blev dekonvuleret til to separate bidrag som blev fulgt som en funktion af potentialet fra de først viste sig og til de forsvandt igen ved de mest negative potentialer. Den mulige baggrund for de to bånd, samt afvigelser fra tidligere litteratur blev diskuteret. CO blev brugt som en probe på Au for at undersøge interaktionen mellem overfladen og forskellige elektrolytter. Højere konkurrence om overfladen i $KHCO_3$ resulterede i et meget snævert vindue for adsorberet CO i forhold til i $NaCO_4$ og $HClO_4$. En kombination af ATR-SEIRAS og Pb UPD på Au viste at CO signalet på Au er relateret til (211)- og (110)-lignende sites og ikke (111) facetten.

Kapitel 7 er en general konklusion. Områder med mulighed for videre forskning og forbedrede procedurer diskuteres.

De primære resultater fra kaptitel 4 og 5 er allerede publiceret og artiklerne er medtaget i appendikset. Artikler baseret på indholdet i kapitel 6 er planlagt.

Preface

This thesis was part of the requirement for attaining a **Doctor of Philosophy** in **Physics** from the **Technical University of Denmark** (DTU). The work was carried out at the Department of Physics, Section for Surface Physics and Catalysis (SurfCat), over 3 years between September 2016 and August 2019, under supervision of Professor Ib Chorkendorff, Associate Professor Brian Seger and Senior Lecturer Ifan E.L Stephens (Ifan formerly held a position as Associate Professor at DTU Physics but moved to Imperial College London in the summer of 2017).
The project at SurfCat was funded through grant 9455 from VILLUM FONDEN through the VILLUM Center for the Science of Sustainable Fuels and Chemicals (V-SUSTAIN).

I would like to thank:

All of my supervisors; Ib, Brian and Ifan, for their guidance and availability for discussions throughout the project.

Erlend Bertheussen for mentoring me in the first part of my PhD. All the other CO_2 reduction people formerly and currently at SurfCat; Thomas Maagaard, Scott, Stefano, Albert, Gaston, Ezra, Ming, Frederik and Degenhart for great discussions, assistance and in some cases collaborations, and Anna for being an understanding office mate. The floor managers; Brian, Patrick, Kenneth and Robert for keeping everything running smoothly and always being ready to help. Everyone else at SurfCat for delivering a sound mixture of good science and good times. The CatTheory people; Hendrik, Henrik and Sudarshan for preliminary discussions on IR. Johan for a great collaboration during his Bachelor's project. The workshop crew, particularly Dan and Peder, for a vast number of electrochemical cells.

Professor Yang Shao-Horn for guidance during my stay at MIT, Yu Katayama for teaching me all things SEIRAS, and the rest of the Electrochemical Energy Lab for

making my time in Boston memorable.

All our collaborators at Stanford, particularly John and Alan for collaboration on the synchrotron project.

My friends and family for their continued support.

Thomas Vagn Hogg

September 1st, 2019

Contents

Chapter 1

Introduction

In the introduction I will motivate the use of electrochemical reduction of CO_2 as a means of producing fuels and chemicals from renewable energy. I end by giving a short overview of the structure of the thesis.

1.1 The energy challenge

We are experiencing a continuous increase in energy demand, a demand met mainly through the use of fossil fuels. The associated rise in atmospheric CO_2 levels has been linked to an increase in global temperature and resulting change in climate. This strongly motivates the discontinuation of fossil fuel combustion as a source of energy. We need to exchange fossil fuels for renewable energy sources such as solar, wind and hydro. Renewable energy sources must be combined with energy storage technologies to buffer their inherently intermittent energy supply. Electrochemical conversion of carbon dioxide into fuels is an example of such a storage technology.

In the following I will discuss the background of the problem, how we may solve it, and what part electroreduction of CO_2 can play.

1.1.1 Higher energy demand due to higher standard of living

Figure 1.1 shows the annual CO_2 emissions per person per year vs annual income for the countries of the world, both on logarithmic scales. A clear connection is seen between wealth of a country and the level of CO_2 emissions (or alternatively energy usage). The colour scale indicates the human development index (HDI) - a combined measure of economic wealth, educational level and life expectancy.

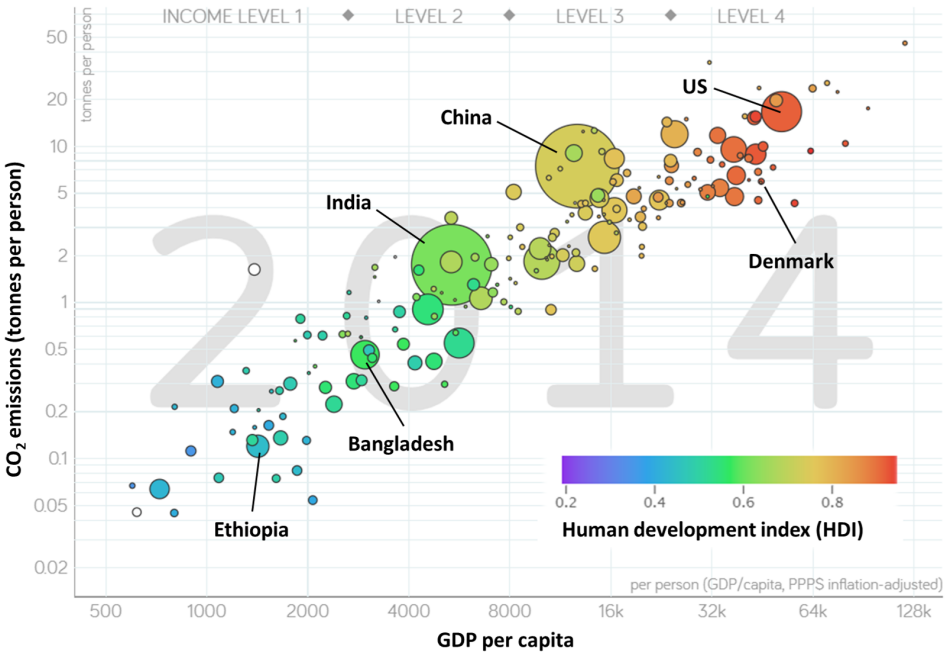

Figure 1.1: Log-log plot of CO_2 emissions vs income for countries of the World in the year 2014. Bubble-size indicates number of inhabitants. Colour mapping indicates level on Human Development Index (HDI) scale. Made using Gapminder Tools.

The HDI clearly scales with income (one of the three HDI metrics) but variations indicate that economic wealth is not the only determining factor for prosperity. The graph is for 2014. Comparing similar graphs from preceding years indicates a clear trend of countries moving from the lower left hand corner of low wealth and low CO_2 emissions towards the upper right hand corner with increased wealth and increased CO_2 emissions. A higher standard of living is clearly linked to higher energy consumption. Thus, as the population of the World both increases in size and attains higher standards of living, we face an increasing need for energy, and as a result, an increasing issue of emissions as long as we rely mainly on fossil fuels. Particularly, the increased standard of living of countries with large populations such as India and China pose an issue as their energy demand is expected to follow in light of the current trend. There is, however, also a trend towards decoupling of economic growth and energy usage as the worlds GDP is increasing compared to energy use, indicating that lower energy use will not necessarily lower our economic development [1, 2].

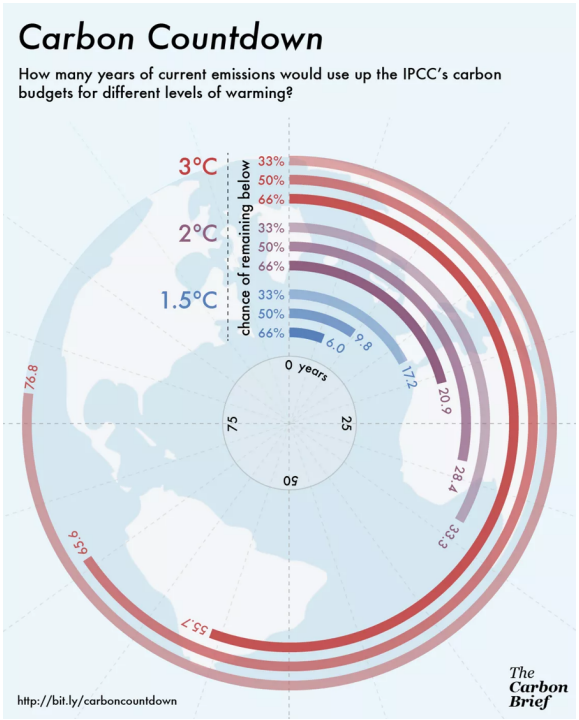

Figure 1.2: Years remaining since 2014 at 2014 emission levels before a certain temperature is reached. Percentages indicate the probability of staying below the indicated temperature. http://bit.ly/carboncountdown.

1.1.2 Resulting rise in CO_2 levels and global warming

CO_2 levels have increased from 227 ppm in 1750 to 405 ppm in 2017 [3]. The effect of CO_2 emissions on the temperature increase are usually measured compared to pre-industrial levels (1850-1900). The 2018 report from the IPCC states that the temperature increase is around 1.0 ± 0.2 °C [4]. We have emitted 2200 ± 320 $GtCO_2$ by the end of 2017 since the pre-industrial period. Depending on the model used, the remaining carbon budget for a 1.5 °C goal is between 420-570 $GtCO_2$ for 66 % confidence. We are currently using 42 ± 3 $GtCO_2$/yr. An idea of how long we can maintain current emissions and stay below a certain temperature is illustrated in Figure 1.2, also based on IPCC projections. If we use up the the full amount of fossil fuels available (5 GtC, lower estimate) we can expect an temperature increase between 6.4-9.5 °C on average and between 14.7-19.5 °C in Arctic regions [5].

1.1.3 How can we mitigate the emission problem?

In order to close the anthropogenic carbon cycle we must remove the same amount of greenhouse gasses as we emit [3]. We must, however, also reduce the current levels that are already causing a rise in the global temperature. Strategies include transitioning away from fossil fuels and towards renewable energy sources such as solar, wind, hydro, geothermal, etc. as well as nuclear energy [6]. Additionally, we require carbon capture and sequestration to lower the CO_2 levels in the atmosphere [7, 8]. Underground storage in geological formations has been suggested [9].

1.1.4 The need for energy storage

An increase in the use of renewable energy will be followed by an issue of stability in supply due to the intermittent nature of renewables. It is necessary to store energy when excess is being produced and to use from these stores when production is low. This can happen on different time scales from hours to seasons. Some energy storage systems include mechanical storage such as pumped hydro, direct thermal storage, battery storage, and electrochemical energy storage through the use of electrolysers [10–12]. The last form of energy storage, electrochemical energy storage, and in particular through co-electrolysis of CO_2 and water, is the technology of interest in this thesis.

1.2 Reduction of CO_2 to fuels and chemicals

The theory behind CO_2 reduction will be introduced in the next chapter. A general scheme for co-electrolysis of water and CO_2 to form hydrocarbons and oxygenates is illustrated in Figure 1.3. An example of a hypothetical energy society with a closed carbon cycle is pictured in Figure 1.4. Here CO_2 reduction is part of a larger electrochemical synthesis framework working together with renewable energy. Particularly, industrial point sources of CO_2, such as concrete and steel, which could be continued even after fossil fuel combustion has stopped, would be suitable for CO_2 reduction. We see that in the case of Figure 1.4, CO_2 reduction has not been emphasised as an energy storage technology, but rather as a means for producing fuels and chemicals. The reason for continued use of carbon based fuel for transportation is due to the high energy density compared to other technologies such as batteries and hydrogen [6]. Thus, long range transportation and the aviation sector could still require carbon based fuels. The other possibility, as also shown in Figure 1.4, is the production of chemicals. From a purely economic standpoint, a techno-economic analysis shows that the current market is mainly open for the use of electrochemical CO_2 reduction towards chemicals, as it is not

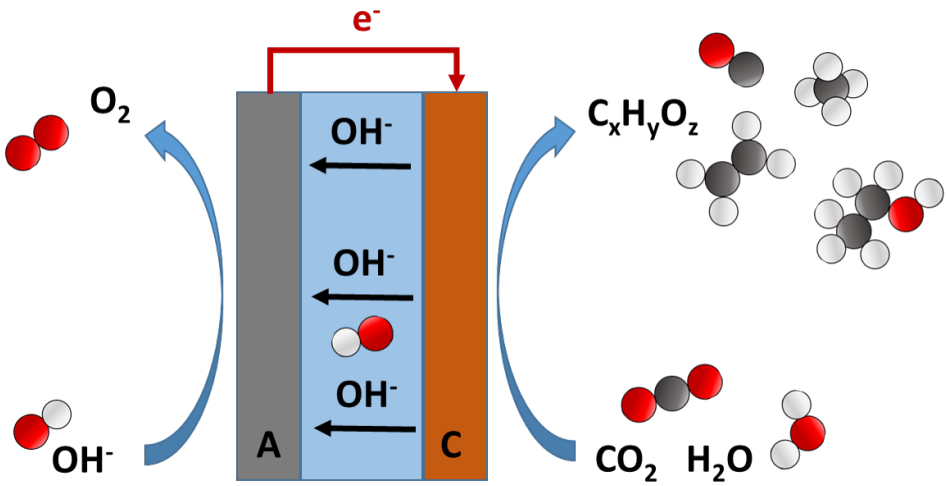

Figure 1.3: General scheme for electrochemical CO_2 reduction. Shown here with an anion exchange membrane separating the anode (A) and cathode (C). Oxygen evolution is the balancing reaction.

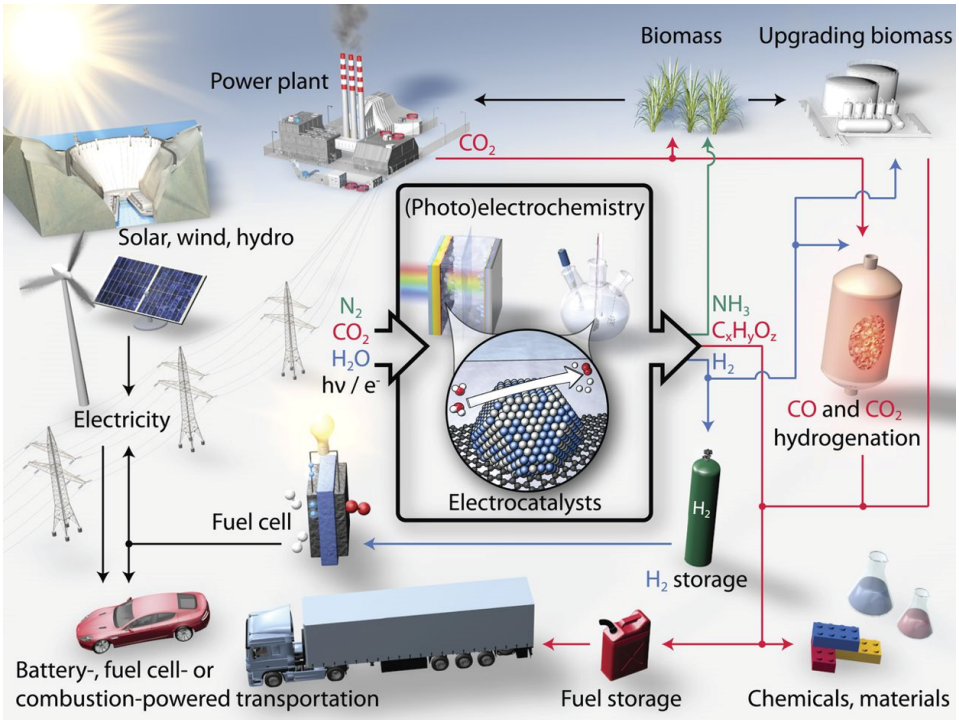

Figure 1.4: Illustration of a scheme for a closed carbon cycle [13, Figure 1].

currently possible to compete on price with fossil fuels [14]. Thus, CO_2 reduction to valuable chemicals such as ethene, a precursor for the polymer industry, could be a means of entry of the CO_2 reduction technology onto the market, inciting further research and development. In general, an electrolysis technology will be very dependent on the price of electricity and in this case the price of renewable electricity. The price of renewable electricity is fortunately continually decreasing [15]. A recent study has also shown that the energy-return-on-investment ratios of oil, coal and gas are quite low at the final stage of use when the full supply chain is considered, making renewable energy more competitive than previously believed [16].

In summary, electrochemical reduction of CO_2 can work as part of a larger renewable energy system with a closed carbon cycle. In order to improve both the selectivity and activity of the reaction we must have a better fundamental understanding of the electrocatalytic process. An attempt at improving this understanding is presented in this thesis through the combination of experimental techniques looking at products, catalyst surface, and adsorbed intermediates.

1.3 Thesis structure

This thesis consists of 7 chapters. Chapter 1 is the introduction and motivation for the project. Chapter 2 introduces the field of electrochemical CO_2 reduction and identifies focus-points for research used in the project. Chapter 3 deals with all the experimental methods used throughout the project. The following 3 chapters correspond to the 3 main groupings of research conducted, all related to CO and CO_2 reduction on polycrystalline Cu. Chapter 4 describes the selectivity and activity of polycrystalline Cu for electroreduction of CO at low overpotentials. Chapter 5 deals with in situ grazing incidence XRD of polycrystalline Cu during CO reduction. Chapter 6 describes work on attenuated total reflection-surface enhanced infrared absorption spectroscopy (ATR-SEIRAS) of CO_2 and CO reduction on Cu and Au films. Chapter 7 is a general conclusion.

Chapter 2

Electrochemical CO_2 reduction

This chapter introduces the field of electrochemical CO_2 reduction at its current state with a main focus on Cu as a catalyst. The field is continually advancing and is reaching technological relevance. This is by no means intended as a complete summary, but introduces the reader to the broad strokes and focuses on themes relevant for the research presented in later chapters.

2.1 Products from CO_2 reduction on metals

CO_2 can be electrochemically reduced producing hydrocarbons and oxygenates. The range of possible products depends on the catalytic material. Various transition metals were tested for their selectivity by Hori and coworkers in the 80'ies (see Table 2.1) [17]. It is clear that the metals can be placed in different groups based on their selectivity.

- Pb, Hg, Tl, In, Sn, Cd: $HCOO^-$.
- Au, Ag, Zn, Pd, Gd: CO.
- Cu: CH_4, C_2H_4 and alcohols
- Ni, Fe, Pt, Ti: H_2

Cu is seen to be the only metal capable of effectively reducing CO_2 beyond CO, that is reactions requiring the transfer of more than two electrons. This fact has made Cu the most investigated metal for CO_2 reduction. A thorough study by Kuhl et al. of the product distribution for CO_2 reduction on Cu showed that a wide range of products could be formed as seen in Table 2.2 [18].

Metal	E [V vs RHE]	J_{total} [mA/cm^2 geo]	CH_4 [%]	C_2H_4 [%]	EtOH [%]	PrOH [%]	CO [%]	$HCOO^-$ [%]	H_2 [%]	Total [%]
Pb	−1.24	−5.0	0	0	0	0	0	97.4	5.0	102.4
Hg	−1.12	−0.5	0	0	0	0	0	99.5	0	99.5
Tl	−1.21	−5.0	0	0	0	0	0	95.1	6.2	101.3
In	−1.16	−5.0	0	0	0	0	2.1	94.9	3.3	100.3
Sn	−1.09	−5.0	0	0	0	0	7.1	88.4	4.6	100.1
Cd	−1.24	−5.0	1.3	0	0	0	13.9	78.4	9.4	103.0
Au	−0.65	−5.0	0	0	0	0	87.1	0.7	10.2	98.0
Ag	−0.98	−5.0	0	0	0	0	81.5	0.6	12.4	94.6
Zn	−1.15	−5.0	0	0	0	0	79.4	6.1	9.9	95.4
Pd	−0.81	−5.0	2.9	0	0	0	28.3	2.8	26.2	60.2
Ga	−0.85	−5.0	0	0	0	0	23.2	0	79.0	102.0
Cu	−1.05	−5.0	33.3	25.5	5.7	3.0	1.3	9.4	20.5	103.5
Ni	−1.09	−5.0	1.8	0.1	0	0	0	1.4	88.9	92.4
Fe	−0.52	−5.0	0	0	0	0	0	0	94.8	94.8
Pt	−0.68	−5.0	0	0	0	0	0	0.1	95.7	95.8
Ti	−1.21	−5.0	0	0	0	0	tr.	0	99.7	99.7

[a]The potential has been converted from the reported SHE potential to the RHE scale [T=18.5 °C, pH=6.8] by adding $(RT/F)\ln(10)\text{pH} = 0.39$ V.

Table 2.1: Product distribution for CO_2 reduction on metals in 0.1 M $KHCO_3$. Table adapted from [19]. Data from [17].

Cu thus has the catalytic capacity for producing a range of hydrocarbons and oxygenated organics which could be used as either fuel or chemicals for synthesis. Attaining a selectivity for any single compound is, however, challenging due to the close standard reduction potentials [18, 20, 21].

Product	# e⁻	E	Product	# e⁻	E
Formate 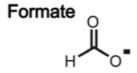	2	−0.02	Acetaldehyde 	10	0.05
Carbon monoxide 	2	−0.10	Ethanol 	12	0.09
Methanol 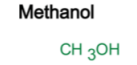	6	0.03	Ethylene 	12	0.08
Glyoxal 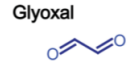	6	−0.16	Hydroxyacetone 	14	0.46
Methane 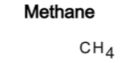	8	0.17	Acetone 	16	−0.14
Acetate 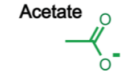	8	−0.26	Allyl alcohol 	16	0.11
Glycolaldehyde 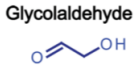	8	−0.03	Propionaldehyde 	16	0.14
Ethylene glycol 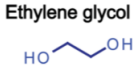	10	0.20	1-Propanol 	18	0.21

Table 2.2: Products for CO_2 reduction on polycrystalline Cu in 0.1 M $KHCO_3$. The number of electrons for the reaction and the equilibrium potential at pH 6.8 is given. Table from [18].

2.2 Theoretical view of electrocatalysis for CO_2 reduction

Using theoretical computations (DFT), Bagger et. al illustrated that the selectivity of different products for CO_2 reduction can be explained by the binding energy of reaction intermediates on the various metals [22]. Cu has a unique binding energy for for the intermediates *CO and *H which has been illustrated by Bagger et al. and shown in Figure 2.1. They argued that Cu is seen to be the only metal that binds CO and does not exhibit underpotential deposited hydrogen. The metals that exhibit underpotential deposition of hydrogen produce hydrogen, those with

H adsorbed at CO_2 reduction potentials form mainly CO, and those with very low or no H adsorbed at CO_2 reduction potentials produce formate.

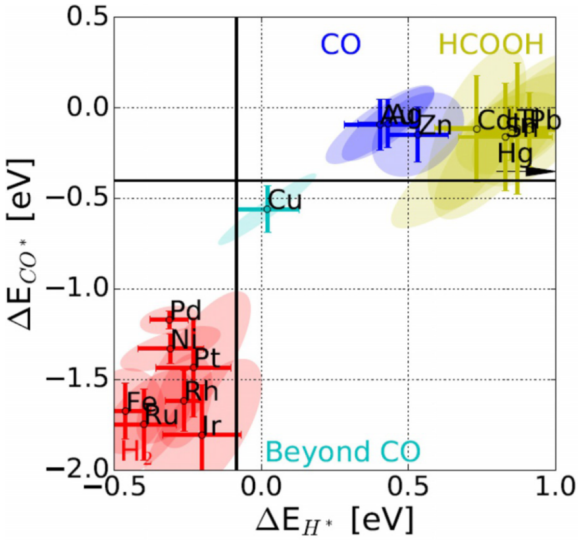

Figure 2.1: Grouping of metals by their binding energy for adsorbed *H and *C. Red group forms hydrogen, blue forms CO, yellow forms HCOOH and turquoise (Cu) goes beyond CO. Black lines indicate the thermodynamics for adsorbing CO and hydrogen. From [22, Figure 4]

The above concept illustrates a complicated dependence on binding energy of different reaction intermediates. A simple version of an electrochemical reaction with only one intermediate and two electrons transferred, is the hydrogen evolution reaction (HER).

$$2H^+ + 2e^- \rightarrow H_2(g) \tag{2.1}$$

For this simple case, the result is an activity volcano as a function of the energy of adsorption of H, as seen in Figure 2.2. The logarithm of the current density has a triangular dependence on the adsorption energy and is seen to be maximised when the adsorption energy is close to zero. The effect is qualitatively explained by the Sabatier principle where the intermediate must have intermediate binding on the catalyst in order to have the reactant bind to the surface followed by reaction and then let the product leave the surface again. Too weak binding will not allow the reactant to adsorb. Too strong bind will not allow the product to desorb. The same principle can be shown for the required overpotential for the reaction, where zero overpotential is theoretically achievable at zero binding energy [24].

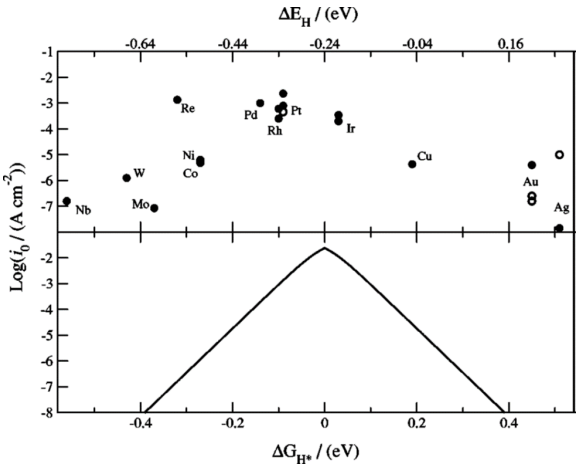

Figure 2.2: Top: Experimental exchange current densities for transitions metals as a function of binding energy, ΔE_{H*}. Prediction of exchange current density as a function of the free energy of hydrogen adsorption, ΔG_{H*}, based on a kinetic model. The authors applied the relationship $\Delta G_{H*} = \Delta E_{H*} + 0.24$. From [23, Figure 1].

For more advanced reactions with multiple electron transfers and intermediates, the optimisation problem becomes multidimensional. The binding energy of the various intermediates cannot in general be changed independently due to scaling relations and hence more advanced reactions have thermodynamic overpotentials [24, 25]. Requiring that every step in a reaction must be exergonic, and assuming that each reaction step is made up of a combined proton and electron transfer (the computational hydrogen electrode [26]), the potential required can be calculated with DFT. An example of the scaling relations and resulting theoretical overpotentials is given for CO_2 reduction to methane on transition metals in Figure 2.3. The difference between the equilibrium potential and the potential for making the most unfavourable step exergonic is seen to give the theoretical or thermodynamic overpotential. In this case the potential limiting reaction was seen to be the coupled proton electron transfer to *CO to form *CHO.

The above discussion has neglected the activation barriers for each reaction step and thus an accurate estimate of the kinetics of the reactions. In general, the computations rely strongly on the theoretical assumptions made and the inherent simplifications. Explicit modelling including solvation effects using water and ions is necessary to get closer to an accurate representation of the electrochemical interface during reaction conditions. This should also be coupled with a model of the transport phenomena relevant for the experimental situation used for comparison. A recent discussion and comparison of the various findings from

computational studies of CO_2 reduction on Cu can be found in [19].

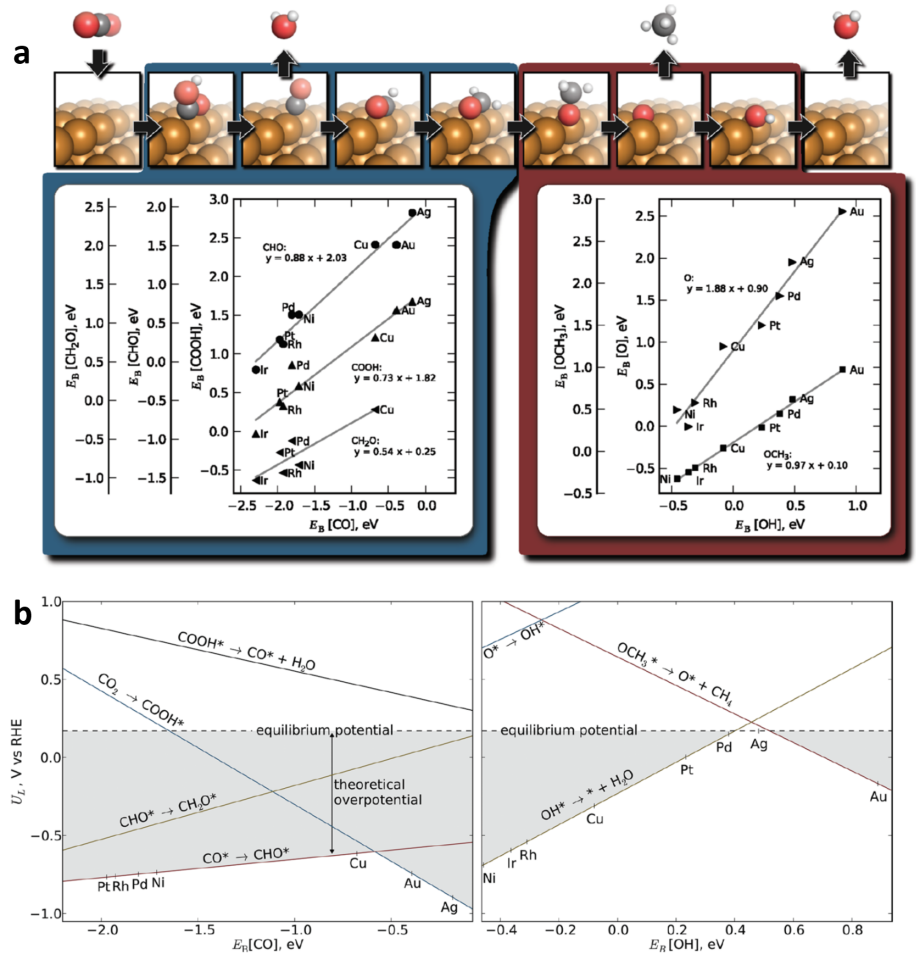

Figure 2.3: a) Scaling relations for intermediates in the reduction of CO_2 to methane on fcc (211) transition metals. b) The resulting thermodynamic overpotentials. From [27, Figures 1 and 2].

2.3 Facets

As the binding energies of intermediates are dependent on the metal, they are also dependent on the surface facet. Studies on single crystals reveal the facet dependence on product selectivity, indicating which sites on polycrystalline materials are active for specific products. The selectivity on Cu single crystals has

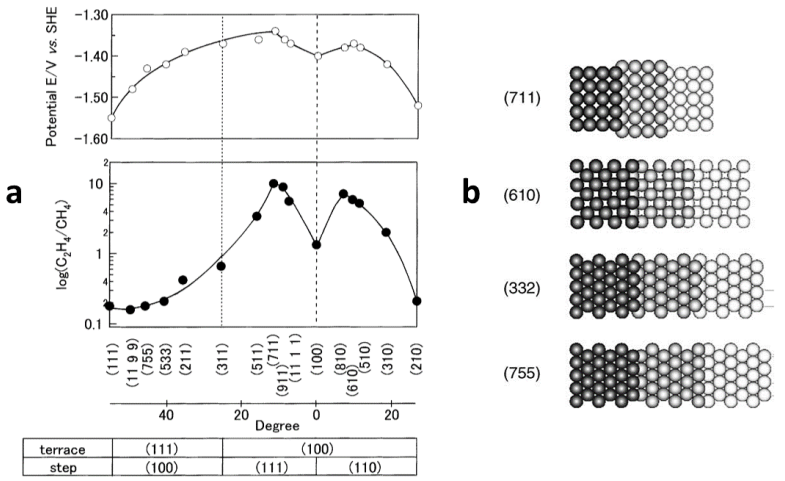

Figure 2.4: a) Relative selectivity of single crystal facets for ethene and methane. Top panel shows the potential required for 5 mA/cm^2, middle panel the log(FE(C_2H_4)/FE(CH_4)) Bottom indicates the orientation relative to (100) and the make-up of the single crystals in terms of terrace and step types. b) Examples of stepped single crystal structures. From [28, Figures 4 and 5].

been investigated by Hori et al. [28]. They compared the different crystals by their relative selectivity for methane and ethene at a fixed current density of 5 mA/cm^2 as shown in Figure 2.4. The (100) facet was seen to have high selectivity for ethene and some for methane. Introduction of (100) or (110) steps between the (100) terraces yielded increased selectivity for for ethene and lower selectivity for methane. The (111) facet mainly yielded methane with some increase in selectivity by introduction of (100) steps. The n(111)-(111) crystal series had high selectivity for multicarbon products and the (110) = 2(111)-(111) had specifically high selectivity for oxygenates (acetate, ethanal and ethanol). A study by Huang et al. varied the potential on Cu single crystals and observed a tendency towards higher methane selectivity at more negative potentials [29].

2.4 Restructuring

The surface orientation of polycrystalline Cu has been observed to change during CO_2 reduction relevant conditions. Kim et. al reported the stepwise conversion from polycrystalline Cu to Cu(111) and then Cu(100) over a period of an hour in both Ar-purged 0.1 M KOH and N_2-purged 0.1 M $KHCO_3$ at -0.9 V vs SHE with EC-STM [30, 31]. Interestingly Cu(110) was also seen to reconstruct whereas

Cu(111) and Cu(100) single crystals remained stable [32]. Additionally, in gas phase STM a Cu(111) surface has been seen to be activated by CO leading to the formation of Cu clusters moving on the surface [33]. This indicates that the presence of CO could also cause restructuring in aqueous environments or increase the rate through increased surface mobility. Knowing the true surface structure and composition during operation is of prime importance to understanding electrocatalysis and emphasises the need for surface sensitive in situ techniques.

2.5 CO as an intermediate and CO reduction

It was found quite early that CO is a surface bound intermediate and that the reduction of CO on Cu leads to many of the same products as for CO_2 reduction [34–36]. This is also supported by IR spectroscopic studies of CO on Cu as explained in detail later. As discussed earlier, the specific binding energy of CO (and H) on Cu is what seems to make it active for further reduction of CO. The introduction of CO is also seen to lower the HER activity compared to Ar-purged solutions due to CO adsorption on the active sites [37]. Lower HER will effectively cause a higher Faradaic efficiency for CO_2 or CO reduction although the CO_2 or CO reduction activity is not necessarily enhanced. Products from CO reduction are generally formed at similar potentials as the same products from CO_2 reduction on the SHE scale [38] (see section on pH below). In terms of research, the reduction of CO can be used to study CO_2 reduction with a lower amount of reaction steps to gain better fundamental understanding of the reaction pathway. Decoupling of the reduction of CO_2 to CO and further reduction of CO to more reduced compounds could also be of practical viability. Such a tandem approach could be imagined where a catalyst with high efficiency for CO_2 reduction to CO (e.g. Zn, Au or Ag) is used in the first step and Cu is used for the further reduction of CO [39]. The concept has been shown to work with Au nanoparticles on Cu foil which yielded higher C2+ selectivity at lower overpotentials [40]. CO_2 reduction on connected nanoparticles of Cu and Ag, referred to as nanodimers, also showed increased ethene selectivity compared to the separate particles, illustrating the same synergistic concept [41].

2.6 Effect of pH

The HER activity is dependent on the potential on the reversible hydrogen scale, where the proton activity of the electrolyte is taken into account. Some CO_2 reduction products are not dependent on the RHE scale, however, but depend on an absolute potential scale such as the standard hydrogen scale, SHE. Hori et al.

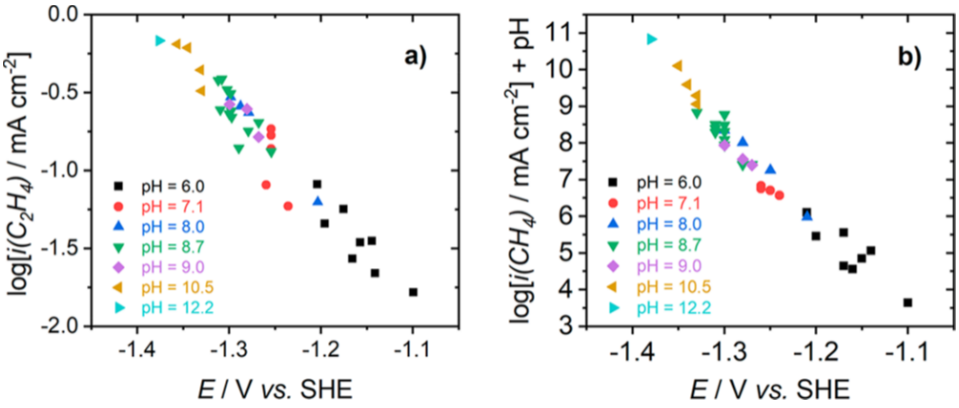

Figure 2.5: a) The activity of CO reduction to ethene vs SHE potential. b) The activity of CO reduction to methane corrected for pH vs SHE potential. Experiments performed in different pH buffered electrolytes. Figure from [19, Figure 9], data from [36].

observed that ethene and ethanol were independent of proton activity whereas methane was dependent [36]. This is illustrated in Figure 2.5. Notice that the pH dependence of methane is included in the y-axis definition in subfigure b. The explanation given was that the rate determining step involved protons for methane but not for ethene and ethanol. It has also later been shown computationally that the C-C coupling barrier for forming multicarbon compounds is lowered with more negative potential on the SHE scale [42, 43]. This effectively means that the HER activity on a material can be controlled independently of the CO_2 reduction activity by maintaining a fixed potential vs SHE but changing the pH, so as to change the RHE potential. It is generally attempted to conduct CO_2 reduction in alkaline environments for this reason. Due to the acidic nature of CO_2 in aqueous media, it will generally neutralise the alkaline environment. This can be mitigated in gas diffusion electrodes where the CO_2 is fed to the electrode as gas and not allowed to be hydrated before reaction. pH change is not an issue for CO reduction. CO_2 has a higher solubility than CO and thus it is beneficial to use CO_2 to get higher mass transport.

In general, whenever an electron is transferred in a CO_2 reaction an OH^- is usually produced [17], resulting in a higher local pH at the electrode surface. This can be particularly extreme for GDE type cells with high current densities. The pH at the electrode surface during CO_2 reduction was modelled by Gupta et al. who found it to be dependent on buffer capacity of the electrolyte, degree of mixing (boundary layer thickness), and current density [44].

2.7 Planar vs nanostructured

The intrinsic activity of a catalyst is better understood on a planar model surface where the transport limitations are minimised. Nanostructured catalysts with their high surface area are however required for real operation in order to maximise geometric current density and hence product formation. Nanostructuring has shown to also yield a different product distribution than flat electrodes [45–48], with a tendency towards higher C2+ production. Using oxide derived Cu (OD-Cu), formed by initial oxidation and following reduction, Kanan and coworkers showed high efficiency towards ethanol for CO reduction in 0.1 M KOH at low overpotentials (>50 % FE for ethanol at -0.3 V vs RHE) [49]. They also showed that OD-Au exhibited almost exclusive selectivity for CO from CO_2 reduction at low overpotentials and showed a different Tafel slope than planar Au, which was attributed to a stabilised intermediate [50]. They attributed the difference in selectivity, compared to planar equivalents, to the increased presence of grain boundaries and surface terminations [51]. In a collaboration between our group and Kanan's we reported the presence of particularly strong binding sites on OD-Cu for CO and correlated their presence with the CO reduction activity [52]. A good benchmark for CO reduction on planar Cu is required to estimate the effect of nanostructuring on the intrinsic activity of Cu.

2.8 Subsurface oxygen

There is an ongoing discussion in the CO_2 reduction field about the potential presence of subsurface oxygen and the role it plays for the catalytic activity of Cu. Particularly, in relation to various forms of OD materials. Generally, however, the standard potentials for reduction of oxidised phases are anodic of the CO_2 and CO reduction reactions, such that the oxidised phases should have been reduced at potentials relevant for CO_2 and CO reduction [19]. Table 2.3 shows the standard potentials for reduction of some oxides and for some CO reduction reactions. Experimental indications of oxygen at or close to the surface have been reported during reaction conditions [46, 47, 55, 56] and a promotional effect on the CO_2/CO reduction reactions has been argued on the basis of DFT calculations [55–57]. Reports arguing against the presence of oxygen at or near the surface at reaction conditions include an experiment using isotope labelling [58], a Raman study [59] and DFT calculations [59, 60]. Further investigations under well defined conditions are clearly required.

Half-cell reaction	U°_{RHE} / V
$CuO + 2\,(H^+ + e^-) \longrightarrow Cu + H_2O$	0.56
$Cu(OH)_2 + 2\,(H^+ + e^-) \longrightarrow 2\,Cu + 2\,H_2O$	0.53
$Cu_2O + 2\,(H^+ + e^-) \longrightarrow 2\,Cu + H_2O$	0.46
$2\,CO + 6\,(H^+ + e^-) \longrightarrow CH_3CHO(aq) + H_2O$	0.19
$2\,CO + 8\,(H^+ + e^-) \longrightarrow CH_3CH_2CHO(aq) + H_2O$	0.19
$2\,CO + 8\,(H^+ + e^-) \longrightarrow C_2H_4(g) + 2\,H_2O$	0.17

Table 2.3: Standard potentials for reduction of select oxidised phases of Cu and for reduction of CO to important products. Calculated with thermochemistry data from [53, 54].

2.9 Towards practical application

In order to attain sufficient production rates for commercial use, the mass transport limitations observed at relatively low current densities in a model electrochemical cell must be overcome. This has been achieved in the same fashion as for the HER, in an electrolysis cell using gas diffusion electrodes. The delivery of the reactant as a gas extensively lowers the issues of gas solubility and slow diffusion. High current densities and Faradaic efficiencies have been attained for example for ethene (60-70 % FE between 275 and 750 mA/cm^2) [61]. Substantial improvements are still required in optimisation of the complex interconnected processes in a GDE type reactor for CO_2 reduction, as well as increased operational stability [62]. Reviews on the area can be found in [62, 63].

2.10 Infrared spectroscopy

In the following a short review is given of the literature relating to infrared absortion studies on Cu and Au of relevance for electrochemical CO_2 and CO reduction and with particular focus on ATR-SEIRAS studies. Infrared absorption spectroscopy and ATR-SEIRAS are described in Section 3.5.

2.10.1 Cu

There have been extensive studies of CO on single crystal and polycrystalline Cu in vacuum using infrared reflection absorption spectroscopy, IRRAS [64–67].
Investigating CO and CO_2 reduction by means of IR has been of interest since the beginning of CO_2 reduction studies. Particularly, Hori and coworkers have published a number of papers using FTIR in the external reflection mode to monitor CO and other adsorbates during CO_2 and CO reduction on Cu [68–73].

These studies were performed on both polycrystalline and single crystal Cu. They were conducted by pressing the crystal electrodes against an IR window to minimise the attenuation due to the electrolyte (IRRAS). The measurement procedure applied is termed SNIFTIRS (subtractively normalised FTIR spectroscopy), where the spectra at a reference potential are subtracted from spectra at a potential of interest. IRRAS experiments generally give a lower signal than SEIRAS as there is usually no surface enhancement but can be performed with single crystals which is not possible for SEIRAS as it is dependent on a nanostructured surface. The FTIR measurements in the external reflection mode also have issues with the thin layer geometry causing transport limitations which is not an issue for SEIRAS [74].
Studying CO and CO_2 reduction with ATR-SEIRAS on Cu has received a lot of attention recently. It was initiated by being able to synthesise Cu films on first Ge [75] and then Si [76] internal reflection elements (IREs), where adsorbed CO was observed. The first extensive study of CO_2 reduction on Cu using ATR-SEIRAS came from the group of Xu [77] in 2016. They electrodeposited Cu on an electroless deposited Au film. This was closely followed by the group of Surendranath (in collaboration with Osawa's group) [78] who applied a Cu electroless procedure. Several studies of CO_2 reduction on Cu using this electroless Cu procedure have been reported by the group of Waegele [79–81].
The above studies have mainly tracked the CO band. A few studies have reported other surface bound intermediates from CO_2 reduction using IRRAS [82] and SEIRAS [83].

2.10.2 Au

Au has received less attention than Cu using IRRAS in vacuum due to the low absorption energy of CO on Au [84].
For ATR-SEIRAS on Au, vacuum evaporated Au films have been utilised and it was shown how these could also be flame annealed to yield a more (111) like surface [85]. An electroless deposition method was also reported [86]. A similar electroless method was employed for studying CO_2 reduction by the groups of Surendranath [87, 88] and Xu [89–91]. It should be noted that the group of Surendrananth has repeatedly reported CO bands in the 2000-1800 cm^{-1} range which they attributed to a bridge bound CO. The group of Xu did not observe these bands on pure Au but were able to replicate them by the use of a Pt counter electrode, thus indicating that they were probably related to poisoning of the Au electrode by foreign metal atoms [91].
An interesting feature when performing CO_2 reduction on Au is that the product, CO, cannot be observed at the potential where it is produced, as it immediately

desorbs. This issue was circumvented by the use of a potential stepping procedure, producing CO at negative polarisation and then stepping more positive to observe the produced CO. Dunwell et al. described this stepping procedure and used it to estimate the catalytic performance of Au for the CO_2 to CO reaction [89]. They also observed an exponential decrease in CO signal after the step, which was attributed to the CO diffusing away. CO will not stay adsorbed on a Au surface unless there is a local pressure of CO. Dunwell et al. additionally illustrated the effect of increased mixing by showing that CO_2 could reach the electrode surface with high enough convection. This was explained by the relatively slow conversion of CO_2 to bicarbonate and hence illustrated a non-equilibrium situation [90]. The same study investigated the local pH by the ratio of the carbonate and bicarbonate bands, a method previously suggested Ayemoba et al. [92].

2.10.3 Issues with observing bands at low wavenumbers

Usually, in ATR-SEIRAS the low wavenumber region (<1200 cm^{-1}) is not available when using Si IREs. This is due to the high absorption of Si in these regions. Some studies have used a sandwich configuration, combining a thin Si wafer with a less absorbing ZnSe IRE [83, 93–95]. This is discussed further in Section 6.5.2.

2.10.4 IR summary

In general, there is a need for more IR studies in the CO_2 reduction field using the ATR-SEIRAS technique in order to increase the data pool and to resolve discrepancies in both observations and interpretations. More well-defined experiments combined with improved computational modelling of the interface and the inclusion of transport effects is expected to improve this.

2.11 Project focus points

Based on the previous sections, a number of points for continued research remain.

- What is the intrinsic activity of planar Cu for CO reduction? (in order to better assess the intrinsic activity of nanostructured catalysts).
- Is there oxygen at or near the surface at CO_2/CO reduction conditions?
- Can we observe restructuring of the surface during reaction conditions?
- Can we observe adsorbed intermediates of CO_2 reduction on Au and CO reduction on Cu and what can it tell us about the respective reactions?

These questions guided the work laid out in this thesis.
To answer the first question we performed CO reduction experiments on polycrystalline Cu in 0.1 M KOH, measuring the product activity and selectivity. We attempted to answer the next two questions, regarding the presence of oxygen and restructuring, by performing grazing incidence X-ray diffraction (GIXRD) synchrotron measurements on Cu during CO reduction conditions. The final question was investigated by the use of attenuated total reflection IR absorption spectroscopy (ATR-SEIRAS) on Au and Cu.
The results from the CO reduction activity and selectivity measurements, GIXRD, and ATR-SEIRAS experiments are described and discussed in separate chapters (4, 5, and 6, respectively). The corresponding experimental methods are given in Chapter 3. A general conclusion is given in Chapter 7.

Chapter 3

Experimental methods and procedures

This chapter describes the experimental methods and procedures used throughout this project as well as the relevant theory. They will for the most part be presented chronologically in the order of use in the project (the same order presented in this thesis). The first section deals with the electrochemical setup and instrumentation used for detection of products from CO reduction on polycrystalline Cu. The second section deals with grazing incidence X-ray diffraction using synchrotron radiation to detect the oxide on polycrystalline Cu during CO reduction. the final section deals with the methods relevant for Attenuated total reflection surface enhanced infrared spectroscopy on Cu and Au films for the investigation of CO and CO_2 reduction.

3.1 Electrochemical techniques

An electrochemical setup usually consists of a working electrode where the reaction of interest takes place, a counter electrode and a reference electrode. The current is drawn between the working and counter electrodes so that the current measured at the working electrode is mirrored at the counter electrode with opposite sign. The reference electrode has a fixed potential defined by a specific electrochemical equilibrium and this is used as a reference point for the working electrode. By varying the potential or the current and measuring the other, we can extract information about the electrochemical system.

3.1.1 Cyclic voltammetry (CV)

Cyclic voltammetry works by applying a triangular potential wave to the working electrode and observing the current response. At specific potentials various reactions will become possible on the electrode surface resulting in either reduction or oxidation current. This indicates what reaction reaction is going on at the surface and often allows one to recognise an electrode material due to its specific oxidation and reduction features under various conditions. Usually CVs are plotted as current vs potential so it is clear at what potential a specific reaction occurs.

3.1.2 Chronoamperometry (CA) and chronopotentiometry (CP)

Chronoamperometry is applying a fixed potential to the working electrode and observing the resulting current over time. Chronopotentiometry is the reverse where current is fixed and the resulting potential observed over time. CA is used for all the CO reduction experiments for selectivity and activity on Cu.

3.1.3 Impedance

Electrochemical impedance is the application of a sinusoidal potential wave of a specific frequency. The resulting current is measured. Different parts of the electrochemical system will have different time constants and thus respond to different frequencies. The total impedance of the system can be viewed as a combination of the individual parts through the use of an equivalent circuit as seen in Figure 3.1 [96]. The impedance spectrum is fitted with EC-lab and gives the values for the various components. Here the ohmic resistance R_Ω is around 35 to 45 Ω in 0.1 M KOH (in the glass H-cell). This is used to compensate for the ohmic drop (overpotential due to electrolyte resistance).

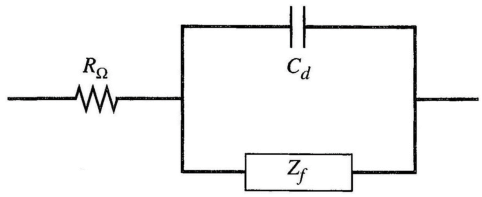

Figure 3.1: The equivalent circuit used to model the electrochemical cell. R_Ω is the electrolyte resistance, C_d the double layer capacitance, Z_f is the generalised impedance related to charge transfer resistance. Modified from[96, figure 10.1.4]

3.2 Electrochemistry coupled with product detection

This section deals with all the methods and procedures related to electrochemical CO reduction on planar polycrystalline Cu and the detection of the products.

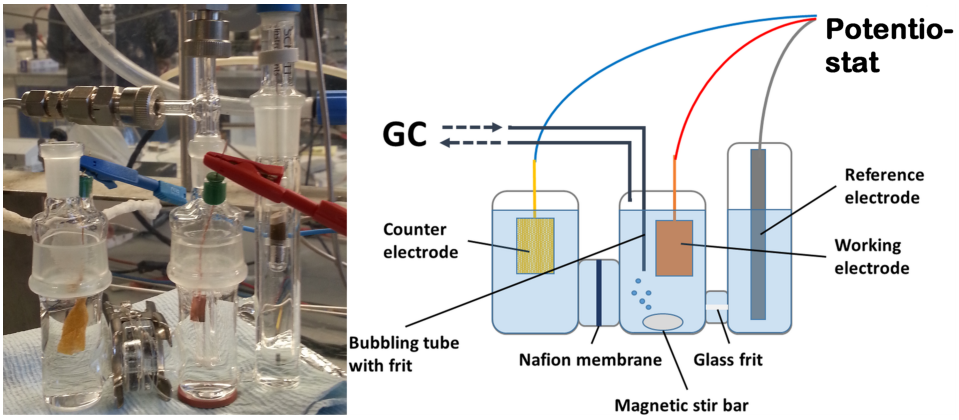

Figure 3.2: Photo and schematic representation of the H-cell used for electrochemical CO reduction. Cu foil working electrode, Au mesh counter and MSE reference electrode.

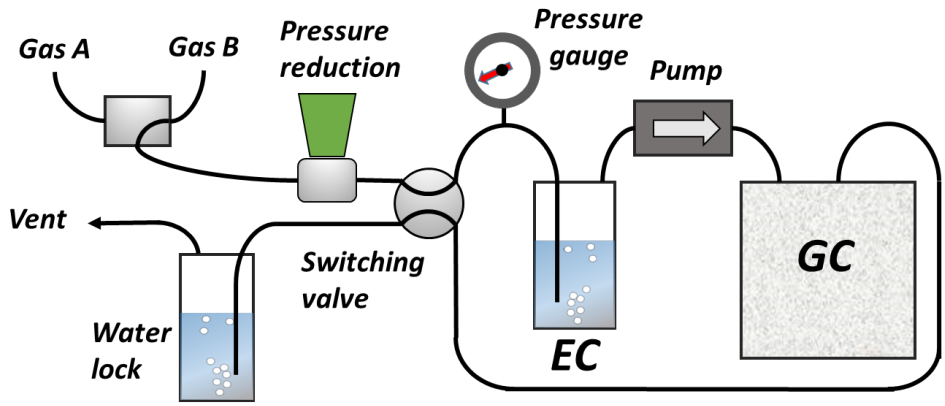

Figure 3.3: Schematic of the setup used for gas detection from electrochemical CO reduction. The switching valve allows for either constant purging of the system or closed circulation in a loop using the pump. Here shown in purge mode.

3.2.1 Electrochemical setup

The electrochemical setup for activity and selectivity studies of CO reduction on polycrystalline Cu consisted of a glass H-cell as seen in Figure 3.2. The

working electrode (WE) consisted of polycrystalline Cu foils (99.9999 %, Alfa Aesar Puratronic) on Cu wires (99.999 %, Goodfellow). The counter electrode (CE) was a Au mesh. The electrolyte was 0.1 M KOH (99.995, Merck suprapur). The gas purged electrolyte in the WE chamber and the non-purged electrolyte in the CE chamber (open to air) were separated by a cation exchange membrane (Nafion 117). The WE chamber was separated from a mecury-mercurous sulfate reference electrode by a ceramic frit. The electrochemistry was controlled by a Biologic VMP-2 potentiostat using the EC-lab software.
The WE chamber was purged by a glass bubbler. The gas handling system allowed for two modes of operation, one with constant purging of the WE electrolyte with new gas and the other with recycling of the same gas. The latter option allowed for up-concentration of the products in the gas stream and thus a higher sensitivity. Initially the WE electrolyte would be purged in constant flow mode and then switched to recycling mode for production and detection of products. All experiments were thus run in batch mode. The gas loop was part of the sample loop of an adjacent gas chromatograph, allowing for injection and detection of the gaseous products from the reaction at various times during an experiment (see Figure 3.3). Liquid products were analysed from the electrolyte post-reaction using static head-space gas chromatography and NMR. All NMR analysis was performed by Erlend Bertheussen and as such a descripton of the technique and procedure has not been included here but can be found in [97].

3.2.2 Gas chromatography

Gas chromatography works by the separation of different components of a gas stream in a column and detecting them as they exit. The characteristic time it takes the various compounds to exit and be detected is known as the retention time. Thus a chromatogram (spectrum of signal vs time) is obtained. The retention time for a compound depends on their interaction with the column, the temperature and the flow rate of the gas. The objective is to separate the compounds sufficiently to avoid overlap when they are detected as the detectors are not product specific. The GC used here was equipped with two common types of detectors, a flame ionisation detector and a thermal conductivity detector. In this setup the gas loop of the setup passed through two sample loops in the GC, each 250 μL in volume. These gas samples are injected in parallel in separate columns using Ar as the carrier gas. One sample goes through an HP-PLOT Q column and ends in an FID, the other sample goes through an H-PLOT Q and an HPLOT Molsieve column in series to a TCD. The temperature program for the oven was 35 °C for 5 min and a 10 °C min^{-1} ramp to 85 °C and held there for 5 min.

Flame ionisation detector (FID)
The FID works by ionising hydrocarbons in a hydrogen flame thereby producing CH^+ which are accelerated by an electric field onto a cathode producing a current. The current is proportional to the amount of carbons present in the ionised molecule. In order to detect CO and CO_2 using the FID, it must be preceded by a methaniser in which CO or CO_2 is converted to methane over a Ni catalyst with hydrogen gas.

Thermal conductivity detector (TCD)
The TCD measures the thermal conductivity of the gas stream relative to a reference stream (in this case Ar) and gives a signal. This detector is used for the non-hydrocarbons, mainly H_2 which is a biproduct during CO_2 and CO reduction from concurrent HER in aqueous media.

Static head-space gas chromatography (HS-GC)
Static HS-GC is used to measure the volatile liquid compounds by heating liquid to equilibrate compounds between the liquid and gas phase in the head-space above the liquid. The relative distribution of the volatile compounds in the liquid and gas phases is determined by their Henry's law constants. Following an experiment, part of the used electrolyte was filled in a vial and capped with a septum. The vial was heated in a separate oven and after equilibration part of the gas phase was injected into the regular GC. This only works for the compounds with a vapour pressure (i.e. alcohols and aldehydes but not ionic forms such as formate). An Agilent 7694E headspace sampler was utilised. 5 mL of electrolyte was sealed in 10 mL vials. Samples were equilibrated for 15 min at 70 °C before transfer to the GC via the split/splitless inlet in the splitless mode and injected in the H-PLOT Q column and detected with the FID. Usually 2 identical vials of 5 mL would be measured and the average signals used.

3.2.3 Converting signal to concentration

Calibration of gasses
Calibration of the GC was done with a calibration gas containing small known amounts of the hydrocarbons of interest (ca. 1.00 % CO, 0.20 % CH_4, 0.25 % C_2H_4, 0.15 % C_2H_6, 0.15 % C_3H_8 in Ar). A separate 5.0 % H_2 in Ar was also used. The hydrocarbons were calibrated with the FID and hydrogen with the TCD. To convert the signal into the amount of a specific compound produced, the following formula was applied:

$$A_i = K_i n_i \tag{3.1}$$

where A_i is the integrated signal under the peak obtained for compound i, K_i is the calibration factor, n_i is the total amount of compound i produced. After flushing the system with the calibration gas and closing the loop, the pressure in the loop is noted (usually at 1.10 bar) and the gas injected. When measuring the calibration gas the the total amount of a compound is determined by the ideal gas law letting us write:

$$A_{i,0} = K_i n_{i,0} = K_i \frac{f_i p_{tot,0} V_{tot}}{RT_0} \Leftrightarrow K_i = \frac{A_{i,0} RT_0}{f_i p_{tot,0} V_{tot}} \tag{3.2}$$

where f_i^0 is the fraction of compound i in the calibration gas, $p_{tot,0}$ the total pressure in the loop for the calibration measurement, V_{tot} the total volume of the loop, T_0 the temperature (in Kelvin) of the measurement and R the ideal gas constant. The only unknown is the total volume of the loop V_{tot}. In order to determine V_{tot}, a series of HER measurements in Ar bubbled electrolyte were performed. In each experiment the sample was initially reduced to the metallic form with constant purging of the system. Afterwards the loop was closed and reduction performed. Only HER was assumed to occur making the passed charge directly proportional to the produced amount of H_2. Several experiments with increasing amount of H_2 were performed. Applying Faraday's law to get $n_{H_2} = q_{H_2}/2F$, where q_{H_2} is the measured charge for the produced H_2 and F is Faraday's constant, we can write:

$$A_{H_2} = K_{H_2} n_{H_2} = K_{H_2} \frac{q_{H_2}}{2F} = \frac{A_{i,0} RT_0}{f_i p_{tot,0} V_{tot}} \frac{q_{H_2}}{2F} = \alpha q_{H_2} \tag{3.3}$$

which gives a straight line for the H_2 signal as a function of the passed charge. The slope α yields V_{tot} as the other factors are known. An example could be α = 475 which corresponds to a gas loop volume of 28 mL (including the headspace in the cell). An average of three measurements of the calibration gasses was used giving a deviation below 1 %. 4-6 points were used for the volume determination yielding a linear fit with an R^2 of for example 0.9993.

Calibration of liquids

Liquid calibration measurements were performed with HS-GC. Calibration samples with known amounts of the relevant compounds in 0.1 M KOH matrix were measured and the integrated intensity for the compounds vs their concentration was plotted. The slopes yielded the calibration factors as $A_i = K_i c_i$. It was found previously in the group that aldehydes polymerise in alkaline conditions, particularly at higher concentrations [98], wherefore the calibration samples had to be prepared and measured in close proximity. Additionally a few liquid compounds (acetate) were analysed by NMR in a similar fashion.

3.2.4 Product distribution

To convert the measured signals of an experiment into the selectivity, the product distribution is plotted as Faradaic efficiency which is the fraction of the charge that was used to produce a specific product. It can be written as

$$FE = \frac{q_i}{q_{tot}} = \frac{n_i}{z_i F q_{tot}} \tag{3.4}$$

where $n_i = A_i/K_i$ for gas products and $n_i = A_i V_{sol}/K_i$ for liquids with V_{sol} being the volume of electrolyte in the working chamber of the cell (always exactly 12 mL as measured with a pipette).

In order to get the activity of the reaction for a specific compound, the partial current density j_i (mA/cm^2) is calculated. For the batch experiments used here, the average of the current density is calculated from the partial charge q_i and the total time of the experiment. For the Cu foils used here the geometric surface area was 1 cm^2 and the roughness factor is assumed very close to 1.

3.2.5 Cleaning of glassware

All glassware was cleaned in either piranha (3:1 mixture of conc. H_2SO_4 and 30 % H_2O_2) or aqua regia (1:3 mixture of conc. HNO_3 and conc. HCl), leaving the glasware in solution over night. It was then rinsed 4-5 times with milli-Q water and boiled 2-3 times in milli-Q water with 3 rinses between each boiling. The glassware was subsequently stored in milli-Q water until use.

3.2.6 Electrode preparation

Cu electrodes were cut in 1.0 cm x 0.5 cm rectangles from an 0.1 mm Cu (99.999%) foil. The foils were pierced with a syringe needle and attached to a Cu wire. Prior to use the electrodes were electropolished in 30 wt% H_3PO_4 in a beaker approximately 2 cm from a counter wire at 2.1 V. Electropolishing was for 90 s on each side of the electrode. After extracting the electrode with potential control it was rinsed with Ar bubbled milli-Q water. It was then inserted in the H-cell.

3.2.7 Cation conducting membranes

The working and counter chambers were separated by a ionically conducting membrane to maintain a constant electrolyte volume in the working chamber and to avoid interference between the two half reactions, both of which would lead to quantification errors. Cation conducting Nafion 117 membranes were used. They were treated in accordance with a standard procedure [99]. The membranes

were cut to the appropriate final size (the flange of the cell). The pieces were boiled in 3 % H_2O_2 for 60 min in a piranha cleaned beaker to clean them. After a thorough rinsing with milli-Q water they were boiled in 0.1 M H_2SO_4 for 60 min to protonate them. Following another rinsing the membranes were boiled in 0.1 M $KClO_4$ for 60 min to exchange the protons for potassium ions, to avoid acidification of the electrolyte by the membrane. The membranes were then boiled 3 times for 20 min in fresh milli-Q water.

3.2.8 Reference electrode calibration

The Hg/Hg_2SO_4 reference electrode was calibrated in a special calibration cell, where one sealable chamber with two Pt wires is bubbled with H_2 gas. This chamber is connected via a ceramic frit to a chamber housing the reference. The Pt wires were first flame annealed and then cycled electrochemically from HER to initial OER in the electrolyte to be used (mainly 0.1 M KOH, Ar purged) in order to have clean Pt. After saturating the solution with H_2 gas and cycling around the HER equilibrium point, the OCV was measured as an indication of the RHE potential in the given electrolyte. As an example a value of -1.394 was obtained indicating that $E(Hg/Hg_2SO_4) = E(\text{RHE}) + 1.394$ V in 0.1 M KOH.

3.3 Ex-situ characterisation techniques

In order to characterise samples, either prior to or following an experiment, scanning electron microscopy (SEM) and X-ray photoelectron spectroscopy was applied.

3.3.1 Scanning electron microscopy (SEM)

SEM works by scanning a conductive sample in vacuum with a focused electron beam over a 2-dimensional area. This generates two types of electrons, secondary and backscattered electrons and X-rays.
Backscattered electrons (BSEs) are electrons from the beam that have reacted elastically with the sample and are reflected or backscattered. The reflection is greater from areas with higher atomic number yielding information about the atomic composition.
Secondary electrons (SEs) are electrons ejected from the outer electronic shells of the the sample atoms. The amount of secondary electrons ejected per geometric area will depend on the angle of the surface relative to the beam, with a steeper surface yielding more electrons and appearing brighter. This gives an indication of surface morphology.
When inner shell electrons are ejected and the atom relaxes to its stable state it emits X-rays specific to the element in question. Analysing these X-rays can give information about the elemental composition of the sample and is called Energy dispersive X-ray spectroscopy (EDX). [100]
In this project a QFEG or AFEG SEM was used both for investigation of polycrystalline Cu used in the activity and selectivity study and for investigation of the morphology of SEIRAS thin films.

3.3.2 X-ray photoelectron spectroscopy (XPS)

X-ray photoelectron spectroscopy works by using X-ray photons to excite core or valence electrons of the sample. The sample absorbs an X-ray and a photoelectron is emitted. The photoelectron has excess energy with respect to its bonding energy, E_b, which results in kinetic energy, E_k [101]. The following relation holds:

$$E_k = h\nu - E_b - \phi \tag{3.5}$$

where $h\nu$ is the energy of the incoming X-ray and ϕ is the work function of the energy analyser. This is illustrated in Figure 3.4. An XPS spectrum shows the intensity of photoelectrons as function of their kinetic energy. This can be converted to a function of the binding energy using the above equation. The technique is surface sensitive as the mean free path of the photoelectrons is low so

mainly electrons from the topmost atomic layer reach the analyser. The binding energy of the excited electron is element specific and also depends on its oxidation state and the spectrum will thus give information about the elemental composition and chemical state of the elements on the surface. Additionally to the XPS signals there are also signals from Auger electrons which are created when the excited ions created in the XPS process relax. This is also illustrated in Figure 3.4
Experiments were performed with a Thermo Scientific Thetaprobe spectrometer equipped with Kα source generating X-rays with 1386.4 eV. Cu electrodes used for selectivity and activity measurements were measured to test for metal impurities. To avoid possible metal deposits oxidatively stripping off, the electrodes were always extracted under potential control at the end of the measurement and either dried with lens paper without touching the area to be measured or were rinsed with Ar purged milli-Q water. SEIRAS films could not be extracted with potential control due to the setup design.

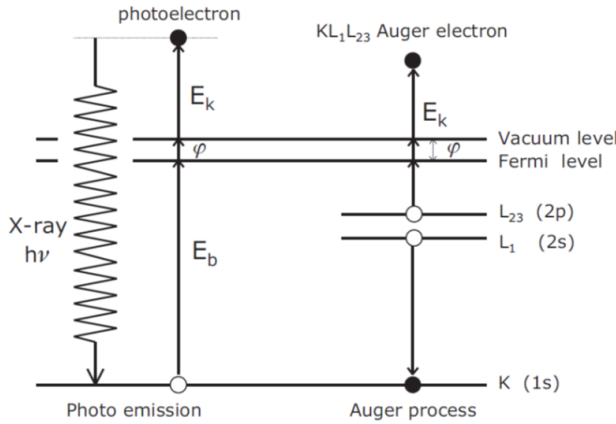

Figure 3.4: Schematic of the XPS and Auger process. [101, Figure 4.6]

3.4 In situ GIXRD setup

In order to understand the changes occurring at the catalyst surface during CO reduction on polycrystalline Cu grazing incidence X-ray diffraction was performed at a synchrotron radiation source.
A synchrotron source can deliver much higher intensity X-rays than a regular XRD source. This is needed in in situ/operando measurements in order to maintain a significant signal when passing through the electrolyte layer. The use of grazing incidence makes the technique surface sensitive as described below.

3.4.1 Grazing incidence X-ray diffraction (GIXRD)

In XRD, X-rays are scattered elastically in a sample. A periodic ordered structure will cause diffraction of the X-rays due to the interference of the reflected X-rays from the ordered planes. The requirement for constructive interference is given by Bragg's law [102]:

$$m\lambda = 2d\sin\theta \tag{3.6}$$

where λ is the wavelength of the X-rays, d the inter-lattice distance, θ the diffraction angle, and m an integer termed the refraction order. More generalised, the requirement for constructive interference is given by the Laue condition stating that the scattering vector $\mathbf{Q}$ vector must equal the reciprocal lattice vector $\mathbf{G_{hkl}}$

$$\mathbf{Q} = \mathbf{G_{hkl}} \tag{3.7}$$

where $\mathbf{Q} = \mathbf{k} - \mathbf{k}'$ and $\mathbf{k}$ and $\mathbf{k}'$ are the incident and refracted wavevectors respectively and h, k, l are the Miller indices indicating the plane. Observing the resulting diffraction pattern as a function of the diffraction angle θ yields the crystal structure and lattice spacing.

In order to attain surface sensitivity with XRD it is necessary to use a grazing incidence angle. This ensures that the beam is totally reflected at the surface and only a small evanescent wave penetrates and samples the topmost layers of the sample. This is illustrated in Figure 3.5 for a 17 keV beam and Cu. The beam penetration into the material is the attenuation length (distance before the intensity reduces to $1/e$). The critical angle is seen to be around 0.18 degrees. Below the critical angle only a few nm into the material are probed.

3.4.2 GIXRD Setup

In situ GIXRD was carried out at SSRL beamline 2-1, equipped with a Pilatus100K-S 2D X-ray detector. The photon energy was 17 keV. A BioLogic SP-200 potentiostat

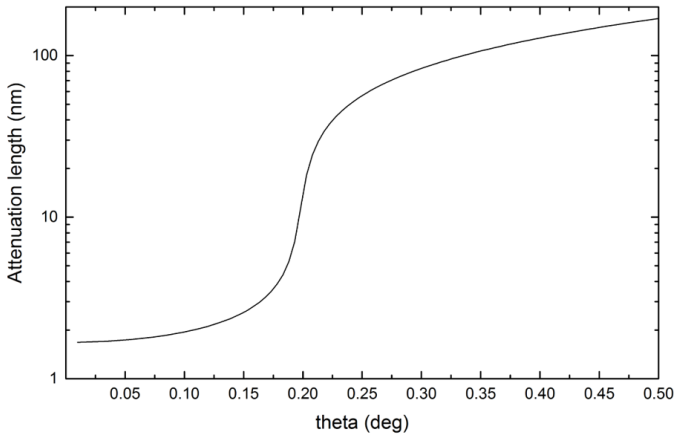

Figure 3.5: Attenuation length as a function of grazing angle for with 17 keV X-rays. Calculated using a tool from the Center for X-ray optics at the Lawrence Berkeley National Laboratory based on work by Henke et al [103].

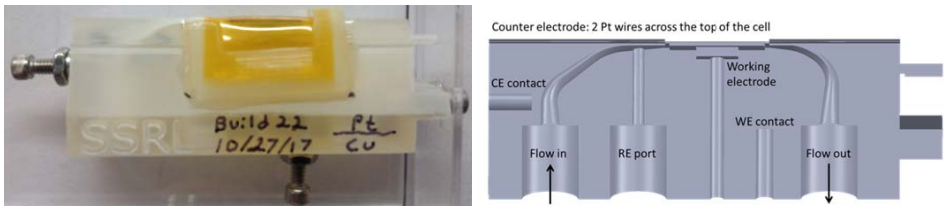

Figure 3.6: Left: Photo of in situ flow cell. Right: Schematic of cell.

was used to control the working electrode potential. The potentiostat was synchronized to the X-ray data acquisition using a TTL trigger.

Cell

The cell was a thin layer cell shown in Figure 3.6. The cell was developed as a collaboration between Berkeley and Stanford and has been described in [104]. The cell allowed for flow of a thin 200 μm tall channel of electrolyte with the thin film working electrode below and a polyimide (Kapton) window above. Two wires of either Au or Pt functioned as the counter electrodes and were parallel to the working electrode. connection to a Ag/AgCl reference electrode was realised through a Lugin capillary.

Flow system

Flow of electrolyte through the cell was maintained using a closed liquid loop pumped using an HPLC pump. Auxiliary compartments ensured sparging of the

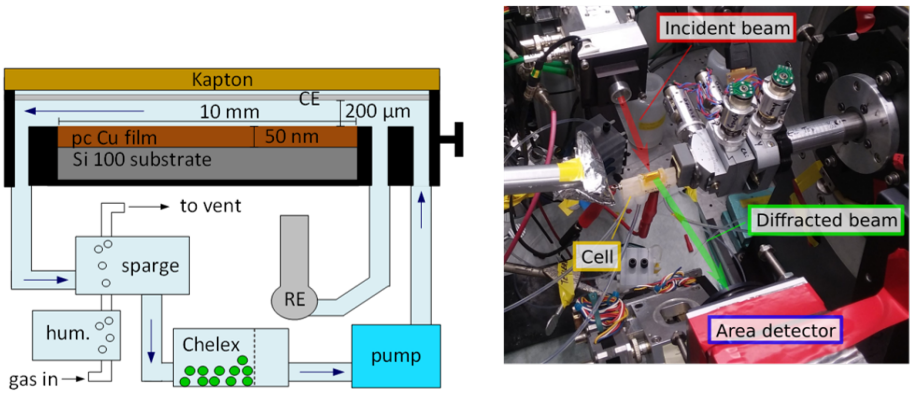

Figure 3.7: Left: Schematic of flow system for in situ GIXRD measurements. Right: Photo of setup. [105, Figure S1 a) and c)].

electrolyte stream with gas and cleaning of metal impurities using iminodiacetate resin (Chelex) held in place by a Ti mesh. This is illustrated in Figure 3.7. Electrolyte was 0.1 M KOH prepared from TraceSELECT KOH (>=99.995 %, Honeywell Fluka) and milli-Q water. The gasses were Ar (5.0 purity, Airgas) and CO (5.0 purity, Matheson). The gasses were flowed at 20-40 mL/min through first a humidifying cell and then the elctrolyte sparging cell. To avoid Ni carbonyls due to the stainless steel gas lines, the CO was allowed to flow at 40 mL/min for 30 min before use.

Samples

50 nm polycrystalline Cu thin films were e-beam deposited onto 3 mm by 10 mm degenerately doped Si(100) wafers with a 3 nm Cr sticking layer in between. The sticking layer also avoids epitaxial growth of Cu on Si(100) [106]. Samples were prepared 2 weeks before use and were exposed to air during this time. The samples were incorporated in the custom flow cell. See [104] for details on the cell.

Measurement procedure

Due to the 2D area of the detector, multiple angles of 2θ could be monitored simultaneously. At a fixed grazing incidence angle α, the detector could either be moved through all the values of 2θ from 0 to 60° or held at a fixed 2θ position. The first mode allowed for measurement of a regular XRD spectrum at fixed sample conditions, whereas the latter allowed for monitoring of dynamic changes in a specific Bragg peak over time with changing sample conditions (electrode potential, gas, electrolyte flow rate). The first mode is referred to as a 2θ-scan and

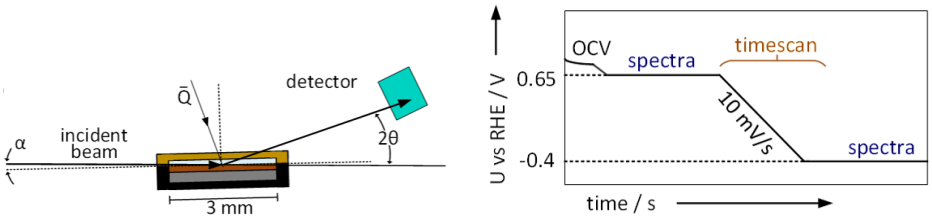

Figure 3.8: Left: Geometry of the GIXRD measurement showing the incident angle α, the 2θ angle and the resulting scattering vector **Q**. Right: Measurement procedure. [105, Figure S1 b) and d)]

the second as a time-scan.
Generally, all samples were aligned dry and dry GIXRD spectra were acquired. The pre-saturated electrolyte (either Ar or CO gas) was introduced. The samples were initially held at a fixed potential (usually 0.65 V vs RHE) just cathodic of the measured OCV of Cu (0.7-0.8 V vs RHE). Wet spectra were acquired at incident angles of α = 0.15° (attenuation length ca. 2.5 nm) and α = 0.20° (attenuation length ca. 20 nm). While maintaining a fixed grazing incidence angle of α = 0.15° and centering the detector at 2θ = 18.5°, the potential would then be scanned cathodically at 10 mV/s to potentials relevant for CO reduction (-0.4 or -0.5 V vs RHE). This would ensure that both the Cu(111) Bragg peak at 2θ = 20.1° and the Cu_2O(111) Bragg peak at 2θ = 16.9° would land on the detector during the reduction of the oxide. Finally GIXRD spectra were recorded at the cathodic potential. The geometry of the measurement and the measurement procedure are illustrated in Figure 3.8.

Data analysis
XRD spectra were calculated by matching detector pixels with 2θ values and adding up the counts and normalising by incident beam intensity. Peaks were integrated after subtraction of a linear background and peak centers and widths were determined using a gaussian fit. The data analysis was performed using a home-built python package (created by Soren Scott), "EC-Xray" available at github/ScottSoren.

3.5 Electrochemistry coupled with infrared spectroscopy

This section starts by presenting the theory behind infrared absorption by molecular bonds, Fourier transform IR (FTIR), attenuated total reflection and surface enhanced infrared absorption (ATR-SEIRAS) on thin metallic films. Then the spectroelectrochemical setup is described along with the synthesis procedure for surface enhanced films of Pt, Cu and Au.

3.5.1 Infrared absorption by molecular bonds

Infrared absorption spectroscopy deals with measuring absorptions in the infrared region of the electromagnetic spectrum. This region corresponds to the transitions from one vibrational state to another in molecules and thus gives a view of the various vibrations present in a molecule. These vibrations can be exemplified by the vibration of a diatomic molecule which can be modelled as two masses connected by a spring. The vibration will be dependent on the magnitude of the masses and the strength of the bond. Using the harmonic oscillator approximation for the potential curve of the separation between the two masses we get Schrödinger's equation as

$$\hat{H}\psi = \left[-\frac{\hbar^2}{2m_{eff}}\frac{d^2}{dx^2} + \frac{1}{2}k_f x^2\right]\psi = E\psi \tag{3.8}$$

where $\hat{H}$, ψ and E are the Hamiltonian, wavefunction, and energy for the motion, respectively, and x is the deviation from the equilibrium bond length. The resulting solution for the energy levels is

$$E(n) = \left(n + \frac{1}{2}\right)h\nu, \qquad \nu = \frac{1}{2\pi}\sqrt{\frac{k_f}{m_{eff}}}, \qquad m_{eff} = \frac{m_1 m_2}{m_1 + m_2}, \qquad n = 0, 1, 2, 3... \tag{3.9}$$

where n is the quantum mechanical energy level, k_f the force constant of the bond ($k_f = (\partial^2 V/\partial x^2)_0$) and m_{eff} the effective mass of the molecule containing the masses m_1 and m_2 [107]. The ground state ($n = 0$) is the most stable and the transition to the first exited state, the most common transition, gives the energy difference:

$$\Delta E(n = 0 \rightarrow 1) = h\nu = \frac{h}{2\pi}\sqrt{\frac{k_f}{m_{eff}}} \tag{3.10}$$

By dividing with the speed of light the equation can be stated in terms of wavenumbers (cm^{-1}) in stead of frequency (Hz).
The diatomic harmonic oscillator approximation can be extended to a polyatomic molecule as a set of uncoupled harmonic oscillators through the use of normal

mode analysis [108]. The potential energy well V will be a function of Nx3 coordinates (q_i), where N is the number of nuclei. Taylor expanding the potential around the equilibrium point (q_i^0) gives

$$V(q_1, ..., q_n) = \frac{1}{2} \sum_{i,j} \left(\frac{\partial^2 V}{\partial q_i \partial q_j} \right)_0 \eta_i \eta_j = \frac{1}{2} \sum_{i,j} f_{ij} \eta_i \eta_j, \qquad \eta_i = (q_i - q_i^0) \tag{3.11}$$

By diagonalising and thus changing to the normal mode coordinate system ($Q_s, s = 0, ..., n$) we get

$$V(Q_0, ..., Q_n) = \frac{1}{2} \sum_s \omega_s^2 Q_s^2 \tag{3.12}$$

This yields a Hamiltonian of the form

$$\hat{H} = -\sum_s \frac{\hbar^2}{2} \frac{\partial^2}{\partial Q_s^2} + \sum_s \frac{1}{2} \omega^2 Q_s^2 \tag{3.13}$$

This is similar to the form for the harmonic oscillator. Thus the total wavefunction can be written as a product of wavefunctions for each mode with each wavefunction being the wavefunction of a harmonic oscillator. Each characteristic vibration will therefore have its own frequency [108].
Additionally for a vibration to be IR active it must obey the selection rules which state that there must be a change in dipole moment $\mathbf{p}$ associated with the vibrational mode in question [109], that is

$$\boldsymbol{\rho} = \frac{\partial \mathbf{p}}{\partial q_i} \neq 0 \tag{3.14}$$

The Hamiltonian of the interaction of the electric field vector $\mathbf{E}$ with an electric dipole moment $\mathbf{p}$ is [109]:

$$\hat{H} = -\hat{\mathbf{E}} \cdot \hat{\mathbf{p}} \tag{3.15}$$

Using Fermi's golden rule, the absorption A is proportional to the probability of transition from an initial to a final state (i to j). The probability is proportional to the square of the Hamiltonian [109].

$$A \propto E^2 |\langle j|\boldsymbol{\rho}|i\rangle|^2 \cos^2\theta \tag{3.16}$$

This illustrates that the transition dipole moment $|\langle j|\boldsymbol{\rho}|i\rangle|$ must be nonzero. This results in for example homonuclear diatomic molecules such as N_2, O_2 and H_2 being IR inactive as they have no dipole moment.

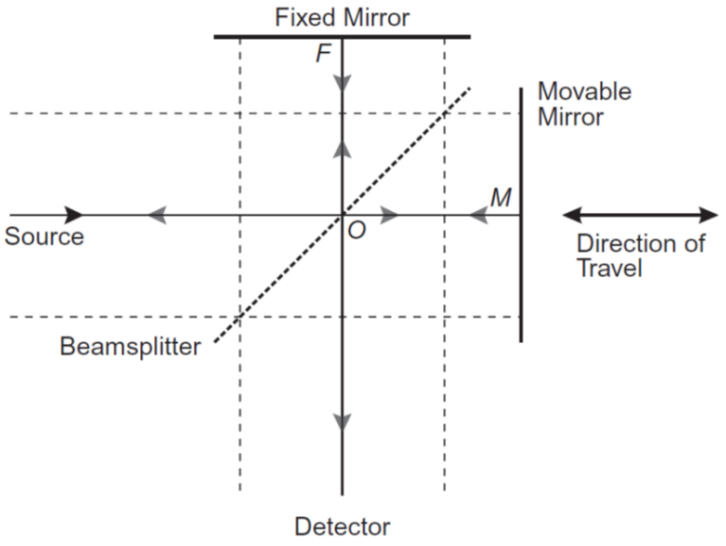

Figure 3.9: Schematic representation of the Michelson interferometer. The beamsplitter partially transmits and partially reflects light. A movable mirror changes the length of the beam path. [110, Figure 2.1].

3.5.2 Fourier transform infrared spectroscopy

Infrared measurements are commonly performed using a Fourier transform infrared (FTIR) spectrometer. A FTIR spectrometer measures the intensity of an IR beam passing through or reflecting off the sample of interest. Instead of using a monochromator to separate the signal from different wavelengths/wavenumbers, an interferometer allows a beam with the full IR spectrum to interfere with itself in a beam path of varying length - the so-called Michelson interferometer. An illustration of the Michelson interferometer is shown in Figure 3.9. This produces an interferogram which is light intensity as a function of mirror position. The interferogram is then Fourier transformed into a spectrum of light intensity vs wavelength or wavenumber. The interferogram can be written mathematically as a function of the optical path difference (OPD) δ [110]:

$$S(\delta) = \int_{-\infty}^{+\infty} B(\tilde{\nu}) \cos(2\pi\tilde{\nu}\delta) d\tilde{\nu} \tag{3.17}$$

where S is the interferogram at the detector and B is the intensity of the source as a function of the wavenumber $\tilde{\nu} = 1/\lambda$, modified by the characteristics of the

instrument. The transform is

$$B(\tilde{\nu}) = \int_{-\infty}^{+\infty} S(\delta)\cos(2\pi\tilde{\nu}\delta)d\delta = 2\int_{0}^{+\infty} S(\delta)\cos(2\pi\tilde{\nu}\delta)d\delta \tag{3.18}$$

where the last equality is due to the $S(\delta)$ being an even function. As the mirror cannot be moved infinitely there is a resulting limitation in spectral resolution. The resulting spectra from a measurement with a sample in the path I and a background without the sample I_0 are used to calculate the transmission spectrum $T(\tilde{\nu})$:

$$T(\tilde{\nu}) = \frac{I}{I_0} \tag{3.19}$$

This can be reformulated as absorbance $A(\tilde{\nu})$:

$$A(\tilde{\nu}) = -\log(T) \tag{3.20}$$

All data presented in this thesis are shown as absorbance unless otherwise stated. For example, $A = -\log(0.9/1) = 0.046$ a.u., where a.u. stands for absorbance unit, but is dimensionless. In general a sample spectrum I_S will be compared to a reference or background spectrum I_R at a reference condition and presented as:

$$A(\tilde{\nu}) = -\log(I_S/I_R) \tag{3.21}$$

This results in positive bands when more of an absorbing compound is present compared to the reference spectrum and negative bands if less is present compared to the reference.

3.5.3 Attenuated total reflection - surface enhanced infrared absorption spectroscopy (ATR-SEIRAS)

To understand ATR-SEIRAS we must first define ATR and SEIRAS.

ATR

The following formulas are taken from reference [109]. Normally, when an electromagnetic wave passes from a medium with one refractive index to another (n_1 to n_2), the wave is refracted, so that part of the beam is transmitted and part of it is reflected (see Figure 3.10). The relationship between the angles of the incident and transmitted beam is given by Snell's law:

$$n_1 \sin\phi_1 = n_2 \sin\phi_2 \tag{3.22}$$

However, when the incident angle surpasses the critical angle ($\phi_c = \arcsin(n_2/n_1)$) the beam is totally reflected (here assuming that medium 1 is optically denser

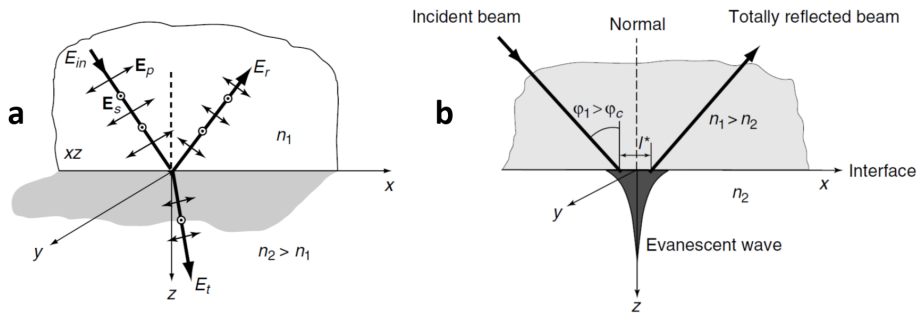

Figure 3.10: a) The electric field vectors in a two phase system showing the reflected and transmitted wave as well as the S and P components of the polarisation. b) Total internal reflection at incident angles above the critical angle, and the resulting evanescent wave. The small shift indicated by I^* is the so called Goos-Hänchen shift [109, Figures 1.9 and 1.10].

than medium 2, i.e. $n_1 > n_2$), but part of the electromagnetic wave penetrates into the optically rarer medium 2 as an evanescent wave (see Figure 3.10):

$$E \propto \exp[i(\omega t - k_x x + k_z z)] \tag{3.23}$$

$$k_x = \frac{\omega}{c} n_1 \sin^2 \phi_1 \tag{3.24}$$

$$k_z = i\frac{\omega}{c} n_2 \left[\left(\frac{n_1}{n_2} \right)^2 \sin^2 \phi_1 - 1 \right]^{1/2} \tag{3.25}$$

where the wave travels in the x-z plane, the x-axis being the interface. As k_z is imaginary (for $\phi_1 > \phi_c$) this results in an exponentially decaying wave in the z-direction. If additionally medium 2 absorbs, there is some loss of energy through the evanescent wave and it is said to be attenuated, hence attenuated total reflection.

Surface enhanced infrared absorption spectroscopy (SEIRAS)

SEIRAS is the result of enhancement of the absorption signal due to surface roughness of metallic films. The theoretical explanation as given by Masatoshi Osawa is the following [111]. a) Metal particles are polarised in an electromagnetic field by excitation of plasma resonances. b) These induced dipoles generate their own field around the particles that is stronger than the incident field. c) The molecules adsorbed on the particles are vibrationally excited by this enhanced field. d) These

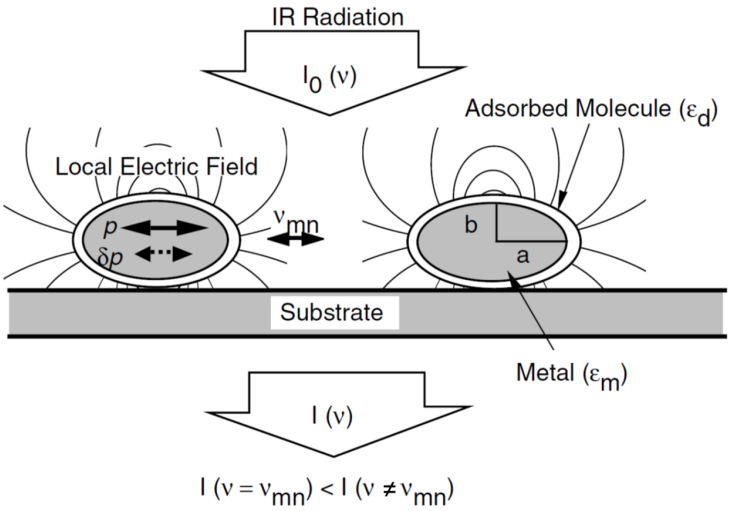

Figure 3.11: Schematic representation of the electromagnetic mechanism of SEIRA on metal island films. In simulations, the island film is modelled as a set of ellipsoids of rotation with a dielectric function ϵ_m, and the adsorbed molecules are modelled by a thin layer with a dielectric function ϵ_d covering the ellipsoids. The aspect ratio of the ellipsoids is defined as $\eta = a/b$. [111, Figure 2].

vibrations in turn create their own field in the particles leading to dampening or modulation of the polarisation of the particles at the frequencies of the molecular vibrations. e) SEIRA is thus the observation of molecular vibrations through the modulated absorption of the metal particles in the film. The principle is illustrated in Figure 3.11. The connection between the absorption of the adsorbed molecule and that of the metal film is illustrated in Figure 3.12 and there is seen to be a linear correlation [112].
The interaction of the electric field with a molecule has been modelled by Osawa as oblate ellipsoids of metal covered with a uniform film of adsorbates. He shows that the enhancement increases with the aspect ratio of the ellipsoids [113]. This is illustrated in Figure 3.13.
The absorption is proportional to the square of the change in dipole moment and the square of the local electric field as seen in Equation (3.16). The enhancement is therefore generally attributed to a combination of two mechanisms, the electromagnetic and the chemical mechanism. The first is due to an enhancement of the local electric field as is observed for metal particles and the second is an increase in the transition dipole moment of the molecule. CO chemisorbed on a flat metal has an increased absorption coefficient by 2-6 times compared to condensed overlayers of CO [111].

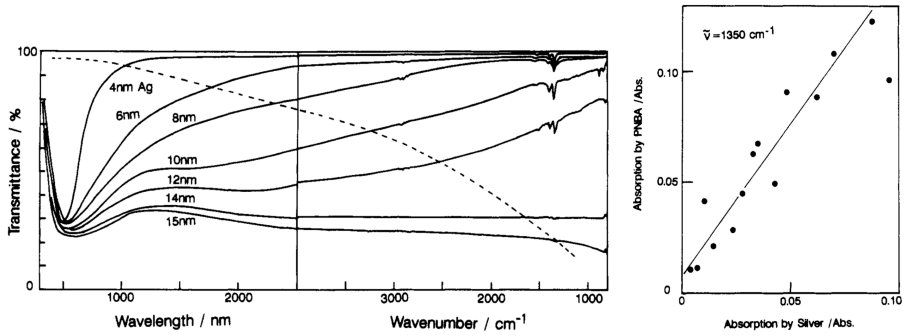

Figure 3.12: Left: Transmission spectra of silver island films evaporated on CaF_2. Mass thickness of the silver is shown in the figure. The metal films are coated with PNBA films of 1.7 nm average thickness. The dashed trace is the transmission spectrum of a hypothetical smooth and continuous silver film of 10 nm thickness on CaF_2 calculated with the Fresnel formula and the dielectric constants of bulk silver. Right: The absorption of the PNBA molecule vs the baseline absorption of the Ag metal film. [112, Figures 4 and 5].

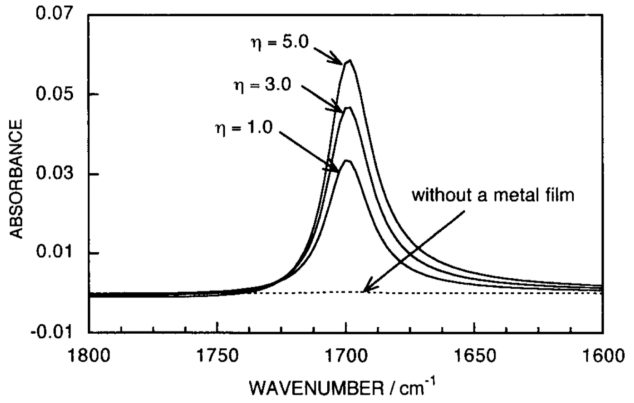

Figure 3.13: The absorption enhancement as a function of aspect ratio of oblate spheroids ($\eta = a/b$) modelled for an adsorbate on 8 nm Ag particles. [113, Figure 4].

The distance dependence of the electromagnetic field enhancement is given as[111]:

$$|E|^2 \propto \left(\frac{a}{a+d}\right)^6 \tag{3.26}$$

where d is the distance from the particle surface and a is the local curvature.
The absorption of the metal film is seen to extend into the IR region.
Additionally, SEIRAS is seen to obey the surface selection rule (SSR) which states that only vibrations with dipole moments perpendicular to the surface are IR active. This is due to the image dipole in the metal cancelling out the effective dipole for dipoles not perpendicular to the surface.

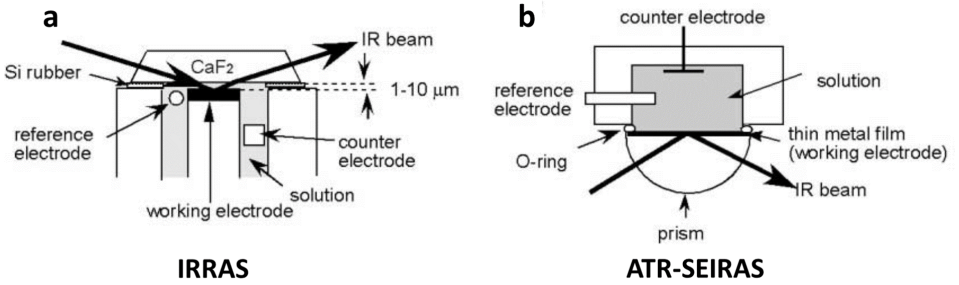

Figure 3.14: a) IRRAS configuration. b) ATR-SEIRAS configuration. Adapted from [111, Figure 6].

ATR-SEIRAS is the combination of ATR with a SEIRAS film on the internal reflection element. The configuration is shown compared to regular infrared reflection absorption spectroscopy (IRRAS) in Figure 3.14. ATR-SEIRAS is ideally suited for electrochemical investigation as the adsorbates on metal electrocatalyst films can be observed as a function of experimental conditions (electrolyte composition, partial pressures of gasses, temperature, applied potential, etc.). Some of these adsorbates will be the intermediates in the electrochemical reaction. The field of electrochemical ATR-SEIRAS was pioneered in great degree by Masatoshi Osawa and co-workers. He has successfully synthesised metal films consisting of Pt, Au, Ag, Cu and more [111]. Recent interest in the technique in relation to CO_2 reduction on Cu and Au has been shown by the groups of Yogesh Surendranath [78, 87], Bingjun Xu [89–91], and Matthias Waegele [79–81].

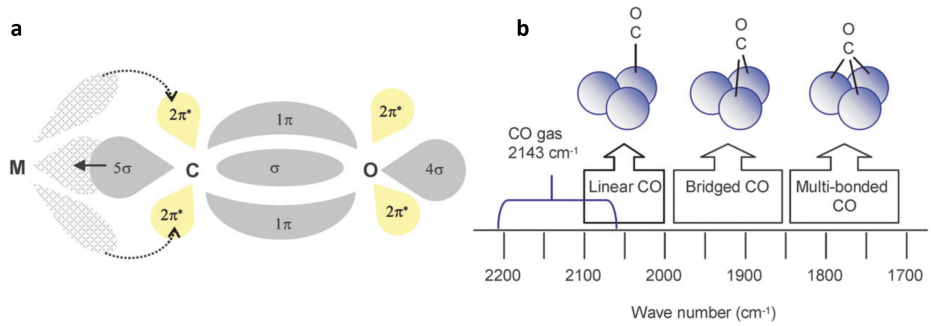

Figure 3.15: a) Model of the backbonding phenomenon for CO on d-band metals. b) Approximate wavenumber regions for CO based on coordination. From [114, Figure 8].

3.5.4 Trends in the band position of carbon monoxide upon adsorption on metals

CO is one of the main probe molecules in IR spectroscopy due to its simple structure [115]. In the following the general trend of the CO stretch frequency is given when going from gas phase to an adsorbate at the vacuum/metal interface and then to an andsorbate at the electrolyte/metal interface. The influence of coverage as well as binding to the surface and imposing an electric field are also described.

From gas phase to adsorbed at the vacuum/metal interface to the electrolyte/metal interface

The following is based on [115].

For CO the shift in wavenumber from gas phase to adsorption is generally downwards. Theoretically bonding to a surface would increase the wavenumber. The observed downwards shift is attributed to the image dipole of the CO in the metal by 20-30 cm^{-1} relative to the gas phase. A shift due to chemical interaction between the CO molecule and the substrate can be explained by the Blyholder model [116]. Here, the interaction is explained as electron donation to the metal through the sigma bond and backdonation from the metal through the d-orbitals to the anti bonding $\pi*$ bond of the CO, thus lowering the bond strength with increased backbonding. The backbonding model is illustrated in Figure 3.15. This also explains the change in CO stretch frequency for sites with different CO binding energy.

The position of the CO stretch band can usually be correlated to the coordination of the CO molecule, with higher coordination decreasing the wavenumber. The following typical grouping was given by Tolstoy et al. [109]:

- 1700-1900 cm^{-1}: threefold bridge
- 1900-2000 cm^{-1}: two-fold bridge bonded CO
- 2000-2100 cm^{-1}: CO atop

The transfer from vacuum to aqueous systems usually lowers these values by 20-30 cm^{-1} as the surface potential is lowered by the double layer environment [117].

Effects of coverage
As the coverage goes up the dipoles of the individual CO molecules can interact through dipole-dipole interactions which generally shifts the wavenumber positive. Backbonding can also be reduced as backbonding is distributed over more adsorbate molecules, and thus a shift to higher wavenumbers. Intermolecular repulsion through overlap of molecular orbitals can also lead to lower occupation of the antibonding pi orbital and hence increase in the wavenumber. [115]

Effect of electric field (potential)
The effect upon vibrational frequency from imposing an electric field on a vibrating dipole is termed the vibrational Stark effect [118]. Depending on the orientation of the dipole relative to the field, an increased field parallel to the dipole will compress it leading to higher wavenumbers and an increased field anti-parallel will have the opposite effect. When CO is adsorbed there is, however, also changes the chemical bonding to the surface due to charge transfer between the metal and the CO as the potential is shifted [119]. An increased negative potential will tend to transfer charge from the metal to the antibonding $\pi*$ orbitals, lowering the wavenumber [120]. These two processes for the change in CO frequency with applied potential lead to the same observed effect (positive shift with positive potential) and are two ways of describing the same underlying phenomenon [119]. The often linear dependence of vibrational frequency with applied potential is commonly referred to as the Stark shift or Stark tuning slope, irrespective of the exact physical process leading to the shift.

3.5.5 Spectroelectrochemical setup

Spectrometer
An INVENIO-R (Bruker) spectrometer equipped with a liquid N_2 cooled MCT (HgCdTe) detector was used for all experiments. The inside of the spectrometer was initially purged with N_2 gas. Later a purge apparatus that removed water vapour and CO_2 from compressed air was used.
The VeeMAXIII ATR accessory from (PIKE Instruments) was placed in the sample

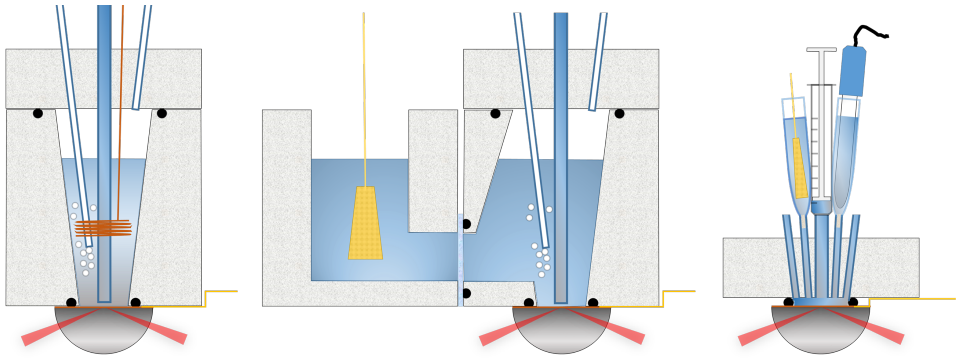

Figure 3.16: Graphical representation of the three types of cell design for spectroelectrochemistry. From left to right: one-compartment cell, two-compartment cell and lid-cell. See the text for a description of the cell types.

compartment to obtain the ATR geometry. An incident angle of 67.5° relative to the interface normal was utilised in all experiments.
Spectra were combined from 32 interferograms in the range 0 to 4950 cm^{-1} with 4 cm^{-1} resolution and a scanner velocity of 160 kHz using the double sided, forward and backward acquisition mode and a Happ-Genzel apodisation function. The aperture setting for the beam was 3 mm and the gain was x8. This resulted in one spectrum every ca. 3.7 seconds. When spectra were acquired continuously the spectrometer was set to measure a spectra with 4 s separation to ensure a constant temporal separation of the spectra.

Cells

All experiments were performed in the ATR Kretschmann configuration (thin metal film on internal reflection element) as illustrated in Figure 3.16. The basic layout was based off the design of the electrochemical cell option delivered by PIKE Instruments together with the VeeMAXIII ATR accessory. It consists of a PTFE cylinder on a flat plate (that is placed on the VeeMAXIII). The ATR crystal is held against the bottom of the cylinder with a plate and screws. The seal between the cylinder and the crystal is made by a Viton O-ring. The original design had the O-ring the same size as the crystal (20 mm diameter). This was changed to a smaller size to allow electrical contact to the dry metal film outside the O-ring. Electrical contact was made by thin pieces of Au foil threaded between the cylinder and the bottom plate. Progressive iteration of the design driven by various experimental needs resulted in 3 main types of cell with each their pros and cons. Graphical illustration of the cell types can be seen in Figure 3.16.

One-compartment cell
The first type was the basic liquid cup with an added lid containing port-holes for in- and outlets of liquid and gas as well as connection for the reference and counter electrodes. All porthole connections were made with M6 threaded IDEX fittings in combination with 1/8" and 1/16" PEEK or PFA polymer tubing. The reference electrode (MSE) was connected via tube ending just above the surface of the thin film electrode as a Luggin capillary. Flow in the tube was stopeed by a PTFE stop-cock that still allowed ionic contact. The counter was a metal wire curled into a spiral and fixed parallel to the working electrode. The metal for counter was usually chosen to be the same as the working electrode film. The total volume of the cup was approximately 5 mL. This design will be referred to as the one-compartment cell.

Two-compartment cell
The second type was a two-compartment cell consisting of two blocks of PTFE pressed around an ionically conducting membrane, connecting the two blocks. One block was identical in function to the one-compartment cell with the crystal pressed against the bottom and made use of an identical lid. The other block had no bottom hole and no lid was used. The counter electrode in the form of a Au mesh was placed here. This allowed for separation of the two half reactions so they would not interfere with each other. This design is the closest to the glass H-cell used for the selectivity and activity studies. The volume of the working chamber is approximately 15 mL. It is bigger than the one-compartment cell to allow for the connection to the block containing the counter. This design will be referred to as the two-compartment cell.

Lid-cell
The third type was an attempt at a small volume flow cell. It was realised by fixing the lid directly onto the bottom plate and only having the O-ring as separator between the thin film electrode and the lid. The volume in the cell was thus defined by the height of the compressed O-ring (and some volume in the lid connections). This design necessitated external bubbling of the electrolyte in a glass flask equipped with a glass frit bubbler. The reference and counter electrodes were placed in glass tubes ending in syringe size tips sealed with frits. These were placed in IDEX-to-syringe type fittings. Assembly of this design was cumbersome as there was no grove in the lid to hold the O-ring in place. Additionally an inconveniently placed port hole required compressing the O-ring slightly to an elliptical shape using the Au contacts. This design will be referred to as the lid-cell.

3.5.6 Spectroelectrochemical setup at MIT

The IR setup at MIT was very similar to that at DTU as described in the previous sections. The spectrometer was a Bruker Vertex 70 with an MCT detector and the VeeMAXII ATR accessory. The cell was similar in design to the one-compartment cell except for a substantially larger volume (ca. 100-200 mL). The counter was a Pt wire and the reference was a Ag/AgCl immersed in the electrolyte.

3.5.7 Electroless synthesis of SEIRAS active films

During the project, Pt, Cu and Au SEIRAS films were synthesised. Pt film synthesis using electroless deposition was initially taught to me by Yu Katayama and this laid the basis for the procedures of Cu and Au. Pt was mainly used as an initial test of SEIRAS in our lab and to get familiar with the spectroelectrochemical procedure on a reference material with previous success. No continued work was performed on Pt after this initial stage as the focus became synthesis of first Cu and then also Au films.
In the following the experimental synthesis procedure will be given for the three metals beginning with the cleaning and etching procedure general to them all.

Cleaning of optical crystals
In general Si hemispheres (20 mm diameter, non-doped FZ-Si, Pier Optics, Japan) were polished using alumina paste of decreasing particle size (0.3 and 0.05 μm, Buehler) to remove the previously deposited film and dirt. Usually, both particle sizes were used sequentially for 1-2 min separated by a thorough rinse with milli-Q water and performed on different polishing pads. However, only using the big particle size did not seem to be detrimental to the films in way of structure, stability or SEIRAS performance. The limited quality of manual polishing did result in visible gradual roughening of the surfaces but not in a notable degradation of the SEIRAS performance.
Following the last polishing step the polishing paste would be rinsed off with milli-Q water. The crystals would then be sonicated in a small glass beaker held in place by the lid from a septum-vial flask sequentially for 10-15 min each in milli-Q water, ethanol and milli-Q water. Between each change of solution the crystal and beaker was rinsed 3 times with milli-Q to wash away the old solution. These sonication steps ensured sequentially removal of alumina particles, grease and finally ethanol (and some compounds dissolved therein from the plastic container).
In some cases film deposition would occur on some part of the spherical face of the crystal which could unwantedly result in reflection of the incident or reflected beam. This could usually be mitigated by rotating the deposited region out of the

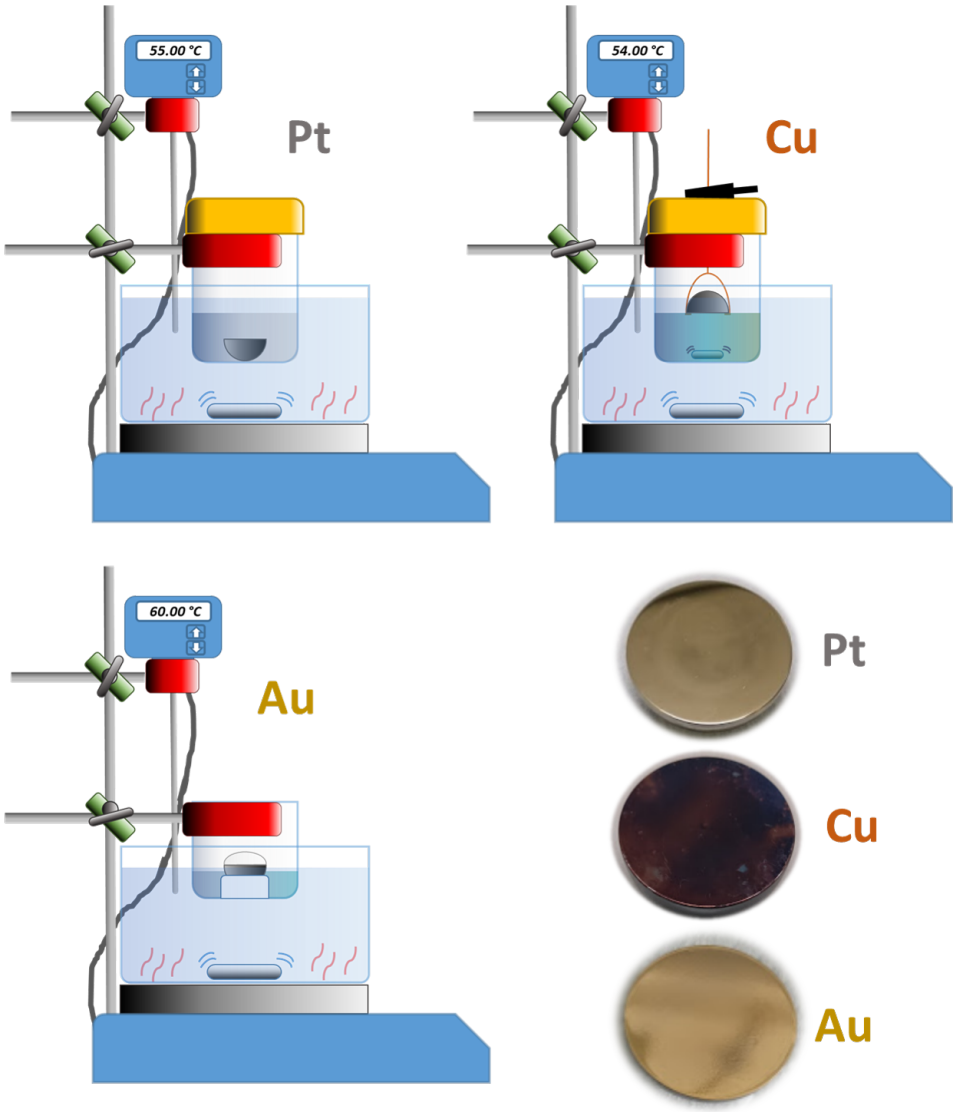

Figure 3.17: Graphical illustration of the plating baths used for Pt, Cu and Au, and examples of the resulting films. See text for details.

beam path but the crystals would eventually need cleaning in an appropriate acid (aqua regia for Pt and Au and nitric acid for Cu).

Oxide removal and hydrogen termination with NH_4F
In order remove the native oxide on the Si surface all crystals were etched with 40 wt% NH_4F for 0.5-2 min depending on the following synthesis. After drying the crystals completely (using a pipette ball fitted with a small micro-pipette tip), following the last sonication step, the crystals were placed on septum-vial flask lids for stability and oriented as flat as possible. For a 20 mm diameter crystal, 0.85 mL NH_4F was placed on the flat surface using a micro-pipette and left to etch. After 0.5-2 min the NH_4F was removed with the micro-pipette without touching the crystal face with the pipette tip. Milli-Q water was carefully added to the surface with a rinse flask and removed with the pipette 3-4 times. The crystal was then dried again. The following steps are specific to the metal.

Pt film synthesis on Si
The procedure consists of an initial formation of a Pd seed layer by dissolution of Si using F^- ions. The Pt is then plated on top of these seeds with hydrazine as a reductant.

Following the NH_4F etch, the crystal was first subjected to a Pd seed step and then Pt plating. The seed solution is 1 mM $PdCl_2$ in 0.5 % HF. 0.85 mL of the solution is placed on the crystal and left there for 5 min (room temperature). It is removed with the pipette while taking great care not to touch the surface and it is immediately submerged in a water bath to quench the seeding. The Pt plating solution is prepared from a commercial solution (LECTROLESS Pt 100, EEJA, Japan) by mixing 30:30:3:0.6 mL of LECTROLESS Pt100 base solution : Milli-Q water : 28 % NH_3 solution : LECTROLESS Pt 100 reducing solution. The plating solution was placed in a polypropylene beaker in a heating bath with temperature control at 55 °C (resulting in approximately 48 °C in the solution). The Si crystal was placed in the solution beaker for 8-15 min until sufficient plating had occurred and then submerged in Milli-Q water to quench the plating. The resulting conductivity across the diameter of the film should be around 10 Ω. A graphical representation of the plating setup for the three metal is given in Figure 3.17

This procedure has also been described elsewhere [121–123]. The use of a commercial solution is unfortunate, particularly as the exact contents are unknown. It was in fact not possible to buy the solutions directly from the company as they were discontinuing the production. One reference using the procedure states the following final composition of the plating bath [121]: "0.01 M hexaammineplat-

inum(IV)hydroxide + 0.06 M hydrazine monohydrate + 0.7–1.1 M ammonia + additives (stabilizer)". An alternative non-commercial solution was suggested by the same author in a later publication (see reference [122]). An alternative procedure is given in reference [124].

Cu film synthesis on Si

The procedure for electroless deposition of Cu films was initially based on the description by Anna Wuttig [78] which is also extensively applied with slight modifications by Charuni Gunathunge [79–81]. This procedure seemed to build on the prior work in Masatoshi Osawa's group [75, 76]. The general idea is similar to the Pt film synthesis in that a seed layer is first formed by the reduction of Cu onto the Si surface by simultaneous oxidation of Si [76].

$$Cu^{2+}(aq) + 2e^- \longrightarrow Cu(s) \tag{3.27}$$

$$Si(s) + 6\,F^-(aq) \longrightarrow SiF_6^{2-}(aq) + 4e^- \tag{3.28}$$

Plating is then performed on these seeds [76]

$$Cu^{2+}(aq) + 2e^- \longrightarrow Cu(s) \tag{3.29}$$

$$2HCHO + 4OH^- \longrightarrow 2HCOO^- + H_2 + 2H_2O + 2e^- \tag{3.30}$$

where HCHO is the reductant and EDTA and 2,2-bipyridine act both as the stabilisers of Cu ions in solution and influence growth on the film surface.

Following etching with NH_4F, the Si crystal was first subjected to a Cu seed step and then a Cu plating step. The seed solution was 750 μM $CuSO_4$ in 0.5 % HF. 0.85 mL of the seed solution was placed on the crystal and left there for 5 min. The Cu plating bath was prepared from 3 stock solutions: A: = 0.1 M $CuSO_4$, B: 1.25 M HCHO (prepared from 37 % HCHO with 10-15 % methanol as stabiliser), C: 0.10 M Na_2EDTA + 1.5 mM 2,2-bipyridine (pH adjusted to 12 with conc. NaOH). First 5 mL of solution A was mixed with 5 mL of solution B in a 100 mL polypropylene beaker. Then 5 mL of solution C was added dropwise to the beaker using a pipette while the beaker was stirred using a PTFE coated stir bar. The solution was then diluted to 25 mL with 10 mL milli-Q water, resulting in a 1:1:1:2 mixture of A : B : C : water, so 1/5 of the original concentration of the stock solutions. Finally the solution pH was adjusted to ca. 12 with conc. NaOH, using a pH-meter.

The closed beaker was then placed in the heating bath (55 °C) and allowed to equilibrate for ca. 5-10 min with magnetic stirring. The crystal was then placed in the sealed beaker held by a Cu wire allowing the seeded crystal face to make contact to the plating solution in form of a meniscus. The wire was threaded

through a small hole in the lid and held by a crocodile clip allowing good control of the crystal height. The crystal would be left for approximately 10 min total and would be rotated ca. 120° two times during the deposition to allow for a more uniform film. In some cases the crystal would be taken out for visual inspection during the deposition to gauge the plating rate. Finally, to quench the plating, the crystal was submerged in milli-Q water and dried. The resistance across the diameter was usually 1-2 Ω.

The procedure was changed several times to improve the film. The seeding time was increased from 1.5 min to 5 min and the plating time from 3.5 min to 10 min. This also resulted in a lower film resistance (15-20 Ω to 1-2 Ω). If a film had too low conductivity it could be re-immersed in the plating bath and this would sometimes give a good result but did sometimes result in film delamination. Using a sealed beaker seemed to improve the bath stability, presumable due to hindered evaporation of the reductant (HCHO). In many cases the plating bath would start to decompose (bulk reduction of Cu in solution). This would generally mean longer time required for the plating step. The best results were obtained when there was no visible decomposition of the bath (stayed bright blue). It is believed that high bath stability can be obtained by the use of very clean containers and substrates. Working Cu SEIRAS films were however obtained without high bath stability. In light of this variable bath stability, the plating time should be calibrated to the plating rate obtainable with the individually prepared solutions.

Au film synthesis on Si

The synthesis of Au films was based on the procedure described by Hiroto Miyake [86] which is a modification of work by Kato [125, and references therein] by exchanging ascorbic acid for HF to allow for the initial deposition of Au on to Si. The seeding and plating is done in one step with the same solution. The main plating is from Au(I) complexed with a mixture of sulfite, sulfate thiosulfate.

Following the NH_4F etch, the dry crystal is placed on a septum-vial lid in a low rimmed open beaker positioned in a heated water bath set to 60 °C. The plating solution was prepared from three stock solutions: A: 0.03 M $NaAuClO_4$, B: 0.3 M Na_2SO_3 + 0.1 M $Na_2S_2O_3$ + 0.1 M NH_4Cl, and 2 % HF. Initially 1 mL of solution A was pipetted into a polypropylene tube and diluted with 2 mL of milli-Q water. To this was added 1 mL of solution B. It was found that a fast forceful addition of solution B could yield a completely clear colorless solution in contrast to slower addition that yielded some bulk precipitation and yellowish/reddish hue. Finally 2 mL of 2 % HF was added to the solution yielding the final plating solution. 0.7 mL of the plating solution was pipetted onto the heated crystal face

and left for 5 min resulting in a clear change from grey Si to vibrant Au. The solution was removed from the surface and exchanged for cold milli-Q water several times to quench the plating. The crystal was removed from the heating bath, rinsed more thoroughly, and dried. The resistance along the diameter was measured to 9-12 Ω.

The quality of the plating solution seemed to depend somewhat on the age of the stock solutions, degrading over time, possibly due to contaminants. The completely clear plating solution would stay clear also during the plating on the crystal and for several weeks in the tube at room temperature. For less stable versions of the plating solution it would start to decompose during the plating and form a brown suspension.

Electrochemical cleaning and SEIRAS activation of films
The first step in each IR spectroelectrochemical experiment would be to cycle the film electrochemically. This would serve a triple purpose: 1) to strip off contaminants, 2) to structure the film akin to the oxidation reduction cycling (ORC) known from preparation of surface enhanced Raman (SERS) active surfaces, and 3) to "adjust" the film to being polarised. In the case of Pt, the cycling was performed in the potential window from initial hydrogen evolution to initial oxygen evolution at 50 mV/s. For Cu it was in the window between initial hydrogen evolution and the initial part of the first oxidation wave at 50 mV/s. Further oxidation would destroy the film. For Au the window was between initial hydrogen evolution and initial oxygen evolution. Au cycling was always performed in 0.1 M $HClO_4$ independently of the electrolyte used after.

Chapter 4

Activity and selectivity for electrochemical reduction of CO on polycrystalline Cu

This chapter describes the work performed on CO reduction on polycrystalline Cu. The main results have been published in [97] which is appended at the end of this thesis. The experimental part can be found in Section 3.2. The experimental work, data analysis and manuscript preparation was carried out in collaboration with Erlend Bertheussen who was a PhD at SurfCat and we share the first author position. Additionally, experimental work and data analysis was performed by Albert K. Engstfeld (a PostDoc in our group) and some preliminary experiments were performed by a visiting PhD student Younes Abghoui. Ifan E.L. Stephens and Ib Chorkendorff supervised the project. All authors revised the manuscript.

As previously mentioned, Cu has been shown to be the only single metal compound to effectively electrochemically reduce CO_2 past the first reduction step of forming CO to form further reduced hydrocarbons and oxygenates. Particularly, nanostructured Cu catalysts have shown a high activity and selectivity towards both CO_2 and CO reduction. In order to evaluate the effect of nanostructuring, a benchmark for the planar catalysts was required. This led to experiments with flat polycrystalline Cu foils for CO reduction.

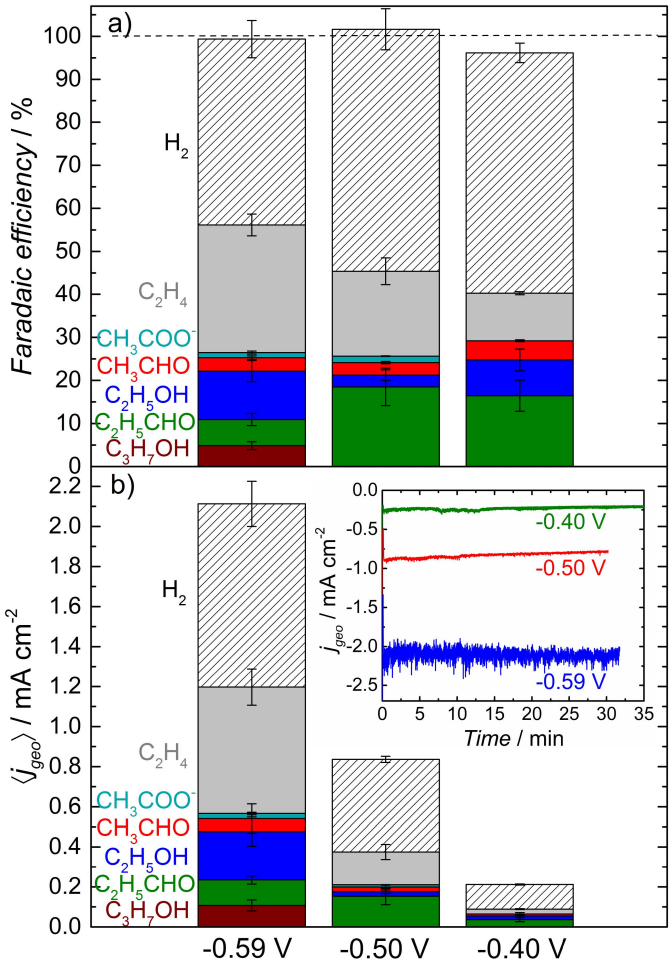

Figure 4.1: CO reduction on polycrystalline Cu in 0.1 M KOH. a) Faradaic efficiencies. b) Mean partial current density for individual products. Insert: Representative chronoamperometry traces for each potential. 3 individual measurements were performed for each potential. Error bars represent $\pm\sigma$ for each product.

4.1 CO reduction on polycrystalline Cu

Electrochemical CO reduction was performed on polycrystalline Cu foils in 0.1 M KOH with chronoamperometric batch experiments at -0.40, -0.50 and -0.69 V vs RHE for approximately 30 min. The products were analysed with a combination of GC for gasses and HS-GC and NMR for liquids. The resulting Faradaic efficiencies and partial current densities can be seen in Figure 4.1. It can be seen that, within the error of the measurement, all the current is accounted for. CO

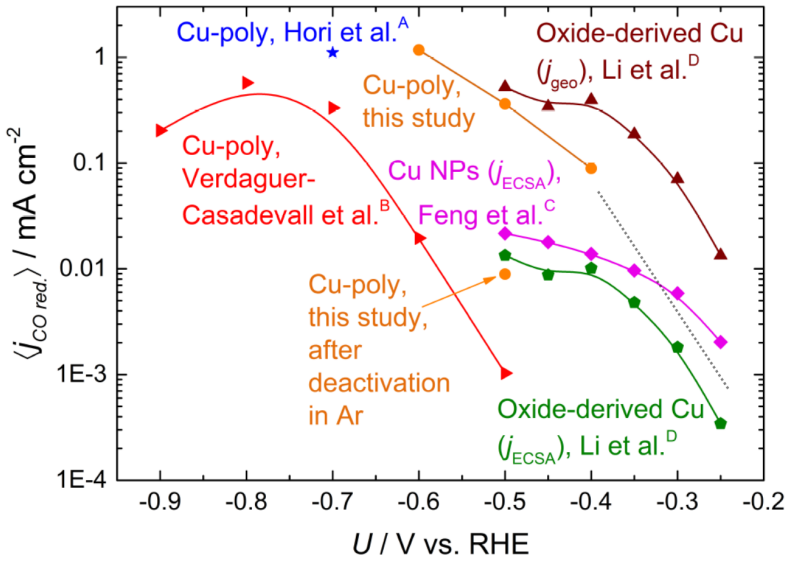

Figure 4.2: Mean CO reduction current densities for polycrystalline, oxide-derived and nanoparticle Cu in 0.1 M KOH. The results from this study are shown together with data adapted from (A) Hori et al. [34], (B) Verdaguer-Casadevall et al. [52], (C) Feng et al. [51], and(D) Li et al. [39]. The stippled gray line projects the intrinsic trend of the nanostructured catalysts in what is believed to be the region not influenced by mass transport limitations.

reduction activity was observed for all the measured potentials but increased as more cathodic potentials were applied. the greatest CO reduction activity and selectivity was achieved at the most negative potential (-0.59 V) yielding current density of 1.2 mA/cm^2 and 56 % Faradaic efficiency. The remainder of the current is accounted for by the concurrent evolution of H_2. The major CO reduction products were ethene (30 % at -0.59 V) and propanal (18 % at -0.5 V). Ethanol, ethanal, 1-propanol and acetate were also formed. The trend with increasingly negative potential is an increase in alcohol selectivity. It has previously been shown that aldehydes function as the precursors to the corresponding alcohol, such that ethanal forms ethanol [36, 126, 127] and propanal forms 1-propanol [36]. The formation of 1-propanol is only observed at the most negative potential of -0.59 V along with a decrease in the propanal selectivity.

4.2 Comparison to literature data for polycrystalline and nanostructured Cu

The CO reduction activity of polycrystalline Cu measured here was compared to other sources for both polycrystalline and nanostructured Cu [34, 39, 51, 52]. This is shown in Figure 4.2. The current densities normalised by electrochemically active surface area (ECSA) are shown. The following roughness factors (RF) were used: polycrystalline Cu (RF = 1), oxide-derived Cu (RF=39), Cu nanoparticles (RF = 66). These were estimated using double-layer capacitance measurements in the double layer region compared to planar Cu foil that was assumed to have roughness factor of 1.

It was observed that the nanostructured catalysts had a decrease in slope around -0.3 to -0.35 V vs RHE, which most likely results from mass transport limitations. When extending the trend of the nanostructured catalysts from the points not affected by mass transport limitations it was seen that these would roughly line up with the points from the present study. This indicated that there was no apparent difference in the intrinsic CO reduction activity between planar and nanostructured Cu. The reason for higher current densities when normalised to geometric surface area seemed mainly due to the very large roughness factors of 39-66. Thus high intrinsic CO reduction activity could be obtained on Cu without nanostructuring.

Nanostructured Cu reaches mass transport limitations at lower overpotentials than polycrystalline Cu due to the higher ECSA. The higher ECSA also allows for product detection at lower overpotentials as the geometric current densities are higher. This means that the potential ranges where product detection can be performed for polycrystalline and nanostructured Cu without mass transport limitations do not overlap. Therefore the activity could not be directly compared at the same potentials but had to extrapolated as done above.

When the product distributions were compared they showed very different behaviours for the polycrystalline and nanostructured samples. For our polycrystalline Cu, a high ethene selectivity was observed at all the measured potentials. On nanostructured Cu, however, the ethene selectivities are very low and mainly oxygenates are formed. This could be supported by the fact that for CO_2 reduction it has been shown that oxygenates are mainly formed at low overpotentials whereas hydrocarbons (such as ethene) require higher overpotentials [18]. Thus, it would seem that hydrocarbons are formed to a lesser extent on nanostructured catalysts due to the required overpotential lying in the mass transport limited range.

On nanostructured oxide-derived Cu a trend towards higher alcohol selectivity compared to aldehydes is also observed [39, 127]. This could be attributed to

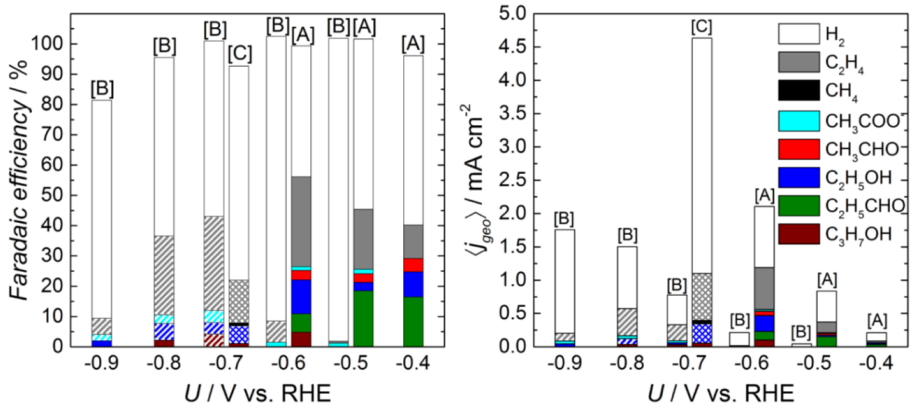

Figure 4.3: Faradaic efficiencies (a), and partial current densities (b) for polycrystalline Cu in 0.1 M KOH. The results from [A] this study are shown together with data adapted from [B] Verdaguer-Casadevall et al. [52] and [C] Hori et al. [34].

3 effects: i) the difference in available potential regions without mass transport limitations, ii) the high surface area and porous structure of oxide-derived Cu results in higher probability for readsorption of aldehydes onto the catalyst and further reduction to alcohols, iii) the oxide-derived Cu has more undercoordinated and thus strong binding sites that are more effective at reducing aldehydes to alcohol [126].

The polycrystalline Cu data from our work differed substantially from the other polycrystalline Cu data as is seen in Figure 4.2. Our data showed significant activity between -0.4 and -0.59 V. The data from Verdaguer-casadevall et al. was previous work from our group and Kanan's group and showed no or low activity from -0.5 to -0.9 V. Hori et al. measured one point at relevant conditions and got similar activities to our work but at a higher overpotential of -0.7 V. The three datasets are compared in Figure 4.3 in terms of Faradaic efficiency and partial current densities. The study by Verdaguer-Casadevall et al. shows mainly hydrogen production at potentials comparable to our study (-0.5 and -0.6 V) and higher overpotentials are required for increased selectivity to hydrocarbons and oxygenates. The total activity is also seen to be much lower than in our study in terms of required overpotential. The study by Hori et al. at -0.7 V shows lower CO reduction selectivity than our point at -0.59 V, that is more current goes to H_2. The total CO reduction activity is similar however. This could indicate that the point measured by Hori is in the mass transport limited range. The large discrepancies in the different polycrystalline Cu studies led us to compare the

Experimental conditions	This study	Hori et al. [34]	Verdaguer-Casadevall et al. [52]
Cell material	Glass	Not stated. Glass used in previous publication [21]	Glass
Electrode	Cu foil (99.9999%, Alfa Aesa Supratronic	Cu foil (99.999%, electro-deposited, donated from Sumitomo Metal Mining Co. Ltd.)	Cu foil (99.9999%, Alfa Aesa Supratronic
Electrode preparation	Electropolishing at 2.1 V vs Cu for 2x90 s in 30% H_3PO_4	Electropolishing for 2 min in 85 % H_3PO_4, electrode material and potential not stated.	Electropolishing in 85 % H_3PO_4 at 5 V against a Ti wire for 5 min.
Electrolyte	0.1 m KOH (Merck Suprapur, >99.995%	0.1 M KOH (reagent grade, pre-electrolysed with Pt black).	0.1 M KOH (semiconductor grade, >99.99%).
CO gas purity	99.95 %	>99.95 %	99.5 %
CO flow rate	~ 30 sccm	~ 70 sccm	5 sccm
CO reduction measurement	Chronoamperometry, ~ 30 min at specified potential	Chronoamperometry, ~ 30 min at 5 mA cm^{-2}	Chronoamperometry, 2-3 hours at specified potential

Table 4.1: Overview of the experimental conditions for this study and those of Hori et al. [34] and Verdaguer-Casadevall et al. [52].

experimental conditions applied. This is shown in Table 4.1
The first noticeable difference is the much longer time spent for CO reduction in the study by Verdaguer-Casadevall et al. where 2-3 hours were spent compared to the approximately 30 min for this study and that by Hori et al. In our own studies we observed significant deactivation of the activity and a shift in product selectivity when measuring more than half an hour. We attributed this deactivation to poisoning of the electrode by Si dissolved from the glass cell due to the alkaline electrolyte. This is discussed in detail in the next section. As Verdaguer-Casadevall et al. and Hori et al. also measured in glass cells it is likely that they experienced the same deactivation behaviour. The data points from Verdaguer-Casadevall et al. could therefore represent deactivated Cu, while the point from Hori et al. more likely resembles the true activity of Cu. Figure 4.2 includes a point at -0.5 V which was measured after deactivation in Ar saturated electrolyte. This is closer to the activity obtained by Verdaguer-Casadevall et al.

4.3 Deactivation

Looking at the insert in Figure 4.1b, which shows the chronoamperometry traces for the ca. 30 min experiments, a slight decrease in activity is observed at -0.4 and -0.5 V, with -0.59 V appearing stable. When measuring for more than 30 min we would observe significant deactivation at all the measured potentials. This is illustrated in Figure 4.4 The total current density and the CO reduction current density is shown with the corresponding concentrations of gaseous and liquid products as a function of total passed charge at -0.52 V. The trace in Figure 4.4a is an example from a single measurement. An initial stable region is followed by deactivation and then finally a stable region appears again. The deactivation profile would vary somewhat in shape from measurement to measurement but the time before initial deactivation was quite consistent. The points at 0.5, 1.0, 4.0 and 6.0 C were measured once and 2.0 C three times. 1-propanol was not detected above the detection limit and acetate which was expected to be around 1 % was not measured for this experiment.
Deactivation was seen to initiate at around 2 C of passed charge corresponding to approximately 30 min. The concentrations of CO reduction products appear to increase linearly with charge before the point of deactivation but do not increase significantly after this point indicating that the electrode has stopped producing these products in appreciable amounts. The concentration of H_2, however, is seen to continue increasing linearly with charge and possibly with a small increase in slope around the deactivation point. The HER activity does therefore not appear to be influenced greatly by the mechanism causing deactivation for the CO reduction reaction.
The deactivation could be attributed to several effects; i) deposition of impurities from the electrolyte, ii) structural change of the catalyst surface under reaction conditions, iii) self-poisoning of the surface by intermediates or products of the reaction. Poisoning by impurities present in the electrolyte has been shown to be an issue as dissolved metal cations can deposit on the surface and change the catalytic activity [128, 129]. As Cu is the only metal capable of CO_2 and CO reduction to further reduced compounds this would result in a decrease in CO reduction activity. Even with very pure electrolyte the use of alkaline electrolyte with glass cells has been observed to be an issue as metal ions and Si dissolves from the glass [130–132]. We performed XPS measurements on our Cu electrodes after CO reduction to check for deposited impurities. Figure 4.5 shows a survey spectrum of a Cu electrode after 17 hours of CO reduction. Only Cu was detected in the survey. A scan of the Si2p region showed increasing amounts of Si as a function of reduction time. This would seem to indicate that the dissolution of Si from glass due to the alkaline electrolyte was depositing on the Cu electrodes

over time.

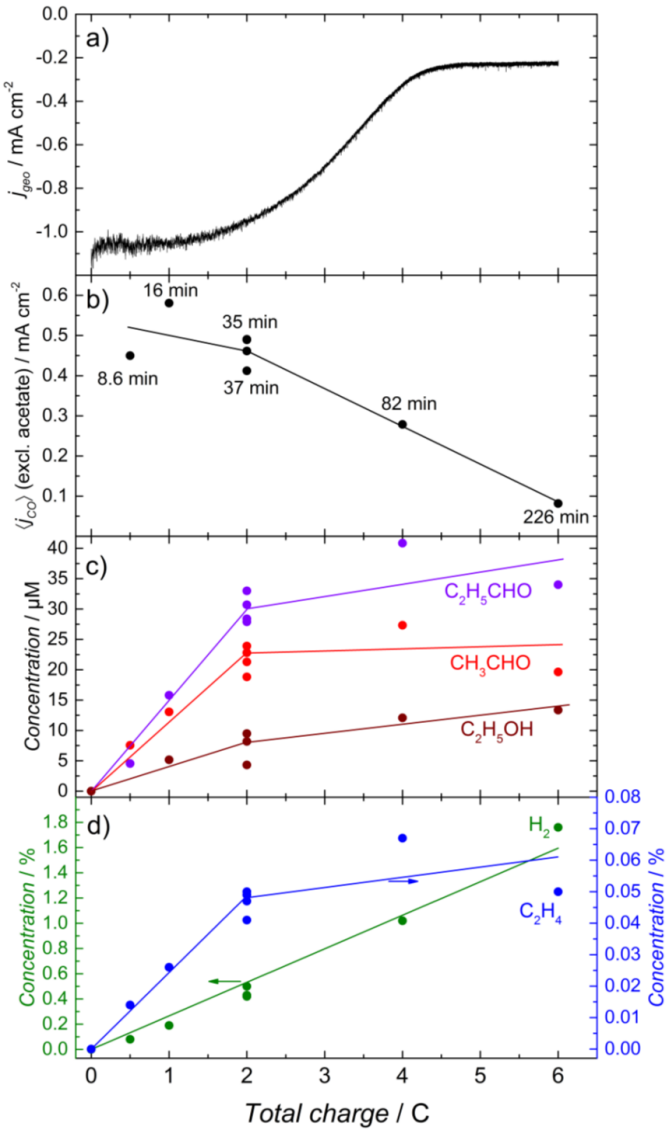

Figure 4.4: CO reduction on polycrystalline Cu in 0.1 M KOH at -0.52 V. a) Representative chronoamperometry trace for a 225 min experiment shown as a function of charge. b) Mean CO reduction activity at different total charges. c) Concentration of liquid products: ethanol, ethanal and propanal as a function of total charge passed. d) conentration of gaseous products as a function of total measurement charge. Lines are a guide to the eye.

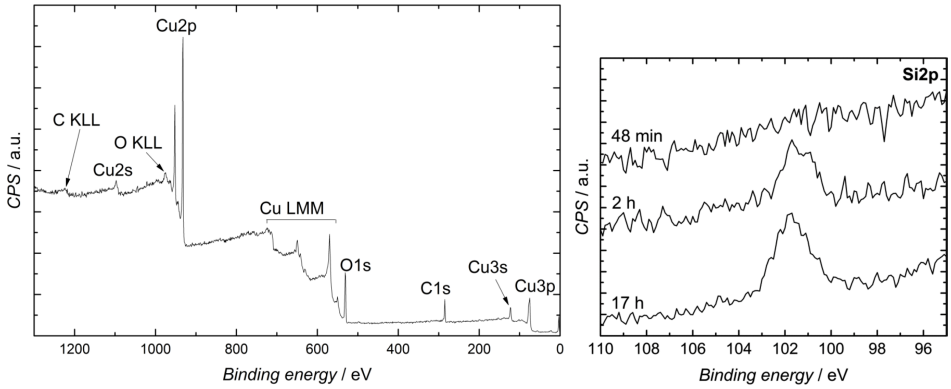

Figure 4.5: XPS of polycrystalline Cu samples after Co reduction at -0.5 V in 0.1 M KOH. Left: Survey spectrum of electrode after 17 hour measurement. Right: The Si2p region as a function of increasing measurement duration.

Deactivation due to self poisoning of the surface by the products has previously been observed for electrooxidation of ethanol on Pt where aldehydes were produced with high selectivity [133]. It was also previously shown in our lab that aldehydes can undergo organic reactions and polymerise in alkaline solutions [127]. As we were producing aldehydes we tested whether they were causing the deactivation. We ran reduction experiments at -0.5 V in Ar saturated 0.1 M KOH with 200 μm of both ethanal and propananal. The current trace is shown in Figure 4.6. An initial increase in current density was observed which indicated that the surface was not immediately poisoned by the aldehydes. After 30 min deactivation was seen in line with the CO reduction experiments.
We also ran the reduction experiment in Ar saturated 0.1 M KOH at -0.5 V for 255 min before changing to CO. The experiment is shown Figure 4.7. An initial activation was seen in Ar saturated electrolyte but deactivation occurred over time. After switching to CO, the sample was clearly deactivated. The product distribution for the CO reduction measurement after deactivation in Ar is in the insert of Figure 4.7. Almost no CO reduction activity was observed. As the deactivation also occurred in Ar saturated solution where H_2 evolution is expected to be the only reaction, this indicated that the deactivation was not related to poisoning by intermediates.
Structural changes for Cu have previously been observed with in-situ STM under CO_2 and CO reduction conditions [30, 32, 134]. The activity of Cu is known to depend on the surface facet [106, 134–137]. Restructuring due to reaction conditions could be occurring on our electrodes but the experiments performed here were not conclusive on that point as deactivation occurred in both Ar and CO saturated electrolyte. In situ techniques that can monitor the surface structure

during the reaction would be more suited for answering these questions.

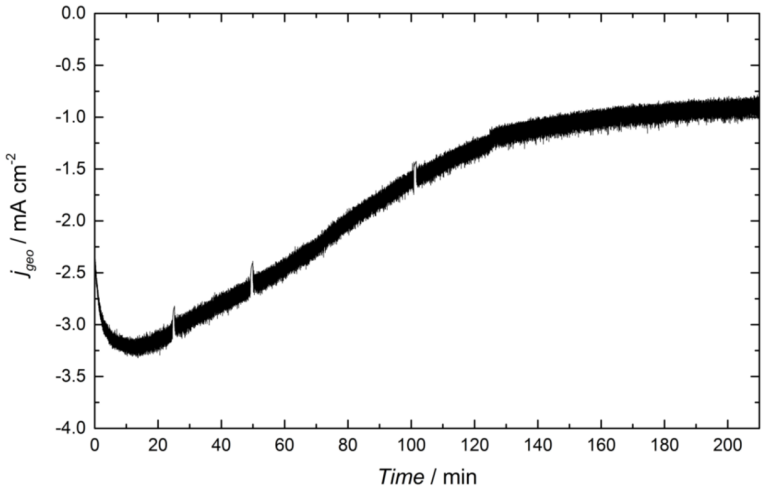

Figure 4.6: Reduction of 200 μM of both ethanal and propanal in Ar saturated 0.1 M KOH at -0.5 V.

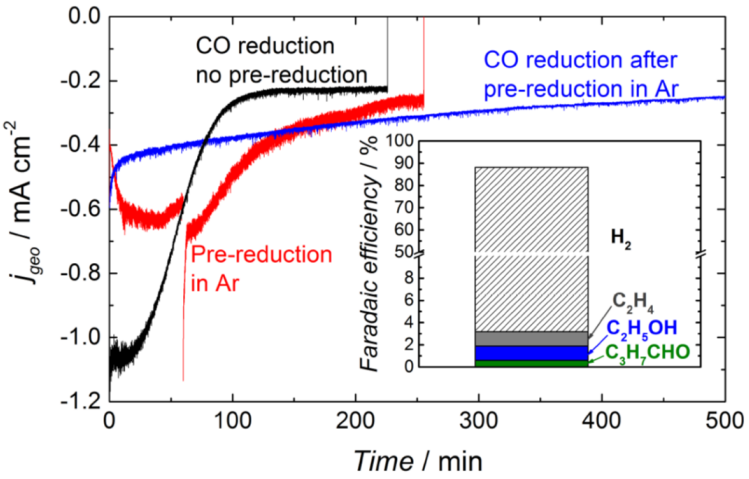

Figure 4.7: The effect of pre-reduction in Ar. CO reduction at -0.5 V in 0.1 M KOH after pre-reduction in Ar (blue), pre-reduction in Ar (red), and regular CO reduction without pre-reduction for comparison (black). Insert shows the Faradaic efficiencies CO CO reduction after pre-reduction in Ar. Figure courtesy of Erlend Bertheussen.

4.4 Conclusion

The activity and selectivity of polycrystalline Cu for CO reduction in 0.1 M KOH was investigated at potentials of -0.4. -0.5 and -0.59 V vs RHE. More than 50 % Faradaic efficiency towards CO reduction products was observed with high selectivity towards C_2 and C_3 aldehydes and alcohols as well as ethene. These results showed similar activity to previously reported data on nanostructured oxide-derived Cu when normalised to ECSA indicating that the high activity of nanostructured Cu catalysts is an effect of increased surface area rather than an increase in the intrinsic activity of Cu. It would thus be beneficial to study how to enhance the intrinsic activity of Cu. Oxide derived Cu shows higher selectivity towards alcohols compared to planar Cu, which could be attributed to a combination of i) different available potential windows for different roughness factors, ii) increased readsorption and reduction of aldehydes in the the porous structure, iii) more undercoordinated sites.
For measurements carried out in excess of ~ 30 min we observed deactivation in CO reduction activity and selectivity. We attributed this mainly to Si which was detected on the electrodes and is a result of the corrosion of the glass cell in alkaline electrolyte. This could also be the case for previous studies by other groups using glass cells in alkaline electrolyte for extended measurement times and explain the large variation observed between datasets. Poisoning of the surface by intermediates or products of the reaction and restructuring of the surface could also cause a change in activity. These phenomena could not be properly investigated in the current setup, although poisoning from intermediates seemed unlikely, and thus other in situ techniques would be required. Synchrotron X-ray techniques for monitoring the crystal structure and infrared spectroscopy for monitoring adsorbates would be two such in situ techniques as described in subsequent chapters.

Chapter 5

In situ grazing incidence X-ray diffraction of Cu under CO reduction conditions

In order to get a true picture of the catalyst during the reaction, in situ experiments must be performed rather than ex-situ characterisation prior to or following the reaction. We investigated the surface crystal structure of Cu catalyst under CO reduction conditions by in situ grazing incidence X-ray diffraction (GIXRD).
The main results are presented in the published paper with the title "Absence of Oxidized Phases in Cu under CO Reduction Conditions" which is attached at the end of the thesis. The experimental work was undertaken at the Stanford Synchrotron Radiation Lightsource (SSRL) at the SLAC National Accelerator Laboratory. The project was initiated by Erlend Bertheussen who wrote the beam time proposal under supervision of Ifan Stephens and Ib Chorkendorff. The experiments were performed by myself, Soren Scott, Thomas Maagaard and Erlend Bertheussen (PhD students at SurfCat, DTU) in collaboration with Alan Landers and John Lin (PhD students in the Jaramillo group at Stanford). Other parties involved in planning, conducting and interpretation of the experiments include Associate Professor Brian Seger (DTU), Staff Scientists Chris Hahn and Drew Higgins (Jaramillo group, Stanford), beam line scientists Apurva Mehta and Ryan Davis (SSRL, SLAC). Additionally, Staff Scientists Walter Drisdell and Jeffrey Beeman (Berkeley, CSD) were involved with the original design of the in situ cell and for cell assembly at Berkeley. Initial data analysis was performed by Soren Scott, myself, Thomas Maagaard and Erlend Bertheussen. Further analysis was mainly performed by Soren Scott using a python script he wrote called "EC-Xray".

Soren Scott and I wrote the initial manuscript of the paper and all the authors helped with revisions.

5.1 Introduction

As presented in in Chapter 2 there is an ongoing discussion about the role of oxygen on the catalytic performance of Cu (Section 2.8) and restructuring of the Cu surface during reaction conditions has been observed (Section 2.4).
The use of grazing incidence X-ray diffraction (GIXRD) allows for the observation of the crystalline phases of the topmost layers of smooth metallic films. This occurs because measurements in total external reflection geometry, where the incident angle is below the critical angle (grazing incidence), give rise to an exponentially decaying wave probing mainly the surface layers [102]. When performing in situ measurements on electrochemical systems, the X-ray beam must pass through and exit the electrolyte layer before and after reaching the electrode. Maintaining a significant signal in this configuration requires the use of a synchrotron source. The penetration depth is dependent on the incidence angle, allowing for depth analysis and comparison of bulk vs surface values. Also see Section 3.4.
Studies using surface sensitive X-ray diffraction techniques for in situ electrochemistry have focused on single crystals using crystal truncation rod (CTR) [138–140]. Very few studies have reported the use of in situ X-ray diffraction for electrochemistry on polycrystalline materials [141], and none to our knowledge in grazing-incidence configuration. Other studies of oxide reduction on Cu prior to the onset of CO or CO_2 reduction include in situ X-ray absorption spectroscopy [142] and Raman spectroscopy [59]. These techniques do not show the same high time-resolution and surface sensitivity of the GIXRD technique applied here.
Here we used GIXRD to monitor the crystal phases at the surface of polycrystalline Cu thin films in 0.1 M KOH saturated with either Ar or CO. We monitored the reduction of the native oxide in the initial cathodic scan and the change in facet distribution at the cathodic potential. Details of the experimental procedure can be found in Section 3.4.

5.2 Reduction of native oxide on Cu

5.2.1 Diffractograms

Diffractograms of the full 2θ range (2θ from 12 to 60°) were acquired of the dry samples and of the samples in electrolyte at fixed potential prior to and following the reduction of the native oxide (in either CO or Ar saturated electrolyte). These

Phase	Cu									Cu_2O	CuO	$Cu(OH)_2$
(hkl)	(111)	(200)	(220)	(311)	(222)	(400)	(331)	(420)	(422)	(111)	(111)	(021)
$2\theta/°$	20.1	23.3	33.2	39.1	40.9	47.6	52.2	53.6	59.2	16.9	18.1	16.0

Table 5.1: Expected Bragg reflections and angles from Cu and its oxidised phases using Bragg's law with a photon energy of 17 keV.

were acquired at both the shallow and the bulk incidence angles of $\alpha = 0.15°$ and $\alpha = 0.20°$, resulting in respective attenuation lengths of approximately 2.5 and 20 nm. An example from a sample reduced in CO is shown Figure 5.1. The expected diffractions from metallic Cu and its oxidised phases, Cu_2O, CuO and $Cu(OH)_2$ are shown in Table 5.1.

Figure 5.1a shows diffractograms before (blue line) and after (brown dotted line) the initial cathodic scan at the most grazing angle ($\alpha = 0.15°$) and the dry sample for comparison (black line). Sharp peaks are apparent at the expected positions for metallic Cu, which are indicated on the top x-axis. The broad peak centred at $2\theta = 13°$ is attributed to diffraction from the electrolyte whereas the broad peaks at $2\theta = 27°$ and 38° are attributed to the substrate and are observed also in the dry scan.

The insert shows a zoomed in region containing the $Cu_2O(111)$, Cu(111), Cu(200) reflections. The presence of a peak at the $Cu_2O(111)$ reflection is clearly observed prior to the reduction and is gone after the reduction. In general for all samples (see Figure S3 of the article appended in at the end of the thesis for the remaining samples), no oxide peak is visible at the $Cu_2O(111)$ reflection after the reduction. The intensity of the oxide peak prior to reduction varies a lot from sample to sample. This could be due to different amounts of time spent at OCP initially, resulting in varying thickness and/or crystallinity of the oxide.

Panel b) shows the diffractograms prior to and following reduction but at the bulk angle ($\alpha = 0.20°$). Higher intensity is observed for the metallic Cu peaks as would be expected when more of the Cu is probed by the beam. There is no discernible oxide peak for the $Cu_2O(111)$ reflection at this angle indicating that oxide is located in the topmost monolayers at the surface.

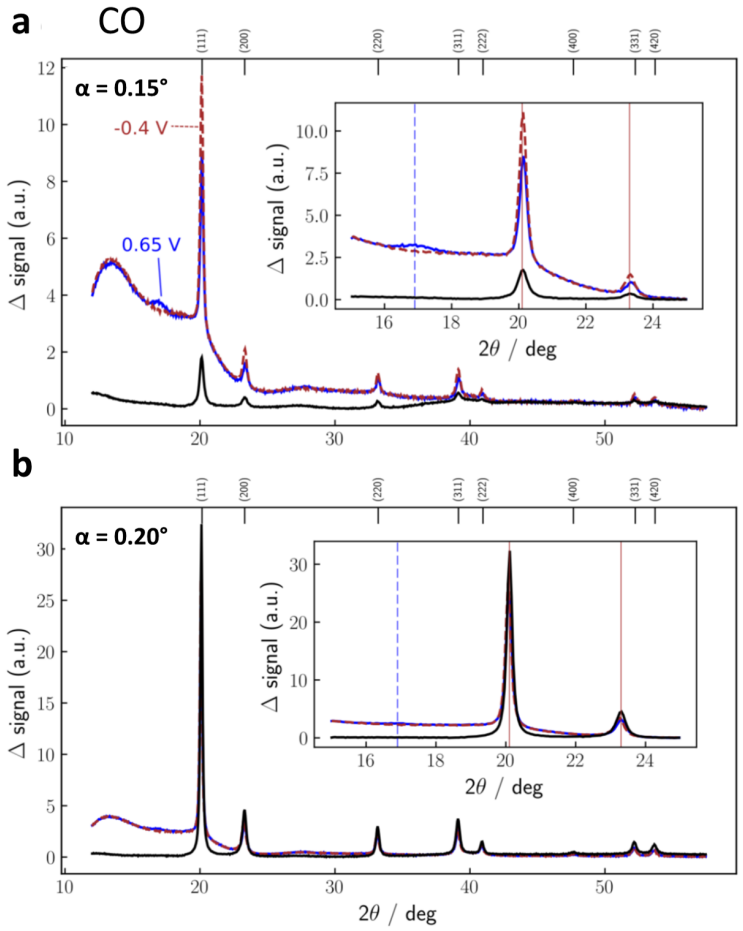

Figure 5.1: Diffractograms of a polycrystalline Cu thin film in CO saturated 0.1 M KOH. a) Incident angle α = 0.15°. b) Incident angle α = 0.20°. Black lines are measured on the dry sample. Blue lines are measured before the reduction at -0.65 V vs RHE. Brown line are measured after the reduction at -0.4 V vs V RHE. The top x-axis indicates the reflections for metallic Cu. Inserts show a zoomed in region for 2θ = 15 to 25° which includes the Cu(111) and Cu(200) reflections marked with Cu coloured lines and the Cu_2O(111) reflection marked with a stippled blue line.

5.2.2 Timescans

The native oxide on Cu samples was reduced with an incident angle of α = 0.15° and the detector held stationary and centred at 2θ = 18.5°. This meant that the Bragg rings for both the Cu(111) reflection at 2θ = 20.1° and the Cu_2O(111) reflection at 2θ = 16.9° were incident on the detector. An example is shown in

Figure 5.2a for a sample in Ar saturated electrolyte. The intensity of the Bragg angle is plotted as a function of angle and time with the accompanying potential and current shown in the lower panel. The angle corresponding to the oxide ($Cu_2O(111)$) centred at 2θ = 16.9° is seen to have intensity initially but then fades as the potential is scanned cathodically. Simultaneously the metal (Cu(111)) centred 2θ = 20.1° increases in intensity. The oxide and metal regions have been separated in the colour map due to the relatively low intensity of the oxide but all the indicated angles were measured simultaneously on the 2D detector. The corresponding diffractograms before and after the reduction are shown in panel b).

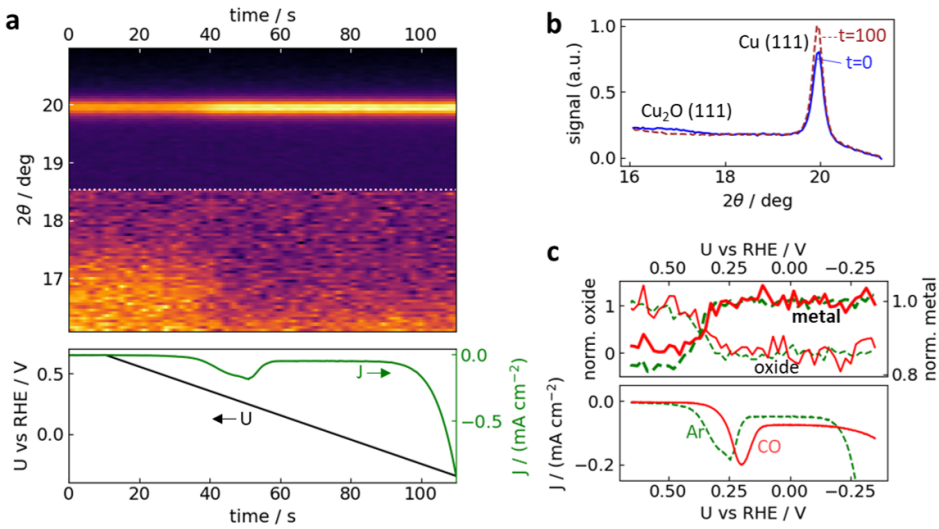

Figure 5.2: Reduction of the native oxide. a) Diffraction intensity as a function of 2θ and time during the first cathodic sweep from +0.65 to -0.4 V vs RHE in Ar saturated 0.1 M KOH. α = 0.15°. The white stippled line splits the diffraction data for better visibility on the color map. The accompanying current and potential is plotted in the lower panel. b) The corresponding diffractograms before (blue) and after (stippled brown) the reduction. c) The normalised integrated metal (thick) and oxide peaks (thin) as a function of potential shown for the same sample in Ar (stippled green) and a different sample in CO (solid red). The corresponding currents are shown in the lower panel.

In panel c) the intensity of the metal and oxide peak is plotted against potential. The corresponding intensities for a sample reduced in CO is also plotted. The intensities have been normalised to the final area of the metal peak and the initial area of the oxide peak, respectively. The lower panel shows the corresponding current. The integrated currents for the reduction waves correspond to 2.0 and 1.8 nm thick Cu_2O layers for the Ar and CO sample, respectively, in line with

previous studies of oxide growth on Cu surfaces at room temperature [143].

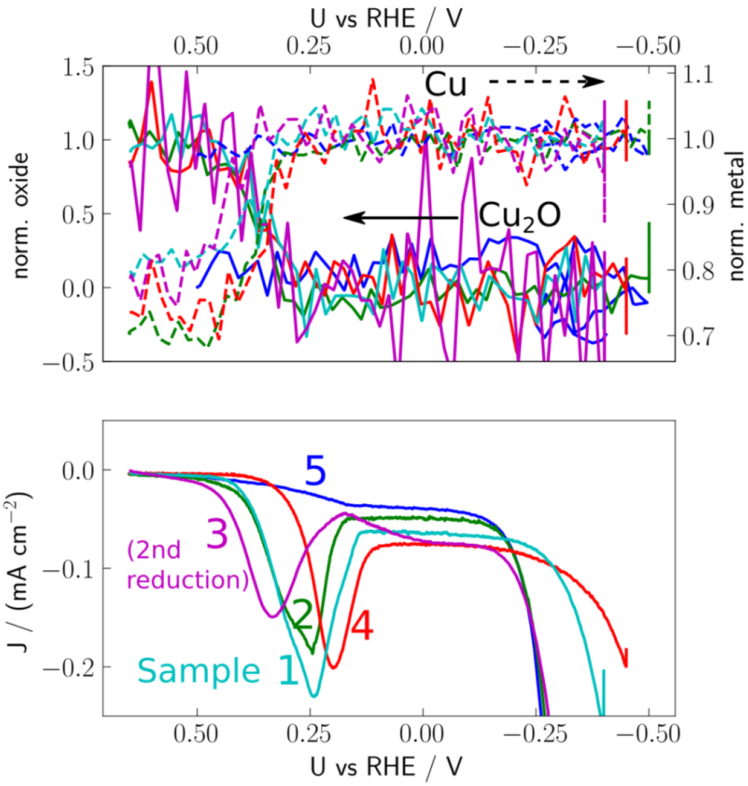

Figure 5.3: Reduction of the native oxide for all samples. The normalised integrated metal (full) and oxide peaks (stippled) as a function of potential shown for all samples. Corresponding currents shown in lower panel. Samples 1, 2, 5 in Ar and 3, 4 in CO. See text for details.

The oxide and metal peak intensities during the reduction are shown for all the samples in Figure 5.3. The reduction as observed by the disappearance of oxide signal is seen to be quite similar for the Ar and CO saturated cases and is also seen to coincide with the increase in metal intensity (by approximately 20 %). Samples 1-4 were held at +0.65 V vs RHE prior to reduction in order to stabilise the native oxide. Sample 5 was held at +0.5 V vs RHE, however, and no oxide reduction or metal increase was observed as it had already been reduced. The oxide is clearly visible in the full diffractogram before the timescan as seen in Figure S3i of the supporting information (see appended). This indicates a slow reduction at +0.5 V after the diffractogram but before the timescan. For sample 3

the second cathodic sweep was used due to experimental error during the first scan. The sample was held at +0.65 V vs RHE for 2 hours before the second reduction. Looking at the currents, a large spread is observed in the size and position of the reduction wave (none is observed for sample 5). Samples 1 and 2 in Ar are similar in position, occurring slightly before the wave for sample 4 in CO. The electrochemical reduction wave is seen to occur earlier (more anodic) for sample 3 (CO) possibly due to the oxide being formed electrochemically as discussed above.

The increase in the metal peak intensity was informative. A non-crystalline oxide phase of Cu would not give a sharp XRD peak but would mask the underlying metallic Cu. The abrupt increase of the metal peak to full intensity at 0.4 to 0.3 V indicated that no such phase was present and that all oxidised phases had been reduced at the CO reduction relevant potentials. Otherwise, the phase would have to be stable in the entire potential range from +0.3 to -0.4 or -0.5 V vs RHE. This is evidence against a significant amount of a sub-stoichiometric phase of oxidised Cu. We cannot, however, rule out minute amounts of oxygen dissolved in the Cu lattice. The GIXRD method also cannot determine the oxidation state of the surface monolayer on polycrystalline samples and other techniques would be required (GIXAS or AP-XPS).

Interestingly, there was a large spread in the position of the electrochemical reduction waves compared to the small spread for the change in GIXRD intensity. The alignment of the electrochemical and GIXRD datasets was ensured by the use of a TTL trigger between the X-ray data acquisition and the potentiostat. The temporal separation of the GIXRD signal and the electrochemical reduction wave could provide information on the reduction mechanism but further studies would be needed to clarify this.

A substantial spread in the current density at the cathodic potentials was observed for the different samples. Sample 1 (-0.4 V vs RHE in Ar) and sample 4 (-0.5 V vs RHE in CO) were ~ -0.2 mA/cm^2 and ~ -0.18 mA/cm^2, respectively, which is in line with previous results on polycrystalline Cu in 0.1 M KOH [97]. The other samples show much higher current densities which could be a result of metal deposition from the counter electrode. This was observed for sample 2 where a Au(111) signal could be detected after 1 hour at -0.5 V vs RHE. Pt was used as the counter electrode for sample 3. No Pt signal was observed in this case but even very small amounts would result in large HER activity.

The possible deposition of metal from the counter electrode, although unfortunate, does not change the fact that there was no oxide on the samples at the reductive potentials relevant for CO reduction.

5.3 Electrochemically induced faceting

XRD probes planes corresponding to reciprocal lattice vectors coinciding with the Q-vector bisecting the incident and diffracted beams [102]. While the Q-vector does not coincide with the macroscopic surface normal of the sample in GIXRD geometry (Figure 3.8 left), it is only off by about 10° for the peaks of interest. Thus, given the low penetration depth, this means that the ratio of peak intensities in GIXRD relates to the surface faceting of a polycrystalline sample. This concept is illustrated in the Supplementary Information Figure S5 of the article (see appended).

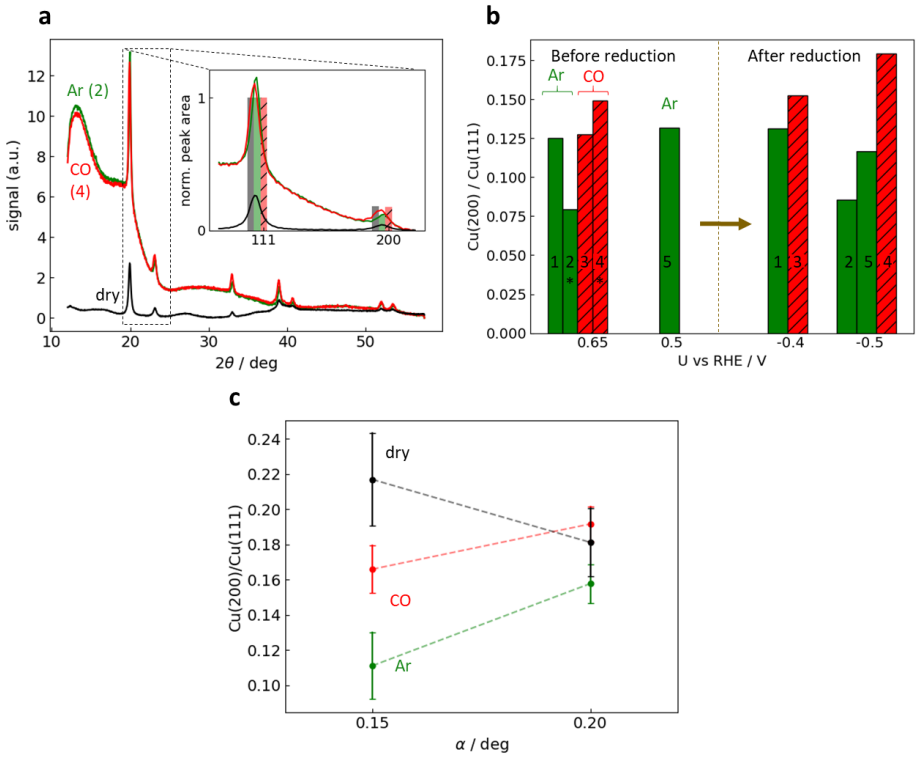

Figure 5.4: Faceting during electrochemistry. a) Representative scans at α = 0.15° for the dry sample and the a sample in CO and Ar saturated 0.1 M KOH. Insert shows the integrated intensities for Cu(111)and Cu(200) normalised to Cu(111) overlaid on the relevant 2θ region. b) The ratio of the Cu(200) and Cu(111) reflections prior to and following reduction. c) Grouped results for dry spectra, spectra in Ar and spectra in CO. The means and the standard deviations of the grouped data points are plotted for α = 0.15° and 0.20°. Lines are a guide to the eye.

Using the above argument, the influence of the electrochemical environment on the surface structure of the Cu samples was investigated by comparing the peak intensities for the Cu(111) and Cu(200) reflections as measured in the diffractograms before and after reduction. Due to the large variation in absolute intensity for the reflections between samples, the relative intensity for each measurement, presented as the ratio Cu(200)/Cu(111), was compared.
Figure 5.4b shows the Cu(200)/Cu(100) ratio at $\alpha = 0.15°$ before and after the reduction. Prior to reduction the ratio was similar in Ar and CO. Following reduction, an increase in the ratio was observed for the samples in CO saturated electrolyte but not for Ar saturated electrolyte. This indicates a trend towards (100)-like facets on the polycrystalline Cu surface under CO reduction conditions. Figure 5.4c shows the ratios following reduction and how they converge for the bulk angle ($\alpha = 0.20°$) as expected, illustrating that the electrochemically induced faceting is confined to the surface layers. Similar reconstruction of polycrystalline Cu during CO_2 reduction has been observed with STM [32], where the polycrystalline surface first reconstructed to (111) and then (100). CO has also been shown to increase the surface mobility of Cu [33]. This CO-promoted reconstruction to (100)-like surfaces could explain the high selectivity of polycrystalline Cu for ethylene during CO reduction as is also observed for stepped (100) surfaces [17].

5.4 Conclusion

In situ grazing incidence X-ray diffraction (GIXRD) was used to monitor the reduction of the native oxide on polycrystalline Cu in alkaline electrolyte in real time. The Cu_2O(111) diffraction peak was seen to disappear completely during the reductive scan at around 0.3 V vs RHE and the metal Cu(111) peak simultaneously reached full intensity without further increase at more cathodic potentials. This is strong evidence that there is no phase besides metallic Cu at the surface at potentials relevant for CO reduction. Hopefully, these results will help to clarify the ongoing debate about oxidised Cu phases in the CO and CO_2 reduction community.
We additionally observed faceting induced by the electrochemical environment. Comparison of the Cu(200) to Cu(111) peak ratio in Ar and CO saturated electrolyte indicated a trend towards CO-promoted formation of (100)-like facets on the Cu surface at cathodic potentials. This is consistent with previous reports using STM and helps explain the high selectivity of polycrystalline Cu towards ethylene as is also observed with Cu(100) single crystals.

Chapter 6

ATR-SEIRAS

To investigate the adsorbates on the surface of polycrystalline Cu it was decided to initiate surface enhanced IR at SurfCat. To get an initial feeling for the ATR-SEIRAS technique, I undertook an external stay at the Electrochemical Energy Laboratory (EEL) at Massachusetts Institute of Technology (MIT) which is lead by Professor Yang Shao-Horn. Here, Yu Katayama introduced me to the basic principles and procedures of the technique. At the time of my external stay, Yu Katayama was a visiting PhD student from Kyoto University, Japan, who had specialised in ATR-SEIRAS during his studies. He is currently an Assistant Professor at Yamaguchi Univeristy, Japan. During a visit to DTU he helped with initiating ATR-SEIRAS at SurfCat.

In the following, 5 sections will deal with various work performed related to CO and CO_2 reduction with ATR-SEIRAS. The first section is CO bands on a Pt film sputtered with 20 nm Cu, the second deals with CO on Pt, the third with CO on Cu and the fourth with CO on Au. The fifth section discusses some experiments that were not included here as well as possible improvements to the experimental setup. The experimental parts relating to synthesis of the films and cell configurations are given in Section 3.5.5.

6.1 CO on Cu on Pt

During my external stay at MIT, it was attempted to monitor CO on Cu during CO reduction. Direct sputtering of Cu onto a Si hemisphere did not adhere. Yu Katayama had extensive experience with synthesising Pt SEIRAS films with good SEIRAS enhancement. Thus, it was decided to sputter a thin layer (20 nm) of Cu on top of such a film and use that for CO reduction. The Pt film was synthesised by Yu Katayama and the Cu sputter deposition by Jonathan Hwang. The experiment was performed in 0.1 M KOH saturated with either Ar or CO.

Figure 6.1a shows the switch from Ar to CO purging at OCV. The background was taken at OCV before introduction of CO. Three peaks appear in the spectra, corresponding to CO bound on Cu (2082 cm^{-1}) and on Pt in the on top and bridge configurations (2006 and 1844 cm^{-1}, respectively). The appearance of peaks related to Pt clearly indicates exposed Pt on the surface. This could be due to pinholes in the Cu overlayer but is more likely due to the extremely strong interaction between Pt and CO resulting in the CO environment pulling Pt to the surface. The process possibly initiated at pinholes in the Cu film. This behaviour has been observed previously in our group for Cu overlayers on Pt [144].

Figure 6.1b shows the spectral dependence upon potential when going from 0.0 to -0.6 V vs RHE and back. The current for the CV is shown in Figure 6.1c together with the same potential window in Ar. As expected, the current is lower in CO saturated solution. No bands were observed in Ar in the spectral range of interest shown here. The bands for CO on Pt have the expected redshift (towards lower wavenumbers) when going cathodic in potential and the positions at 0.0 V vs RHE, as indicated by the stippled lines, correlate to values reported elsewhere [123, Figures 2 and S6]. The slope of the stark shifts as seen in Figure 6.1d are approximately 67 and 54 $cm^{-1}V^{-1}$ for CO atop and bridge bound, respectively, which is higher than reported in [123] (52 and 26 $cm^{-1}V^{-1}$, respectively). This could be an effect of the Cu altering the CO binding on Pt slightly. However, the cited study used 1 M KOH in place of 0.1 M KOH and measured from 0.05 vs RHE and positive resulting in the potential ranges for the studies not matching. The Cu peak around 2082 cm^{-1} is consistent with previous reports of CO on Cu [71, 80]. The intensity of the CO on Cu peak is extremely low, making it hard to judge the stark shift. It appears to be around 15 $cm^{-1}V^{-1}$ which is about half of the value reported for CO on Cu in [80] (30 $cm^{-1}V^{-1}$) but similar to that reported in [145] (15 $cm^{-1}V^{-1}$).

The experiment illustrated an interesting surface phenomenon using SEIRAS,

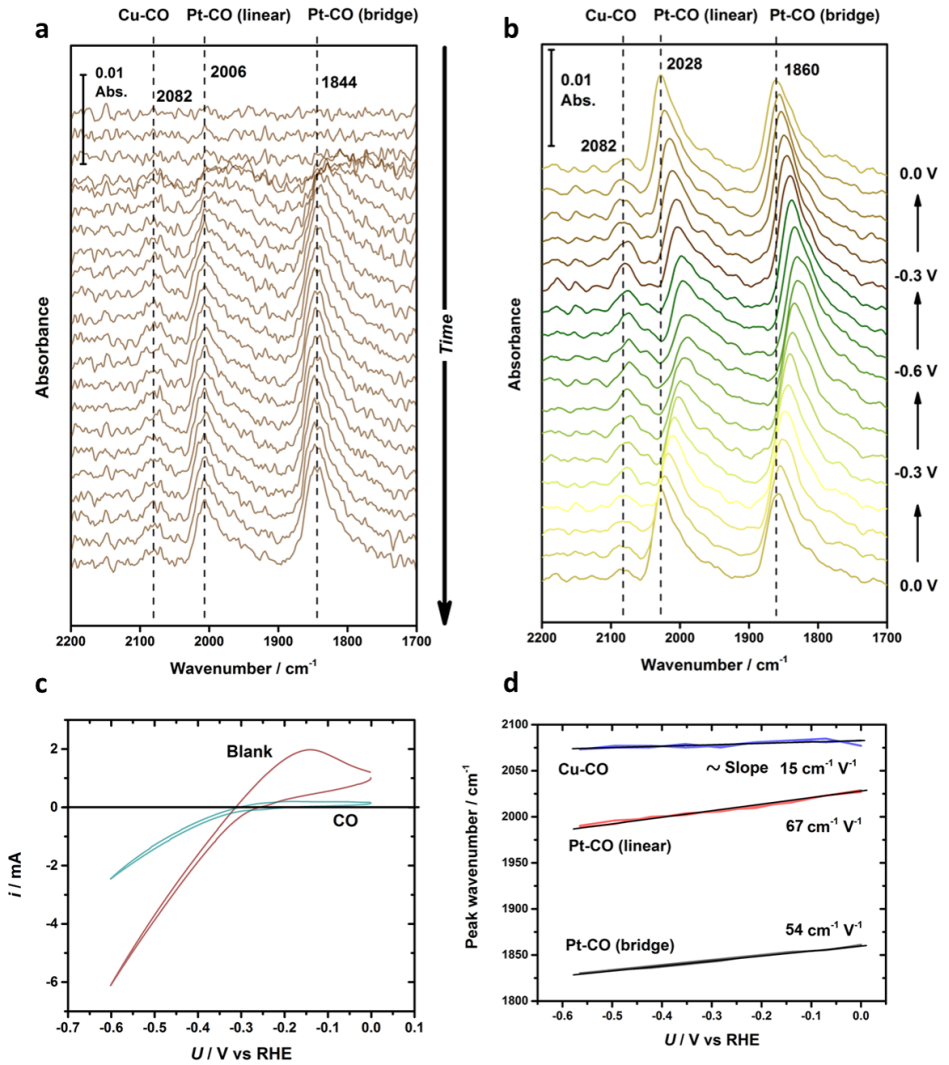

Figure 6.1: a)Introduction of CO at OCV in 0.1 M KOH on a Cu sputtered Pt SEIRAS film. b) 10 mV/s CV in CO on the same film. c) Current for the CV in Ar and CO. d) Stark shifts from b).

where the strong Pt-CO bond pulls Pt to the surface despite a Cu overlayer. The film configuration was, however, not useful for studies of CO reduction on pure Cu and was therefore not pursued further. Film synthesis using only Cu was decided upon for further experimentation as described in the following sections.

6.2 CO on Pt

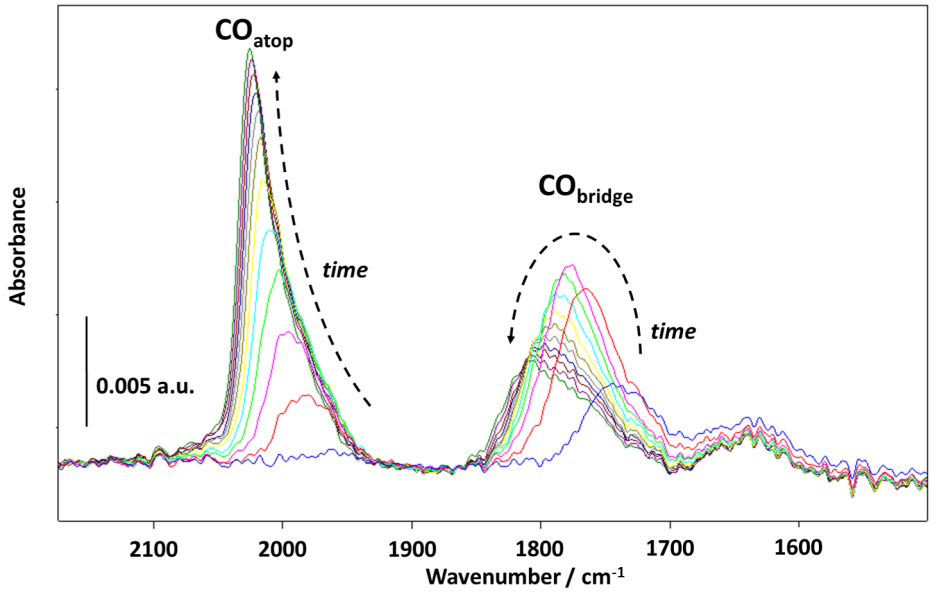

Figure 6.2: Introduction of CO_2 at OCV in 0.1 M KOH on an Pt electroless SEIRAS film. The spectral evolution with time is indicated. Each spectrum is approximately 20 seconds apart and is an average of 20 s.

During the initial phase of setting up ATR-SEIRAS at DTU, we used Pt films to test the equipment. Thus, reactions of Pt are not a theme of this thesis but have been included here for completeness and to give an idea of the variability of the infrared signature on different metals.

The following example is of a Pt film in 0.1 M KOH. The one-compartment cell with a Pt CE was used. Holding the potential at OCV, the electrolyte was initially purged with Ar and a background spectrum was acquired. Spectra were acquired as the electrolyte was purged with CO_2 as seen in Figure 6.2. Notice the initial increase in CO population on the bridge sites which shifts in favour of the atop sites, presumably as a higher CO coverage leads to a shift in surface configuration. Both peaks were seen to initially shift towards higher wavenumbers which is an effect observed on Pt when going from low to higher coverage due to increased dipole-dipole coupling [109, Chapter 3.6]. Several factors are changing, however, during purging with CO_2. As CO_2 neutralises the KOH and forms $KHCO_3$, the pH changes from ca. 13 to 6.8 [17]. A shift in OCV could also be expected. Unfortunately neither pH or OCV were monitored.

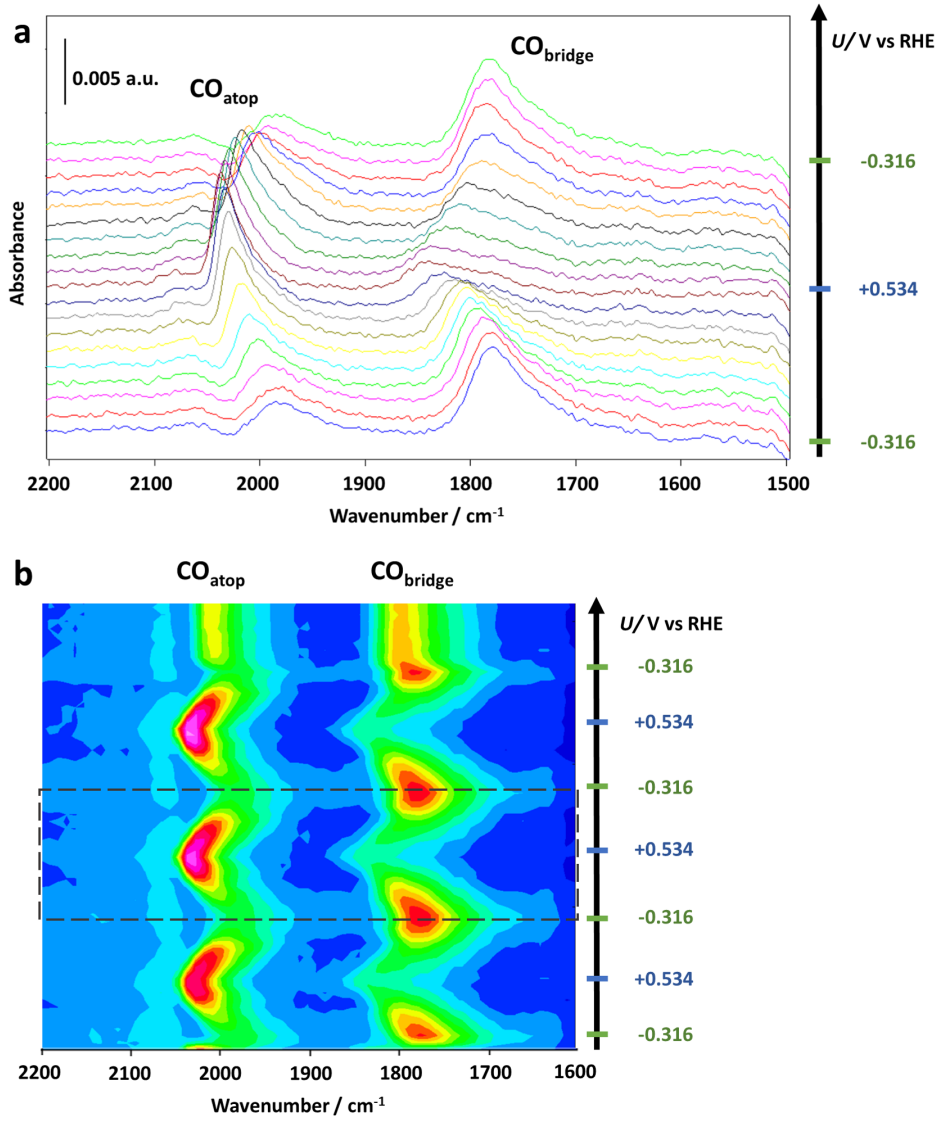

Figure 6.3: CV on Pt SEIRAS film at 20 mV/s in CO_2 saturated 0.1 M KOH between -0.316 and +0.543 V vs RHE (pH assumed to be 6.8). a) Stacked spectra of the CO region for CV cycle 2 out of three. b) Heatmap of all 3 cycles with cycle 2 indicated by stippled box. The choice of potential window is due to a mistake in correcting for the pH change upon saturation of the 0.1 M KOH solution with CO_2.

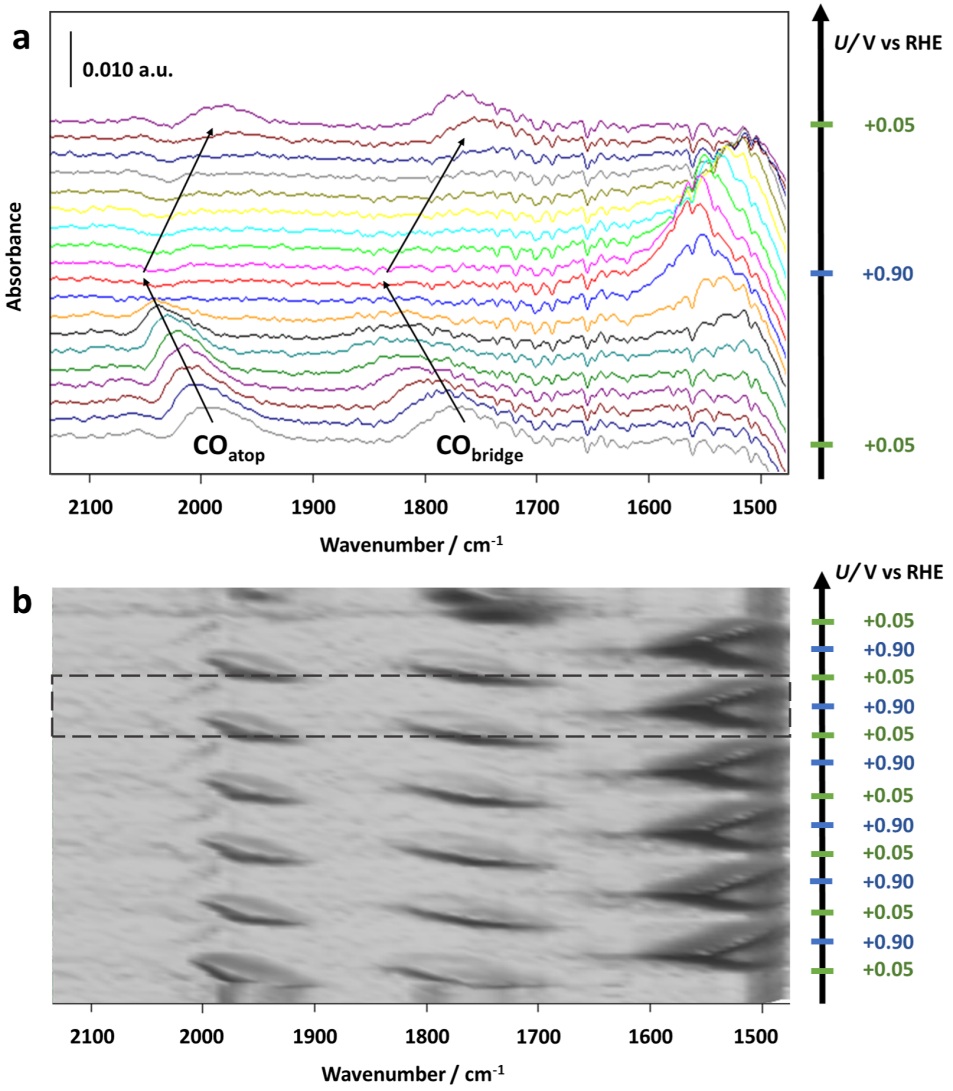

Figure 6.4: CV on Pt SEIRAS film at 20 mV/s in CO_2 saturated 0.1 M KOH between +0.05 and +0.90 V vs RHE (pH assumed to be 6.8). a) Stacked spectra of the CO region for CV cycle 5 out of six. b) Landscape of all 6 cycles with cycle 5 indicated by stippled box.

Under identical conditions and with a film prepared in the same manner, CVs were performed. Figure 6.3a shows the second out of 3 cycles as stacked spectra. An interesting dynamic is seen to occur between the CO_{atop} and CO_{bridge}. Both peaks have the expected Stark shift towards higher wavenumbers with increasing positive potential but as the the CO_{atop} reaches its maximum intensity at the most positive potential (+0.543 V vs RHE), the CO_{bridge} is at its minimum. Figure 6.3b shows a heat map of all 3 cycles and here the reversible conversion between CO_{atop} and CO_{bridge} is clearly observed.
Additional CVs were performed in the range +0.05 to +0.90 V vs RHE as shown in Figure 6.4. When going anodic, both CO peaks are seen to shift to higher wavenumber and then gradually disappear. Between 1600 and 1500 cm^{-1} an additional peak was observed which increased with increasing potential simultaneously with the decrease in the CO peaks. This peak has been attributed to adsorbed COOH formed from adsorbed CO and OH (*CO + *OH -> *COOH) [123]. On the cathodic scan the disappearance of the COOH peak and the return of the CO peaks is not reversible as the COOH peak disappears at more negative potentials than it appeared at. The CO peak does not start to reappear until ca +0.35 V and again it is seen to appear first on the bridge site and then on the atop site.

The experiment indicated a dynamic conversion between the CO_{atop} and CO_{bridge} configurations, where CO_{bridge} is preferred at low CO coverage but then converts to CO_{atop} at higher coverage. The potential also affected the distribution of the two configurations. At more positive potentials the conversion to what is believed to be adsorbed COOH was observed.

6.3 CO on Cu

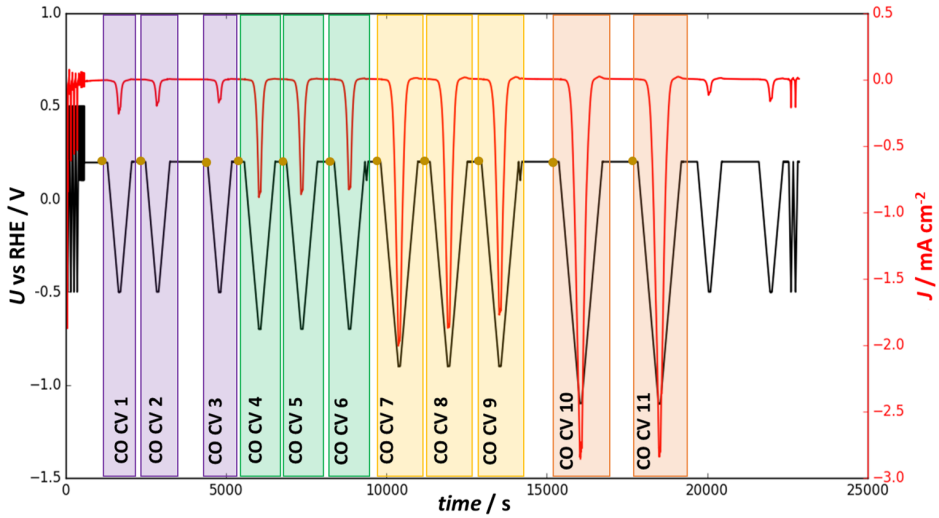

Figure 6.5: Electrochemical program for CO reduction on a Cu SEIRAS film. 2 mV/s CVs in CO saturated 0.1 M $KHCO_3$. Increasing cathodic bounds from -0.5, -0.7, -0.9, -1.1 V vs RHE. Current is normalised to geometric surface area of the electrode (1.23 cm^2). CVs with same potential bounds indicated by colour. Yellow dots indicate that a background was taken at +0.2 V vs RHE.

ATR-SEIRAS measurements of CO reduction on Cu in CO saturated 0.1 M $KHCO_3$ were performed in the two-compartment cell with a Fumasep FAA anion exchange membrane and a Au mesh counter electrode.
Following the initial cycling in Ar saturated solution, a background was taken and CO introduced while holding the potential at +0.200 V vs RHE (-0.372 V vs SHE, pH measured to 9.7), where no CO is observed. After allowing the solution to saturate with CO (1 bar), CVs were measured at 2 mV/s from +0.2 V vs RHE to cathodic potentials of -0.5, -0.7, -0.9, and -1.1 V vs RHE. A spectrum background was taken at +0.2 V vs RHE before the beginning of each CV and each cathodic potential was repeated 3 times. The electrochemical program can be seen in Figure 6.5.
Figure 6.6 shows the full spectrum for the first CV to -0.5 V vs RHE. A peak corresponding to CO_{atop} stretch is observed in the 2040-2090 cm^{-1} region. The initial appearance of the CO stretch band is accompanied by a negative band appearing in the carbonate region around 1540 cm^{-1}, indicating that carbonate is displaced by CO on the surface. The signal due to water in the bulk is also observed as the OH stretch and HOH bend of water at ca. 3400 and 1640 cm^{-1},

respectively. The increase in these bands is attributed to small changes in the film during polarisation.

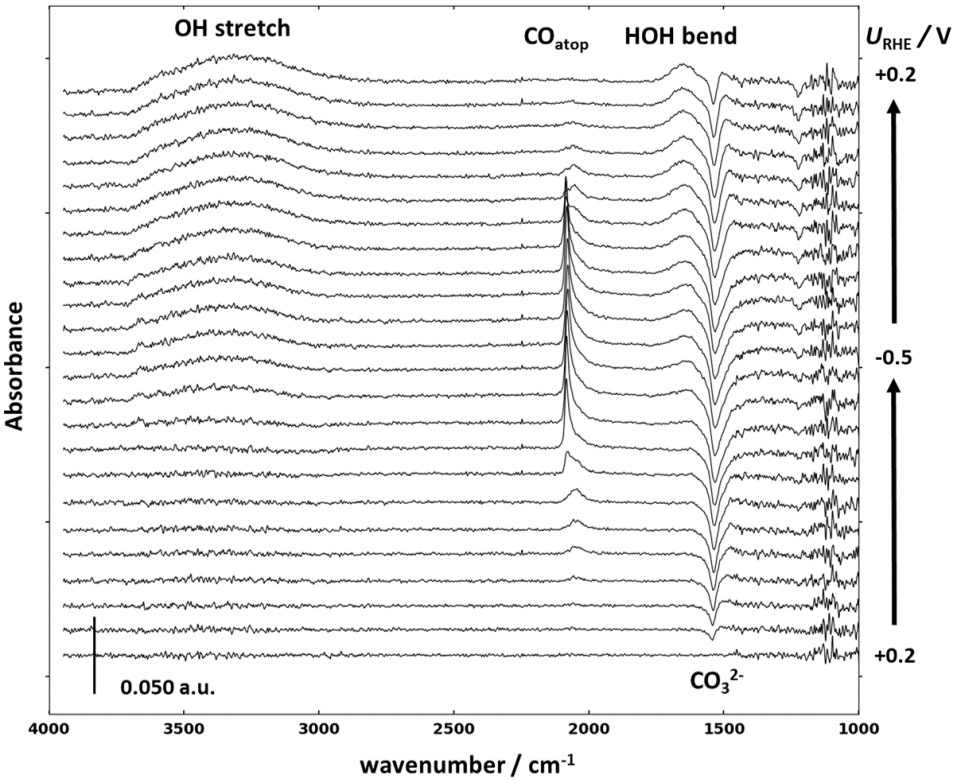

Figure 6.6: SEIRAS spectra corresponding to 2 mV/s CV from +0.2 to -0.5 to +0.2 V vs RHE in CO saturated 0.1 M $KHCO_3$ on Cu. Every 8th spectrum has been plotted resulting in a 64 mV separation. The broad peak at 3400 cm^{-1} corresponds to the OH stretch of water, the sharp peak around 2080 cm^{-1} is the CO stretch of atop bound CO, the peak at 1640 is the water bend, the negative peak around 1540 cm^{-1} is the carbonate ion (desorbing), and the weak negative peak at 1220 cm^{-1} is SiO. The noise in the lower part of the of the spectrum (ca. 1500-1000 cm^{-1}) is due to strong absorption of most of the IR beam by the Si crystal.

Figure 6.7a shows the spectra in the CO band region for the first CV to -0.5 V vs RHE. When scanning the potential cathodically, a peak is seen to appear around 2050 cm^{-1} and grow in intensity. Continuing cathodically another sharper peak appears as a shoulder on the initial peak around 2080 cm^{-1} and also grows in intensity. The sharp peak clearly moves with potential as is expected from a surface bound species due to the Stark shift [118, 119]. The peaks will be referred to as the high and low frequency bands or peaks, CO_{HFB} and CO_{LFB}. The two

overlapping peaks have been deconvoluted using two gaussians following a background subtraction. The integrated intensity of each of the gaussians as well as the sum is plotted as a function of time in Figure 6.7(b, c, d) together with the electrochemistry data. The peak centres have also been plotted in the region where the band intensity is high enough to discern them (defined as peak area > 0.15 for CO_{HFB} and >0.3 for CO_{LFB}).
The two peaks can be assigned to various things but it is generally agreed upon that they are due to atop bound CO on Cu. Looking at the Cu single crystal work from Hori's group [68–73], they could simply be CO_{atop} on different Cu facets or steps with the low frequency peak corresponding to terraces and the high frequency peak to steps. Gunathunge et al. attribute the high frequency peak to reversible formation of Cu clusters at higher coverage [79].

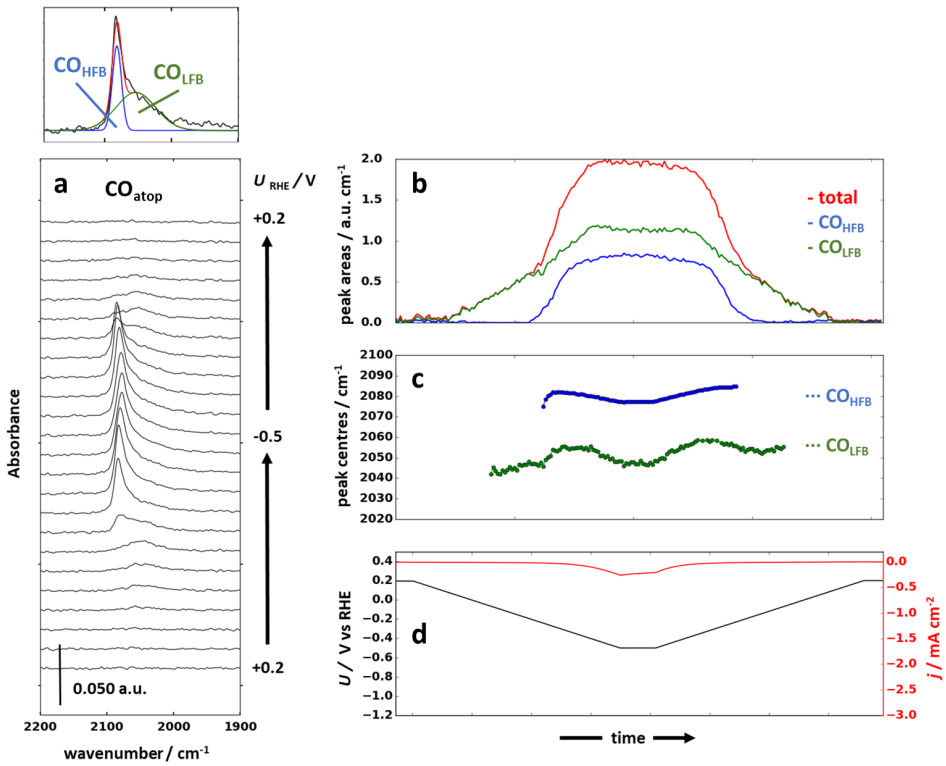

Figure 6.7: SEIRAS spectra corresponding to 2 mV/s CV from +0.2 to -0.5 to +0.2 V vs RHE in CO saturated 0.1 M $KHCO_3$ on Cu. a) Stacked spectra in the CO band region. Every 8th spectrum has been plotted resulting in a 64 mV separation. The deconvolution of the CO peak is illustrated in the upper panel. b) Integrated peak areas for the high frequency and low frequency band and the combined peak area (CO_{HFB}, CO_{LFB}, total). c) Peak centres for CO_{HFB} and CO_{LFB}. d) Corresponding potential and current as a function of time.

To assess the reversibility of the peak intensities and centres, they have been plotted as a function of potential in Figure 6.8. It is clearly observed that the low frequency peak increases almost linearly in area and then plateaus. The CO_{LFB} starts at ca 0.070 V vs RHE (-0.502 V vs SHE) and the CO_{LFB} starts at ca. -0.202 V vs RHE (-0.774 V vs SHE) and has a sharper increase. This is consistent with the data reported by Gunathunge et al. under identical conditions [79, Figure 4c]. In the same study Gunathunge et al. also observed that the general band evolution was preserved but shifted to more negative values vs SHE when lowering the local CO concentration, either by using 0.1 atm CO or 1 atm CO_2 saturated 0.1 M $KHCO_3$, the former giving lower integrated intensities and the latter slightly higher for both peaks. The band evolution thus seems to also depend on the local CO pressure. The more negative onset of the CO_{HFB} band compared to the CO_{LFB}, could be interpreted as that a certain amount of CO_{LFB} must be present before the CO_{HFB} is formed. The CO_{LFB} has reached an area of ca. 0.58 a.u. cm^{-1} when the CO_{HFB} starts to appear. Alternatively, the sites simply have different binding energies.

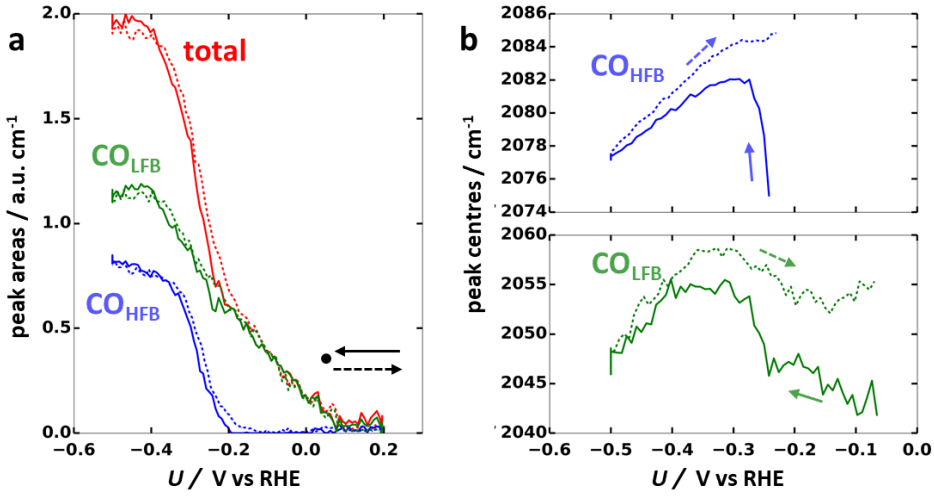

Figure 6.8: Same data as in Figure 6.7 but plotted against potential. a) Peak areas. b) Peak centres. Full and stippled lines indicate the cathodic and anodic scan respectively.

Gunathunge et al. did not report the peak positions of the two peaks. This has been done here with an accuracy of ca. ± 1 cm^{-1}. Particularly, the peak centre of the CO_{LFB} which is wider is harder to define precisely and is seen to be more scattered than the sharper CO_{HFB}.
When the CO_{LFB} peak size has reached 0.3 a.u., so the peak position is well defined, we see that the peak begins around 2043 and slowly increases to 2047 cm^{-1}.

As the CO_{HFB} intensity begins to rise, a sharper incline in the CO_{LFB} position is observed. This is an indication that the two surface populations could be affecting one another. The CO_{LFB} position then decreases as the potential is made more cathodic, probably Stark shift convoluted with other effects. On the anodic scan the behaviour is somewhat reversible with an initial incline in CO_{LFB} position with increased potential and then a decline in position as the intensity of the CO_{HFB} dies off. A tilt towards higher wavenumbers is observed in the position throughout the scan.
The CO_{HFB} has an initial sharp increase in position just as it appears, which could be due to the initial formation of islands of CO (possibly on Cu clusters) where the local environment changes minimally once the islands have passed a certain size. Such CO island formation has been theorised for CO on Cu to explain results from gas phase experiments [33, 64]. As the potential is made more cathodic, a negative shift in position is observed with a quite linear trend which is most likely Stark shift. The reverse Stark shift is observed on the anodic scan, albeit with a slight tilt towards higher wavenumbers as for the CO_{LFB}.

The integrated intensities and peak positions corresponding to all the CV scans highlighted in Figure 6.5 have been included in Appendix A. Generally, a high reproducibility is observed between CVs to the same cathodic potential. Integrated peak areas overlay on the cathodic and anodic branches for -0.5 and -0.7 V but are slightly lower on the returning anodic branch for -0.9 and -1.1 V vs RHE. The intensity decrease is attributed to either i) overall decrease in the intensity during each scan due to small changes in film structure, or ii) slight depletion of the local CO concentration due to the high CO reduction activity at these potentials leading to lower coverage. A drop in maximum total integrated intensity of ca. 50 % is observed from the first to the last experiment (from ca. 2.0 to 1.0 a.u. cm^{-1}) which were performed over more than 5 hours in harsh polarising conditions.
The high total intensity of the CO peak on this sample is noted compared to the work by Gunathunge et al. who reported maximum total peak areas of the CO_{atop} band at 0.73 a.u. cm^{-1}, or a max intensity in the range 10-20$\times10^{-3}$ a.u. [80]. A max intensity of the CO band of 56$\times10^{-3}$ a.u. was obtained here. It was not investigated further whether this was due to an intrinsic improvement of the SEIRA effect on this film or simply an effect of higher surface area.
The peak centres also show good agreement between individual scans with consistent small tilt towards higher wavenumbers on the reverse branch of the scan. A relative lowering in wavenumber is observed in the first part of the return scan for the CO_{LFB} for -0.9 and -1.1 V vs RHE. This is also the case for the CO_{HFB} at -1.1 V vs RHE. The lowering in wavenumber coincides with the lower observed intensities on the return branches of these measurements as stated above. Thus,

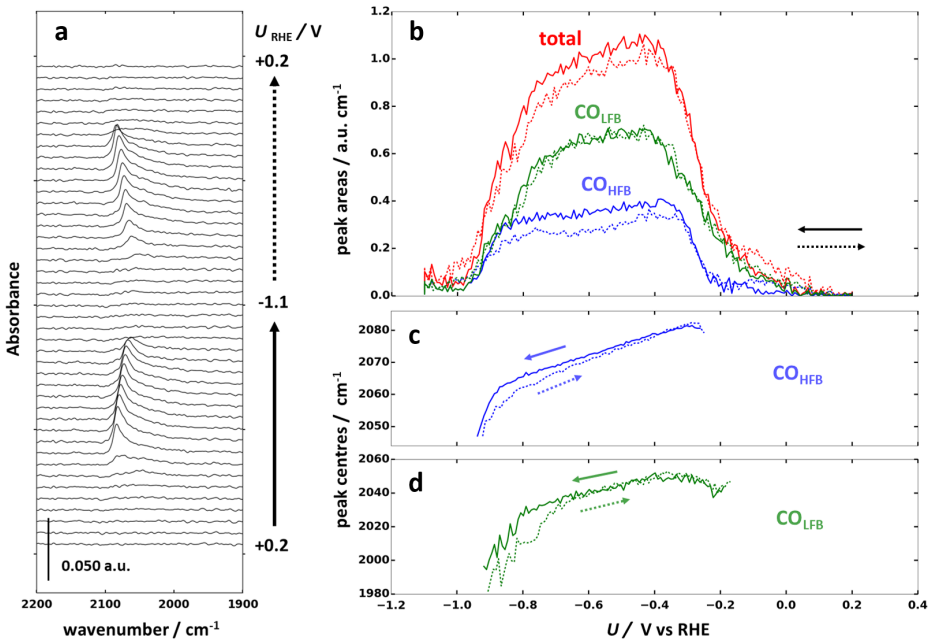

Figure 6.9: SEIRAS spectra and corresponding integrated intensities and peak centres. CO saturated 0.1 M $KHCO_3$ on Cu. 2 mV/s CV from +0.2 to -1.1 V vs RHE and back. a) stacked spectra in the CO stretch region (every 8th spectrum shown). b) Integrated peak intensities of the deconvoluted CO stretch peak. c) Peak centres.

lower coverage could explain both the lower intensity and lower wavenumber observed.

The final scan to -1.1 V vs RHE is shown in Figure 6.9. The full behaviour of of the CO peaks in the widest potential range can be observed, from they appear initially when going cathodic and to they disappear at the most cathodic potentials. The initial stage of the appearance of the bands has already been discussed above. New features that can be observed are that both bands reach a maximum intensity after which a small linear drop in intensity with more cathodic potential is observed. Finally, the intensities experience a sharp drop similar to their initial appearance and eventually disappear completely (small intensity fluctuations around zero are due to noise).
The CO_{HFB} reaches maximum intensity first at ca. -0.37 V and then the CO_{LFB} at ca. -0.43 V vs RHE. The CO_{HFB} then drops linearly in intensity until -0.86 V where the sharp decease occurs. The CO_{LFB} decreases somewhat linearly only until -0.76 V before the sharp decrease. Both peaks are gone at ca. -0.98 V vs RHE.

These points have been tabulated in Table 6.1.
The small linear drop in intensity for both peaks in the plateau between the sharp rise and drop could be interpreted as a small lowering of the CO coverage with more negative potential. However, for UHV studies a maximum in intensity followed by a slight decline has been observed despite increasing coverage [65–67], where saturation coverage is around $\theta = 0.5$ with a small increase to $\theta = 0.57$ upon compression of the adlayer. The final sharp decrease in intensity observed for both peaks seems to indicate a true decrease in CO coverage. This decrease could be due to: i) displacement of CO by adsorbing cations, ii) displacement by adsorbed hydrogen, iii) high CO reduction rates resulting in immediate conversion of CO. Again, the CO_{HFB} population seems dependent on that of the CO_{LFB}, as the CO_{HFB} does not drop sharply before the CO_{LFB} has decreased significantly.

The band positions reflect the behaviour of the band intensities. In the plateau region where the intensities shift mostly linearly, the bands shift in straight lines to lower frequencies with more cathodic potential. This seems to be consistent with a Stark shift due to the increasing electric field across the double layer and/or increased backdonation. It also seems to support that the coverage doesn't change much in this potential region or, alternatively, that the band position is independent of coverage above a certain coverage threshold. As the CO_{LFB} intensity starts to drop sharply, the band position follows after a ca. 25 % decrease from the plateau intensity. The position of the CO_{HFB} seems to drop as soon as the CO_{HFB} intensity starts to decrease.

The stark shifts for the two bands have been estimated using the linear parts of the peak positions in the plateau region (-0.30 to -0.85 V vs RHE for the CO_{HFB} and -0.40 to -0.80 V for the LFB). Only the cathodic branches were used in both cases. Linear regression of the points yields ca. 32 and 52 cm^{-1} V^{-1} for the CO_{HFB} and CO_{LFB}, respectively. The stark shift in similar conditions was reported by Gunathunge et. al to be ca. 30 cm^{-1} V^{-1} (there was no deconvolution of the two bands in this study, so the position of the CO_{HFB} with the highest intensity dominates)[80].

When comparing the obtained results with another study from Gunathunge et al. [80], investigating the effect of using various alkali metal cations on the obtained SEIRAS spectra, we observe both similarities and discrepancies. They observed a much earlier onset of the intensity decrease in the cathodic scan for larger alkali cations (K^+ and Cs^+ bicarbonates) which they attested to stronger interfacial fields caused by these larger ions. For the smaller Li^+ they saw the intensity decrease shifted by more than 200 mV negative. The effect of cation iden-

	U / V vs RHE			
Band	**Initially appears**	**Maximum**	**Decrease initiates**	**Disappears**
CO(HFB)	-0.20	-0.37	-0.86	-0.98
CO(LFB)	-0.07	-0.43	-0.73	-0.98
Total	-0.07	-0.40	-0.76	-0.98

Table 6.1: Estimated potentials for the evolution of the high and low frequency part of the CO stretch band estimated from Figure 6.9. The initial appearance of the bands, their maxima, the initial decrease and their disappearance are tabulated in said order.

tity on the band position was clearly observed as negative shifts with increasing cation size. They also observed substantial irreversibility of the anodic branches for K^+ and Cs^+, with reduction of the maximum by 40 % compared to the cathodic scan. They contributed this to irreversible specific adsorption of the large cations. Interestingly, their data for Li^+ resembles much more closely the data we report here for K^+. This discrepancy could be due to lower mass transport of CO in their experiments and thus local depletion at high CO reduction rates. The study presented here would be improved by the use of different partial pressures of CO as well as varying the cation identity.

The behaviour of the CO stretch band on Cu in CO saturated 0.1 M $KHCO_3$ was investigated with ATR-SEIRAS coupled with electrochemistry. The CO stretch band was deconvoluted into two components; a high frequency and low frequency band (CO_{HFB} and CO_{LFB}). The bands can be attributed to CO on stepped and flat surfaces of the polycrystalline electrode respectively. Alternatively, the CO_{HFB} appears at higher CO coverages due to reversible CO induced formation of Cu clusters. The intensity and position of the two bands was tracked as a function of potential with the most negative potential at -1.1 V vs RHE (ca. -1.67 V vs SHE). The CO_{HFB} appeared dependent on the coverage of the CO_{LFB}. A somewhat linear plateau region was observed in terms of intensity between the initial increase and the final decrease in intensity. A somewhat constant coverage was hypothesised in this region. The band intensities both dropped to zero at ca. -1.0 V vs RHE (ca. -1.6 V vs SHE). This was attributed to either displacement of the CO by other adsorbates (cations, H*) or high CO reduction rates lowering the local CO concentration. A high level of reversibility between the cathodic and anodic scans was also observed, contrary to previously reported work [80]. The band positions also appeared to have positive frequency shifts with initial increase in coverage and complimentary downshifts at decreasing coverage. Additionally, a record-high intensity of 0.056 a.u. was observed for the CO stretch band.
A full understanding of the observed trends is still lacking, but hopefully additional experiments with systematically altered parameters such as CO pressure

and electrolyte identity in combination with theoretical computations will improve that.

6.4 CO on Au

CO on Au thin films was investigated with ATR-SEIRAS. Previous work at SurfCat [146] regarding CO_2 reduction on polycrystalline Au and Au single crystals had revealed that (110) and (211) type sites on polycrystalline Au were the primary site for CO_2 to CO reduction. This was shown by partially blocking the step sites with Pb atoms utilising Pb under potential deposition (UPD). It was therefore hoped that the same phenomenon could be observed with ATR-SEIRAS. Most of the project was performed in collaboration with a bachelor student, Johan Ehlers, whom I was supervising during his Bachelor's project.
Initial experiments focused on production of the Au film where the electroless synthesis method was eventually decided on due to a combination of SEIRAS activity and chemical stability. The second part concerned benchmarking of the CO signal on Au in different electrolytes. Finally, partial blocking of step sites with Pb were performed. The final synthesis procedure is described in Section 3.5.7. The effect of electrolyte and partial blocking of sites with Pb is described in the following.

6.4.1 Effect of varying the electrolyte

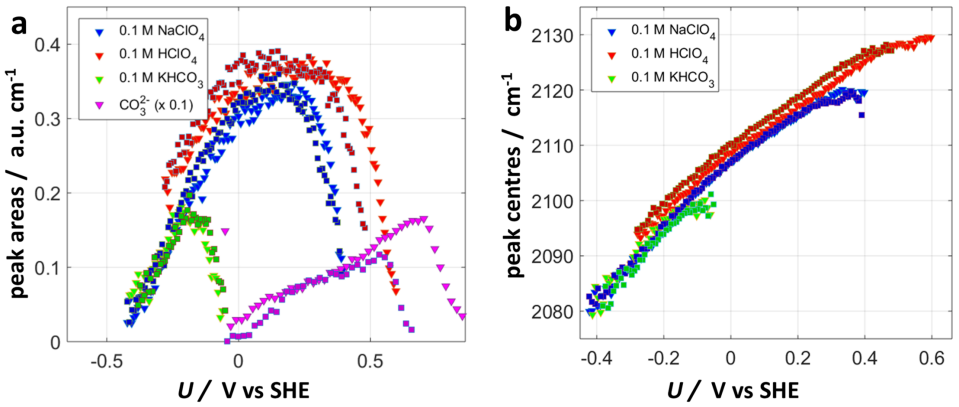

Figure 6.10: ATR-SEIRAS of CO the CO stretch band on Au in CO saturated 0.1 M $NaClO_4$, $HClO_4$ and $KHCO_3$. a) Integrated peak area. b) Peak centre. Cathodic sweep shown as triangles and anodic sweep as squares. The integrated area of the bicarbonate peak has also been included in a). Figure courtesy of Johan Ehlers.

The behaviour of the CO stretch band in different electrolytes was examined. 0.1 M $NaClO_4$, $HClO_4$ and $KHCO_3$ were used in the one-compartment cell with a Au wire counter electrode. When changing the electrolyte the film was gently rinsed several times with milli-Q water before adding the next electrolyte. One

peak is seen for atop bound CO on Au. No other peaks at lower wavenumbers corresponding to CO bound in the bridge position or otherwise were observed at any time. The resulting spectra were fitted yielding the peak area and centre as a function of applied potential in the different electrolytes, as shown in Figure 6.10. For $NaClO_4$ and $HClO_4$ the CO stretch is seen to be visible in a large potential range of approximately 1 full volt, spanning from +0.6 or +0.5 V to -0.4 or -0.5 V vs SHE. The CO stretch band in $KHCO_3$ is, however, observed in a much smaller range, not appearing before ca. 0.05 V vs SHE but disappearing at -0.4 like the the other electrolytes. This is explained by the bicarbonate ion adsorbing on the surface and competing with CO for the sites. The integrated area of the carbonate peak has been co-plotted and is seen to appear as the CO signal disappears. The ClO_4^- ion does not adsorb specifically in the same way [147]. The slightly later onset of the CO peak in $NaClO_4$ vs $HClO_4$ could also be due to small concentrations of bicarbonate. Bicarbonate could be produced at positive potentials where the background is taken as CO is oxidised to CO_2 which in turn can become bicarbonate through reaction with water. This does not occur in the acid as the $CO_2 + H_2O \rightleftharpoons H_2CO_3$ equilibrium is shifted to the left. A somewhat higher intensity is observed for $HClO_4$ than $NaClO_4$. This is possibly due to $HClO_4$ being the electrolyte that the Au film is cycled in to obtain a surface structure with good SEIRAS activity. The signal range for $HClO_4$ is shorter in the cathodic direction as more cathodic potentials caused excessive HER with detrimental effects on the film. The trend in this region is expected to mirror that of the $NaClO_4$.
The band position is observed to be mostly linear with a Stark shift of approximately 50 cm^{-1} V^{-1} which is in accordance with other reports [85]. Small dips are observed initially when the peaks appear on the cathodic scan which could be attributed to a decreasing dipole-dipole interaction at low coverages as observed for Pt and Cu in the previous sections.

Generally, the overall behaviour can be explained by a competition for the surface sites at different surface charges. As CO is bound weakly and reversibly on Au it is an excellent probe molecule for the adsorbability of other electrolyte species. The maximum in the intensity curves for the two perchlorate solutions coincides quite well with the potential of zero charge (PZC) of Au in perchlorate (+0.14 V vs SHE on polycrystalline Au [148], ca. +0.2 to +0.6 V on reconstructed Au single crystals [149]). SEIRAS experiments and models of the water orientation at the interface predict that water, due to being a dipole, is oriented H-down below the PZC, O-down above the PZC, and flat close to the PZC [150](and refs. therein). The weak interaction with dipoles (e.g. water) and ions close to the PZC allows CO to adsorb (if there is a local pressure of CO). Above the PZC, CO

is slowly desorbed as anions adsorb. This occurs faster for the more strongly adsorbing (bi-)carbonate ion compared to perchlorate. It should however also be noted that CO begins to oxidise to CO_2 at around +0.3 V vs SHE. Thus, the signal decrease in the perchlorate solutions going anodic could be due to lower CO coverage at higher CO oxidation rates. Another SEIRAS study estimated perchlorate adsorption to initiate around +0.7 V vs SHE [150]. Below the PZC cations are believed to adsorb and displace CO [89].
Interestingly, in a recent report from Wuttig et al., the desorption of CO when going anodic was attributed to displacement by water and not (bi-)carbonate [88]. If this were the case we would expect a similar behaviour in the perchlorates.

These experiments give powerful insight into the relative behaviour of the different electrolyte species at the interface. The experiment could be improved by expanding the electrolyte selection to systematically ascertain the effect of cation and anion on the CO desorption and hence the relative adsorbability of those ions. The effect of varying the partial CO pressure in these various electrolytes could potentially also prove insightful.

6.4.2 Blocking of step sites on Au with partial Pb UPD

ATR-SEIRAS was performed on Au in 0.1 M $HClO_4$ in the two-compartment cell with a Nafion membrane and a Au mesh counter electrode. $HClO_4$ was chosen specifically to avoid carbonate in the electrolyte either as the main anion constituent (i.e. in $KHCO_3$) or by formation from oxidised CO (i.e. in $NaClO_4$), as Pb precipitates as $PbCO_3$ at neutral conditions. After initial cycling in Ar to structure the surface, CO was introduced and the signal vs potential observed. Then Pb was introduced in the form of 1 mM $Pb(ClO_4)_2$. CVs were performed in the Pb UPD range on Au while the solution was saturated with CO. Finally CO was purged out with Ar and a CV in the Pb UPD range was performed again.

The electrochemical program is shown in Figure 6.11. Figure 6.12(a, b) show the IR spectra in the CO stretch region on Au before and after addition of Pb^{2+} ions. A clear absence of signal is observed for the Pb-containing solution compared to that without Pb. The CO peak spectra were fitted with a single gaussian and the resulting peak areas are plotted against potential in Figure 6.12c. Figure 6.12d shows the corresponding currents. Without Pb, the oxidation of CO is seen anodically and the onset of HER cathodically. With Pb, a clear UPD curve is observed. The slight mismatch and offset from zero in both CVs is attributed to small amounts of oxygen leading to oxygen reduction.

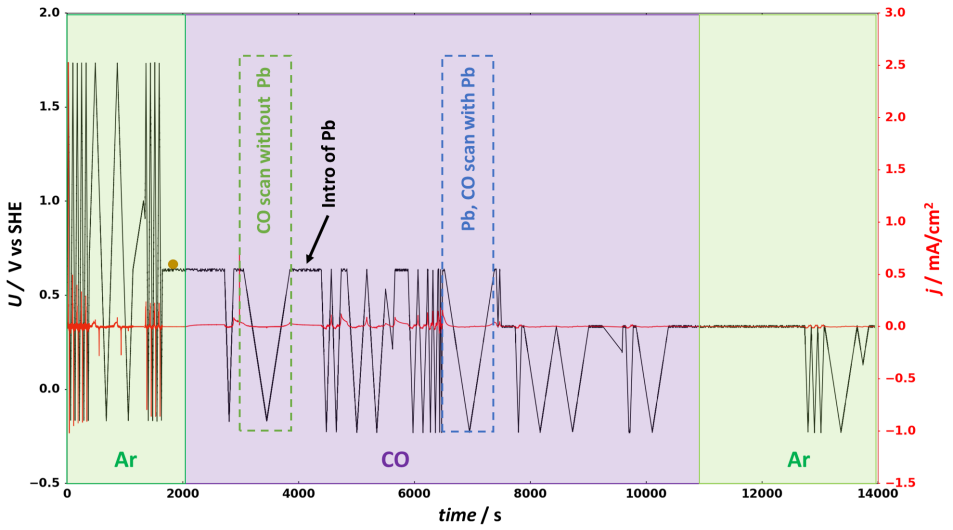

Figure 6.11: Electrochemical program for Pb UPD on Au SEIRAS film experiment. Regions with Ar or CO saturated electrolyte and the introduction of Pb to the solution are indicated. 2 mV/s CVs performed with and without Pb in the electrolyte are in stippled boxes and are referred to later in the text. The yellow dot indicates where the background scan was performed before introduction of CO.

The region corresponding to the drop in intensity has been indicated on the same UPD curve in Figure 6.13. The Pb UPD is in good agreement with the expected features for polycrystalline Au [151]. The broad waves from 0.25 to 0.05 V vs SHE are attributed to a combination of (211) and (110) type sites and the sharp waves around 0.05 V vs SHE to (111) type sites [146]. When going in the cathodic direction, the more open (211) and (110) type sites are seen to be covered by Pb prior to the (111) type sites. When fully blocking only the (211)/(110) type sites with Pb UPD, our group previously observed a 20-fold drop in the CO_2 reduction current on polycrystalline Au [146]. In comparison the HER activity only dropped by a factor of two, attesting to the low site sensitivity for this reaction.
The experiment shown here seems to indicate that the CO stretch signal on polycrystalline Au is also related to these (211)/(110) type sites and not the (111) type sites. This would indicate that the most active catalytic sites for CO_2 reduction on Au are observable through SEIRAS by using CO as a probe molecule. This is despite the fact that actual CO_2 reduction takes place at potentials much more negative than applied here and that the produced CO immediately desorbs at CO_2 reduction potentials.

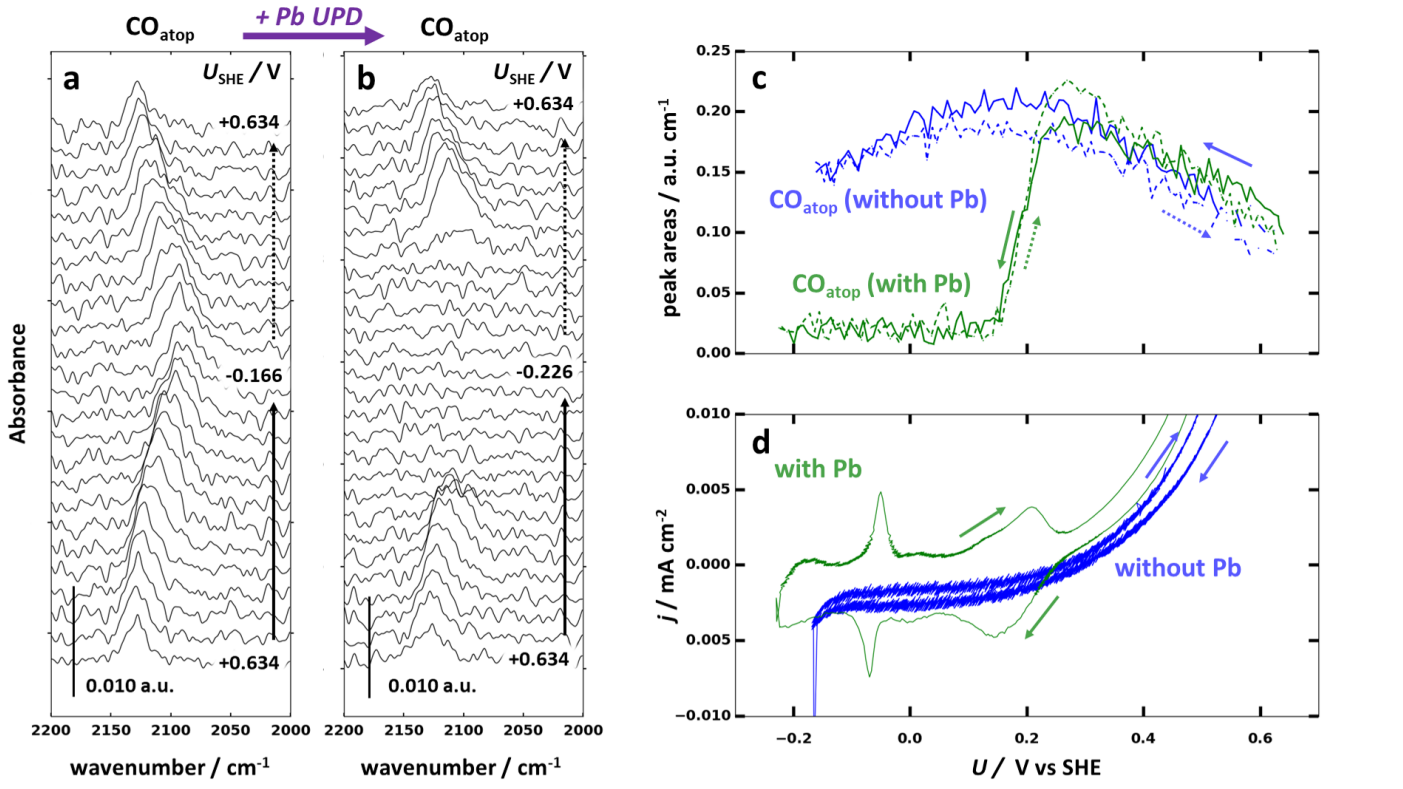

Figure 6.12: ATR-SEIRAS on Au SEIRAS film in the CO stretch region in CO saturated 0.1 M $HClO_4$ before and after addition of Pb. a) IR spectra in the CO stretch region without Pb. b) SEIRAS spectra in the CO stretch region with 1 mM $Pb(ClO_4)_2$. Every 8th spectrum is shown, giving 64 mV separation. c) integrated intensities of the CO stretch with and without Pb as a function of potential. d) Corresponding 2 mV/s CVs with and without Pb.

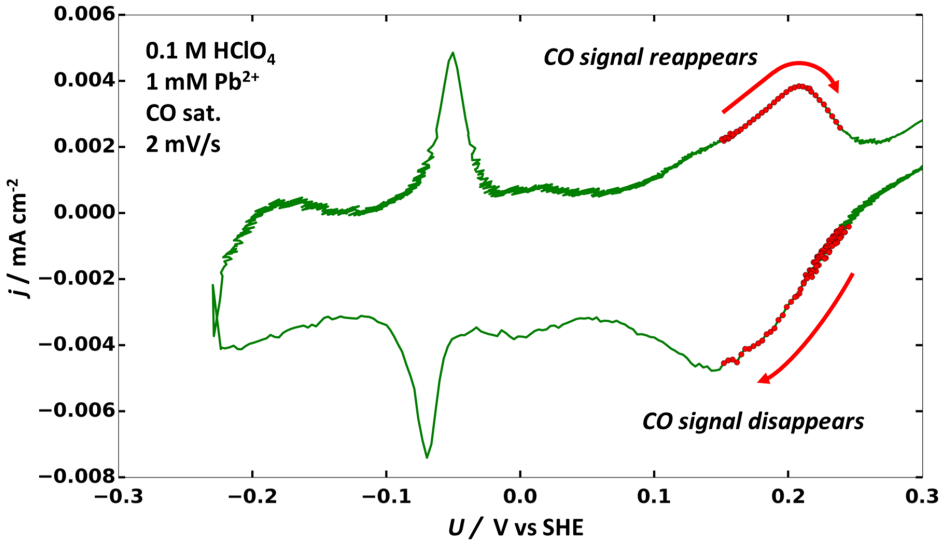

Figure 6.13: CV for Pb on Au SEIRAS film. Same as in Figure 6.12d. 2 mV/s scan rate in CO saturated 0.1 M $HClO_4$ and 1 mM $Pb(ClO_4)_2$. The regions corresponding to the transient in the IR signal for the CO stretch band have been overlaid.

Tracking of a UPD process has been performed previously with SEIRAS for Cu UPD on Au [152]. They applied coadsorbing sulfate as a probe molecule. Performing Cu UPD on Au with CO as the probe molecule could potentially reveal simultaneous but separate bands for CO adsorbed on Au and Cu. The combination of Au and Cu is of interest due to its potential use as a tandem catalyst for CO_2 where Au produces high local concentrations of CO and Cu further reduces the CO.

(Note: Pb UPD experiments in CO saturated electrolyte observed with SEIRAS were also attempted on Cu films. Good SEIRAS activity was however hard to obtain in any other electrolyte than bicarbonate which is incompatible with Pb as mentioned above).

6.5 Comments on experiments not included and possible improvements

6.5.1 Partial UPD in lid-cell

Extensive work was performed trying to realise partial Pb UPD on SEIRAS films by stopping at a potential where only part of the surface sites were covered and then flush the excess Pb from the cell. Flushing out the excess Pb in concentrations around 1 mM from a ca 10 mL volume (two-compartment cell) required excessive amounts of electrolyte as the only means of mixing in the cell was by convection from the incoming and out going electrolyte streams. The one-compartment cell was not ideal despite its smaller electrolyte volume (3-4 mL), due to Pb UPD and auxillary reactions at the counter electrode. Both of these issues were mitigated by the use of a thin layer flow cell with a small electrolyte volume and the counter and reference electrodes mounted on top separated by glass frits, i.e. the lid-cell. The design showed promise and could successfully remove excess Pb from the cell after introduction (data not included). Issues related to bubble formation and resulting loss of potential control need to be mitigated by further design improvements. Many experiments involving fast dynamic exchange of electrolyte components could benefit from this type of design.

6.5.2 Observing bands in the low wavenumber region

All the experiments shown in this thesis are for metal SEIRAS films on Si internal reflection elements. The high absorption of Si in the low wavenumber region does not allow for observation of other bands such as the expected intermediates from CO_2 and CO reduction. Attempts were made to mitigate this by using a combination of a thin Si wafer (0.5 mm) optically coupled to a ZnSe hemisphere as has been reported elsewhere [83, 93–95]. These experiments could successfully observe liquids directly on the Si wafer, but the addition of a metal film attenuated the signal level beyond practical use. Further tests with this configuration focusing on better optical coupling between the ZnSe and Si wafer could prove successful at observing bands in the lower wavenumber region.
An alternative strategy using Si wafers with micromachined facets on the backside [153], effectively making them an internal reflection element, has also shown promise and is now commercially available from the company IRUBIS.

6.6 Conclusion

ATR-SEIRAS was used to observe the CO stretch band on various catalytic surfaces.
For thin Cu overlayers on Pt, the strong interaction between CO and Pt was seen to pull Pt to the surface.
For Pt, a dynamic relationship between the atop and bridge bound CO, and the formation of a COOH intermediate was observed.
On Cu, the CO reduction reaction was tracked by deconvoluting the CO stretch band into two contributing bands and observing their behaviour. Possible origins of the two bands and their interdependence was discussed. Some variation from previously reported work was observed [80]. A record-high intensity of 0.056 a.u. for the CO band was noted.
For Au, CO was seen to function as an infrared probe molecule for the adsorbabilities of the various electrolyte components, and the CO stretch band on the polycrystalline surface was shown to be correlated to (211) and (110) type sites.
Future developments involving thin layer flow cells and the ability to observe the low wavenumber region, and hence bands from further reduced intermediates, were suggested.

Chapter 7

General Conclusions

In this chapter the results from chapters 4, 5 and 6 will be summed up and tied together.

Chapter 4 showed that polycrystalline Cu has a high intrinsic activity for CO reduction comparable to nanostructured equivalents when normalised to the ECSA, despite large variations in geometric current density. Variations in product selectivity were attributed to different available potential windows for the different levels of structuring of the catalysts (determining when mass transport sets in), as well as readsorption in porous structures and more undercoordinated sites.

Chapter 5 investigated the presence of oxidised phases at the surface layers of polycrystalline Cu during CO reduction conditions and found that they were reduced at potentials positive of the CO reduction. This is a valuable result in the discussion of subsurface oxygen in the CO_2 reduction field. Indications of restructuring in favour of (100) type surfaces were also observed in line with other reports and may help to explain the selectivity of polycrystalline Cu for ethene.

Chapter 6 illustrated how the ATR-SEIRAS technique can be used to track surface bond intermediates during the CO and CO_2 reduction reactions. CO reduction on Cu was investigated by deconvolution of the CO_{atop} band into two contributions and tracking of their intensity and position as a function of potential. Variations from prior reports on a similar system were observed, highlighting a need for more well defined reaction conditions and additional measurements.
CO was seen to function as a probe molecule on Au, due to its low adsorption strength, its displacement indicating the preferential adsorption of other electrolyte species.

By observing the CO band on Au while performing Pb UPD it was shown that the CO band on Au is related to the (211) and (110) type sites.

In this thesis, electrochemistry has been combined with in situ measurements on different time scales. Product detection required prolonged fixed potentials to avoid convolution of products from different potentials, whereas the surface sensitive in situ spectroscopic techniques could track surface structure and adsorbate coverage whilst changing the potential. All these techniques worked together to give a more complete view of the electrochemical CO_2 and CO reduction reactions. A future combination of the ability to observe surface adsorbates with dynamic changing of reaction environment and rapid continuous product detection would result in a strong investigational tool for study of reactions at the electrode-electrolyte interface. We need such tools to improve our understanding of electrocatalysis, a piece of the puzzle for a renewable energy society.

Bibliography

[1] B. Obama. The irreversible momentum of clean energy: Private-sector efforts help drive decoupling of emissions and economic growth. *Science*, 355(6321):126–129, 2017.

[2] World Bank Group. IEA Statistics. GDP per unit of energy use. https://data.worldbank.org/indicator/EG.GDP.PUSE.KO.PP?contextual=default&locations=US-CN-EU-1W.

[3] C. Le Quéré, R. M. Andrew, P. Friedlingstein, S. Sitch, J. Hauck, J. Pongratz, P. A. Pickers, J. I. Korsbakken, G. P. Peters, J. G. Canadell, A. Arneth, and et al. Global Carbon Budget 2018. *Earth System Science Data*, 10(4):2141–2194, 2018.

[4] V. Mason-Delmotte, P. Zha, H.-O. Pörtner, D. Roberts, J. Skea, P. R. Shukla, A. Pirani, W. Moufouma-Okia, C. Pean, R. Pidcock, and et al. Global warming of 1.5°C. An IPCC Special Report on the impacts of global warming of 1.5°C above pre-industrial levels and related global greenhouse gas emission pathways, in the context of strengthening the global response to the threat of climate change, sustainable development, and efforts to eradicate poverty. Technical report, IPCC, 2018.

[5] K. B. Tokarska, N. P. Gillett, A. J. Weaver, V. K. Arora, and M. Eby. The climate response to five trillion tonnes of carbon. *Nature Climate Change*, 6 (9):851–855, 2016.

[6] S. J. Davis, N. S. Lewis, M. Shaner, S. Aggarwal, D. Arent, I. L. Azevedo, S. M. Benson, T. Bradley, J. Brouwer, Y. M. Chiang, C. T. Clack, A. Cohen, S. Doig, J. Edmonds, P. Fennell, C. B. Field, B. Hannegan, B. M. Hodge, M. I. Hoffert, E. Ingersoll, P. Jaramillo, K. S. Lackner, K. J. Mach, M. Mastrandrea, J. Ogden, P. F. Peterson, D. L. Sanchez, D. Sperling, J. Stagner, J. E. Trancik, C. J. Yang, and K. Caldeira. Net-zero emissions energy systems. *Science*, 360 (6396):eaas9793, 2018.

[7] E. S. Sanz-Pérez, C. R. Murdock, S. A. Didas, and C. W. Jones. Direct Capture of CO_2 from Ambient Air. *Chemical Reviews*, 116(19):11840–11876, 2016.

[8] D. H. Apaydin, M. Gora, E. Portenkirchner, K. T. Oppelt, H. Neugebauer, M. Jakesova, E. D. Głowacki, J. Kunze-Liebhäuser, M. Zagorska, J. Mieczkowski, and N. S. Sariciftci. Electrochemical Capture and Release of CO_2 in Aqueous Electrolytes Using an Organic Semiconductor Electrode. *Acs Applied Materials and Interfaces*, 9(15):12919–12923, 2017.

[9] H. De Coninck and S. M. Benson. Carbon dioxide capture and storage: Issues and prospects. *Annual Review of Environment and Resources*, 39(1): 243–270, 2014.

[10] J. P. Chamberlain, R. Hammerschlag, and C. P. Schaber. Energy storage technologies. *Energy Conversion, Second Edition*, pages 497–523, 2017.

[11] Z. Yang, J. Zhang, M. C. Kintner-Meyer, X. Lu, D. Choi, J. P. Lemmon, and J. Liu. Electrochemical energy storage for green grid. *Chemical Reviews*, 111 (5):3577–3613, 2011.

[12] *Whitebook, Energy storage technologies in a Danish and international perspective*. Technical University of Denmark, Department of Energy Conversion and StorageTechnical University of Denmark, Department of Energy Conversion and Storage, 2019.

[13] Z. W. Seh, J. Kibsgaard, C. F. Dickens, I. Chorkendorff, J. K. Nørskov, and T. F. Jaramillo. Combining theory and experiment in electrocatalysis: Insights into materials design. *Science*, 355(6321):eaad4998, 2017.

[14] P. De Luna, C. Hahn, D. Higgins, S. A. Jaffer, T. F. Jaramillo, and E. H. Sargent. What would it take for renewably powered electrosynthesis to displace petrochemical processes? *Science*, 364(6438):eaav3506, 2019.

[15] The International Renewable Energy Agency (IRENA). Renewable Power Generation Costs in 2018, 2019.

[16] P. E. Brockway, A. Owen, L. I. Brand-Correa, and L. Hardt. Estimation of global final-stage energy-return-on-investment for fossil fuels with comparison to renewable energy sources. *Nature Energy*, 4(7):612–621, 2019.

[17] Y. Hori. Electrochemical CO_2 Reduction on Metal Electrodes. *Modern Aspects of Electrochemistry*, (42):89–189, 2008.

[18] K. P. Kuhl, E. R. Cave, D. N. Abram, and T. F. Jaramillo. New insights into the electrochemical reduction of carbon dioxide on metallic copper surfaces. *Energy & Environmental Science*, 5:7050, 2012.

[19] S. A. Nitopi, E. Bertheussen, S. B. Scott, X. Liu, A. K. Engstfeld, S. Horch, B. Seger, I. Stephens, K. Chan, C. Hahn, J. K. Nørskov, T. Jaramillo, and I. Chorkendorff. Progress and Perspectives of Electrochemical CO_2 Reduction on Copper in Aqueous Electrolyte. *Chemical Reviews*, 119(12):7610–7672, 2019.

[20] Y. Hori, H. Wakebe, T. Tsukamoto, and O. Koga. Electrocatalytic process of CO selectivity in electrochemical reduction of CO_2 at metal electrodes in aqueous media. *Electrochimica Acta*, 39(11-12):1833–1839, aug 1994.

[21] Y. Hori, K. Kikuchi, and S. Suzuki. Production of CO and CH_4 in electrochemical reduction of CO_2 at metal electrodes in aqueous hydrogencarbonate solution. *Chemistry Letters*, 14(11):1695–1698, 1985.

[22] A. Bagger, W. Ju, A. S. Varela, P. Strasser, and J. Rossmeisl. Electrochemical CO_2 Reduction: A Classification Problem. *Chemphyschem*, 18(22):3266–3273, 2017.

[23] J. K. Nørskov, T. Bligaard, A. Logadottir, J. Kitchin, J. Chen, S. Pandelov, and U. Stimming. Trends in the exchange current for hydrogen evolution. *Journal of the Electrochemical Society*, 152(2):J23–J26, 2005.

[24] M. T. Koper. Thermodynamic theory of multi-electron transfer reactions: Implications for electrocatalysis. *Journal of Electroanalytical Chemistry*, 660(2): 254–260, 2011.

[25] F. Abild-Pedersen, J. P. Greeley, F. Studt, J. Rossmeisl, T. R. Fronczek-Munter, P. G. Moses, E. Skulason, T. Bligaard, and J. K. Nørskov. Scaling properties of adsorption energies for hydrogen-containing molecules on transition-metal surfaces. *Physical Review Letters*, 99(1):016105, 2007.

[26] A. A. Peterson, F. Abild-Pedersen, F. Studt, J. Rossmeisl, and J. K. Nørskov. How copper catalyzes the electroreduction of carbon dioxide into hydrocarbon fuels. *Energy & Environmental Science*, 3(9):1311–1315, 2010.

[27] A. A. Peterson and J. K. Nørskov. Activity Descriptors for CO_2 Electroreduction to Methane on Transition-Metal Catalysts. *The Journal of Physical Chemistry Letters*, 3(2):251–258, jan 2012.

[28] Y. Hori, I. Takahashi, O. Koga, and N. Hoshi. Electrochemical reduction of carbon dioxide at various series of copper single crystal electrodes. *Journal of Molecular Catalysis A: Chemical*, 199(1-2):39–47, may 2003.

[29] Y. Huang, A. D. Handoko, P. Hirunsit, and B. S. Yeo. Electrochemical Reduction of CO_2 Using Copper Single-Crystal Surfaces: Effects of CO* Coverage on the Selective Formation of Ethylene. *Acs Catalysis*, 7(3):1749–1756, 2017.

[30] Y. G. Kim, J. H. Baricuatro, A. Javier, J. M. Gregoire, and M. P. Soriaga. The evolution of the polycrystalline copper surface, first to Cu(111) and then to Cu(100), at a fixed CO_2RR potential: A study by operando EC-STM. *Langmuir*, 30(50):15053–15056, 2014.

[31] Y. G. Kim, J. H. Baricuatro, and M. P. Soriaga. Surface Reconstruction of Polycrystalline Cu Electrodes in Aqueous $KHCO_3$ Electrolyte at Potentials in the Early Stages of CO_2 Reduction. *Electrocatalysis*, 9(4):526–530, 2018.

[32] Y. G. Kim, A. Javier, J. H. Baricuatro, D. Torelli, K. D. Cummins, C. F. Tsang, J. C. Hemminger, and M. P. Soriaga. Surface reconstruction of pure-Cu single-crystal electrodes under CO-reduction potentials in alkaline solutions: A study by seriatim ECSTM-DEMS. *Journal of Electroanalytical Chemistry*, 780:290–295, 2016.

[33] B. Eren, D. Zherebetskyy, L. L. Patera, C. H. Wu, H. Bluhm, C. Africh, L. W. Wang, G. A. Somorjai, and M. Salmeron. Activation of Cu(111) surface by decomposition into nanoclusters driven by CO adsorption. *Science*, 351 (6272):475–478, 2016.

[34] Y. Hori, A. Murata, R. Takahashi, and S. Suzuki. Electroreduction of CO to C_2H_4 and C_2H_4 at a copper electrode in aqueous-solutions at ambient-temperature and pressure. *Journal of the American Chemical Society*, 109(16): 5022–5023, 1987.

[35] Y. Hori, A. Murata, and R. Takahashi. Formation of hydrocarbons in the electrochemical reduction of carbon dioxide at a copper electrode in aqueous solution. *Journal of the Chemical Society, Faraday Transactions 1: Physical Chemistry in Condensed Phases*, 85(8):2309, 1989.

[36] Y. Hori, R. Takahashi, Y. Yoshinami, and A. Murata. Electrochemical reduction of CO at a copper electrode. *Journal of Physical Chemistry B*, 101(36): 7075–7081, 1997.

[37] Y. Hori, A. Murata, R. Takahashi, and S. Suzuki. Electrochemical Reduction of Carbon Monoxide to Hydrocarbons at Various Metal Electrodes in Aqueous Solution. *Chemistry Letters*, 16(8):1665–1668, 1987.

[38] L. Wang, S. A. Nitopi, E. Bertheussen, M. Orazov, C. G. Morales-Guio, X. Liu, D. C. Higgins, K. Chan, J. K. Nørskov, C. Hahn, and T. F. Jaramillo. Electrochemical Carbon Monoxide Reduction on Polycrystalline Copper: Effects of Potential, Pressure, and pH on Selectivity toward Multicarbon and Oxygenated Products. *ACS Catalysis*, 8(8):7445–7454, 2018.

[39] C. W. Li, J. Ciston, and M. W. Kanan. Electroreduction of carbon monoxide to liquid fuel on oxide-derived nanocrystalline copper. *Nature*, 508(7497): 504–507, 2014.

[40] C. G. Morales-Guio, E. R. Cave, S. A. Nitopi, J. T. Feaster, L. Wang, K. P. Kuhl, A. Jackson, N. C. Johnson, D. N. Abram, T. Hatsukade, C. Hahn, and T. F. Jaramillo. Improved CO_2 reduction activity towards C2+ alcohols on a tandem gold on copper electrocatalyst. *Nature Catalysis*, 1(10):764–771, 2018.

[41] J. Huang, M. Mensi, E. Oveisi, V. Mantella, and R. Buonsanti. Structural Sensitivities in Bimetallic Catalysts for Electrochemical CO_2 Reduction Revealed by Ag-Cu Nanodimers. *Journal of the American Chemical Society*, 141(6):2490–2499, 2019.

[42] F. Calle-Vallejo and M. T. M. Koper. Theoretical Considerations on the Electroreduction of CO to C2 Species on Cu(100) Electrodes. *Angewandte Chemie*, 125(28):7423–7426, 2013.

[43] J. H. Montoya, C. Shi, K. Chan, and J. K. Nørskov. Theoretical insights into a CO dimerization mechanism in CO_2 electroreduction. *Journal of Physical Chemistry Letters*, 6(11):2032–2037, 2015.

[44] N. Gupta, M. Gattrell, and B. MacDougall. Calculation for the cathode surface concentrations in the electrochemical reduction of CO_2 in $KHCO_3$ solutions. *Journal of Applied Electrochemistry*, 36(2):161–172, oct 2005.

[45] W. Tang, A. A. Peterson, A. S. Varela Gasque, Z. Jovanov, L. Bech, W. J. Durand, S. Dahl, J. K. Nørskov, and I. Chorkendorff. The importance of surface morphology in controlling the selectivity of polycrystalline copper for CO_2 electroreduction. *Physical Chemistry Chemical Physics*, 14(1):76–81, 2012.

[46] H. Mistry, A. S. Varela, C. S. Bonifacio, I. Zegkinoglou, I. Sinev, Y. W. Choi, K. Kisslinger, E. A. Stach, J. C. Yang, P. Strasser, and B. R. Cuenya. Highly

selective plasma-activated copper catalysts for carbon dioxide reduction to ethylene. *Nature Communications*, 7(1):12123, 2016.

[47] D. Kim, S. Lee, J. D. Ocon, B. Jeong, J. K. Lee, and J. Lee. Insights into an autonomously formed oxygen-evacuated Cu_2O electrode for the selective production of C_2H_4 from CO_2. *Physical Chemistry Chemical Physics*, 17(2): 824–830, 2015.

[48] D. Ren, Y. Deng, A. D. Handoko, C. S. Chen, S. Malkhandi, and B. S. Yeo. Selective Electrochemical Reduction of Carbon Dioxide to Ethylene and Ethanol on Copper(I) oxide catalysts. *ACS Catalysis*, 5(5):2814–2821, 2015.

[49] C. W. Li, J. Ciston, and M. W. Kanan. Electroreduction of carbon monoxide to liquid fuel on oxide-derived nanocrystalline copper. *Nature*, 508(7497): 504–507, 2014.

[50] Y. Chen, C. W. Li, and M. W. Kanan. Aqueous CO_2 reduction at very low overpotential on oxide-derived Au nanoparticles. *Journal of the American Chemical Society*, 134(49):19969–19972, 2012.

[51] X. Feng, K. Jiang, S. Fan, and M. W. Kanan. A direct grain-boundary-activity correlation for CO electroreduction on Cu nanoparticles. *Acs Central Science*, 2(3):169–174, 2016.

[52] A. Verdaguer Casadevall, C. W. Li, T. P. Johansson, S. B. Scott, J. T. McKeown, M. Kumar, I. E. L. Stephens, M. W. Kanan, and I. Chorkendorff. Probing the Active Surface Sites for CO Reduction on Oxide-Derived Copper Electrocatalysts. *Journal of the American Chemical Society*, 137(31):9808–9811, 2015.

[53] P. J. Mallard and W. G. Linstrom. *NIST Chemistry WebBook, NIST Standard Reference Database Number 69*. National Institute of Standards and Technology, Gaithersburg MD, 20899.

[54] J. A. Dean. *Lange's handbook of chemistry*. McGraw-Hill,, 1999.

[55] A. Eilert, F. Cavalca, F. S. Roberts, J. Osterwalder, C. Liu, M. Favaro, E. J. Crumlin, H. Ogasawara, D. Friebel, L. G. Pettersson, and A. Nilsson. Subsurface Oxygen in Oxide-Derived Copper Electrocatalysts for Carbon Dioxide Reduction. *Journal of Physical Chemistry Letters*, 8(1):285–290, 2017.

[56] M. Favaro, H. Xiao, T. Cheng, W. A. Goddard, J. Yano, and E. J. Crumlin. Subsurface oxide plays a critical role in CO_2 activation by Cu(111) surfaces to form chemisorbed CO_2, the first step in reduction of CO_2. *Proceedings of the National Academy of Sciences*, 114(26):6706–6711, 2017.

[57] C. Liu, M. P. Lourenço, S. Hedström, F. Cavalca, O. Diaz-Morales, H. A. Duarte, A. Nilsson, and L. G. Pettersson. Stability and effects of subsurface oxygen in oxide-derived Cu catalyst for CO_2 reduction. *Journal of Physical Chemistry C*, 121(39):25010–25017, 2017.

[58] Y. Lum and J. W. Ager. Stability of Residual Oxides in Oxide-Derived Copper Catalysts for Electrochemical CO_2 Reduction Investigated with ^{18}O Labeling. *Angewandte Chemie - International Edition*, 57(2):551–554, 2018.

[59] L. Mandal, K. R. Yang, M. R. Motapothula, D. Ren, P. Lobaccaro, A. Patra, M. Sherburne, V. S. Batista, B. S. Yeo, J. W. Ager, J. Martin, and T. Venkatesan. Investigating the Role of Copper Oxide in Electrochemical CO_2 Reduction in Real Time. *ACS Applied Materials & Interfaces*, 10(10):8574–8584, 2018. PMID: 29437377.

[60] A. J. Garza, A. T. Bell, and M. Head-Gordon. Is Subsurface Oxygen Necessary for the Electrochemical Reduction of CO_2 on Copper? *Journal of Physical Chemistry Letters*, 9(3):601–606, 2018.

[61] C. T. Dinh, T. Burdyny, G. Kibria, A. Seifitokaldani, C. M. Gabardo, F. Pelayo García De Arquer, A. Kiani, J. P. Edwards, P. De Luna, O. S. Bushuyev, C. Zou, R. Quintero-Bermudez, Y. Pang, D. Sinton, and E. H. Sargent. CO_2 electroreduction to ethylene via hydroxide-mediated copper catalysis at an abrupt interface. *Science*, 360(6390):783–787, 2018.

[62] D. Higgins, C. Hahn, C. Xiang, T. F. Jaramillo, and A. Z. Weber. Gas-Diffusion Electrodes for Carbon Dioxide Reduction: A New Paradigm. *ACS Energy Letters*, 4(1):317–324, 2019.

[63] D. M. Weekes, D. A. Salvatore, A. Reyes, A. Huang, and C. P. Berlinguette. Electrolytic CO_2 Reduction in a Flow Cell. *Accounts of Chemical Research*, 51 (4):910–918, 2018.

[64] P. Hollins and J. Pritchard. *Reflection Absorption Infrared Spectroscopy: Application to Carbon Monoxide on Copper*, pages 125–143. Springer Berlin Heidelberg, Berlin, Heidelberg, 1980.

[65] R. Ryberg. Carbon-monoxide adsorbed on Cu(100) studied by infrared spectroscopy. *Surface Science*, 114(2-3):627–641, 1982.

[66] K. Horn and J. Pritchard. Infrared-spectrum of CO chemisorbed on Cu(100). *Surface Science*, 55(2):701–704, 1976.

[67] J. Pritchard, T. Catterick, and R. K. Gupta. Infrared spectroscopy of chemisorbed carbon monoxide on copper. *Surface Science*, 53(1):1–20, 1–20, 1975.

[68] Y. Hori, A. Murata, T. Tsukamoto, H. Wakebe, O. Koga, and H. Yamazaki. Adsoprtion of carbon monoxide at a copper electrode accompanied by electron transfer observed by voltammetry and IR spectroscopy. *Electrochimica Acta*, 39(17):2495–2500, dec 1994.

[69] Y. Hori, O. Koga, H. Yamazaki, and T. Matsuo. Infrared-spectroscopy of adsorbed CO and intermediate species in electrochemical reduction of CO_2 to hydrocarbons on a Cu electrode. *Electrochimica Acta*, 40(16):2617–2622, 1995.

[70] O. Koga, T. Matsuo, H. Yamazaki, and Y. Hori. Infrared spectroscopic study of CO_2 and CO reduction at metal electrodes. *Studies in Surface Science and Catalysis*, 114:569–572, 1998.

[71] Y. Hori, O. Koga, Y. Watanabe, and T. Matsuo. FTIR measurements of charge displacement adsorption of CO on poly- and single crystal (100) of Cu electrodes. *Electrochimica Acta*, 44(8-9):1389–1395, 1998.

[72] O. Koga, Y. Watanabe, M. Tanizaki, and Y. Hori. Specific adsorption of anions on a copper (100) single crystal electrode studied by charge displacement by CO adsorption and infrared spectroscopy. *Electrochimica Acta*, 46(20):3083 – 3090, 2001.

[73] O. Koga, S. Teruya, K. Matsuda, M. Minami, N. Hoshi, and Y. Hori. Infrared spectroscopic and voltammetric study of adsorbed CO on stepped surfaces of copper monocrystalline electrodes. *Electrochimica Acta*, 50(12):2475–2485, 2005.

[74] M. Osawa. Surface-Enhanced Infrared Absorption Spectroscopy. *Compendium of Surface and Interface Analysis*, pages 697–706, 2018.

[75] H. Miyake and M. Osawa. Surface-enhanced infrared spectrum of CO adsorbed on Cu electrodes in solution. *Chemistry Letters*, 33(3):278–279, 2004.

[76] H.-F. Wang, Y.-G. Yan, S.-J. Huo, W.-B. Cai, Q.-J. Xu, and M. Osawa. Seeded growth fabrication of Cu-on-Si electrodes for in situ ATR-SEIRAS applications. *Electrochimica Acta*, 52:5950–5957, 2007.

[77] J. Heyes, M. Dunwell, and B. Xu. CO_2 Reduction on Cu at Low Overpotentials with Surface-Enhanced in Situ Spectroscopy. *Journal of Physical Chemistry C*, 120(31):17334–17341, 2016.

[78] A. Wuttig, C. Liu, Q. Peng, M. Yaguchi, C. H. Hendon, K. Motobayashi, S. Ye, M. Osawa, and Y. Surendranath. Tracking a Common Surface-Bound Intermediate during CO_2-to-Fuels Catalysis. *ACS Central Science*, 2(8):522–528, 2016.

[79] C. M. Gunathunge, X. Li, J. Li, R. P. Hicks, V. J. Ovalle, and M. M. Waegele. Spectroscopic Observation of Reversible Surface Reconstruction of Copper Electrodes under CO_2 Reduction. *Journal of Physical Chemistry C*, 121(22): 12337–12344, 2017.

[80] C. M. Gunathunge, V. J. Ovalle, and M. M. Waegele. Probing promoting effects of alkali cations on the reduction of CO at the aqueous electrolyte/copper interface. *Physical Chemistry Chemical Physics*, 19(44):30166–30172, 2017.

[81] C. M. Gunathunge, V. J. Ovalle, Y. Li, M. J. Janik, and M. M. Waegele. Existence of an Electrochemically Inert CO Population on Cu Electrodes in Alkaline pH. *ACS Catalysis*, 8(8):7507–7516, 2018.

[82] E. Pérez-Gallent, M. C. Figueiredo, F. Calle-Vallejo, and M. T. M. Koper. Spectroscopic Observation of a Hydrogenated CO Dimer Intermediate During CO Reduction on Cu(100) Electrodes. *Angewandte Chemie - International Edition*, 56(13):3621–3624, 2017.

[83] Y. Katayama, F. Nattino, L. Giordano, J. Hwang, R. R. Rao, O. Andreussi, N. Marzari, and Y. Shao-Horn. An In Situ Surface-Enhanced Infrared Absorption Spectroscopy Study of Electrochemical CO_2 Reduction: Selectivity Dependence on Surface C-Bound and O-Bound Reaction Intermediates. *The Journal of Physical Chemistry C*, 123(10):5951–5963, 2019.

[84] Y. Jugnet, F. J. Cadete Santos Aires, C. Deranlot, L. Piccolo, and J. C. Bertolini. CO chemisorption on Au(110) investigated under elevated pressures by polarized reflection absorption infrared spectroscopy and scanning tunneling microscopy. *Surface Science*, 521(1-2):L639–L644, L639–L644, 2002.

[85] S. G. Sun, W. B. Cai, L. J. Wan, and M. Osawa. Infrared absorption enhancement for CO adsorbed on Au films in perchloric acid solutions and effects of surface structure studied by cyclic voltammetry, scanning tunneling microscopy, and surface-enhanced IR spectroscopy. *Journal of Physical Chemistry B*, 103(13):2460–2466, 1999.

[86] H. Miyake, S. Ye, and M. Osawa. Electroless deposition of gold thin films on silicon for surface-enhanced infrared spectroelectrochemistry. *Electrochemistry Communications*, 4(12):973–977, 2002.

[87] A. Wuttig, M. Yaguchi, K. Motobayashi, M. Osawa, and Y. Surendranath. Inhibited proton transfer enhances Au-catalyzed CO_2-to-fuels selectivity. *Proceedings of the National Academy of Sciences of the United States of America*, 113(32):E4585–E4593, 2016.

[88] A. Wuttig, J. Ryu, and Y. Surendranath. Electrolyte Competition Controls Surface Binding of CO Intermediates to CO_2 Reduction Catalysts. *ChemRxiv*, 2019.

[89] M. Dunwell, Q. Lu, Q. Lu, J. M. Heyes, J. Rosen, J. G. Chen, Y. Yan, F. Jiao, and B. Xu. The Central Role of Bicarbonate in the Electrochemical Reduction of Carbon Dioxide on Gold. *Journal of the American Chemical Society*, 139(10): 3774–3783, 2017.

[90] M. Dunwell, X. Yang, B. P. Setzler, J. Anibal, Y. Yan, and B. Xu. Examination of Near-Electrode Concentration Gradients and Kinetic Impacts on the Electrochemical Reduction of CO_2 using Surface-Enhanced Infrared Spectroscopy. *ACS Catalysis*, 8(5):3999–4008, 2018.

[91] M. Dunwell, X. Yang, Y. Yan, and B. Xu. Potential Routes and Mitigation Strategies for Contamination in Interfacial Specific Infrared Spectroelectrochemical Studies. *Journal of Physical Chemistry C*, 122(43):24658–24664, 2018.

[92] O. Ayemoba and A. Cuesta. Spectroscopic Evidence of Size-Dependent Buffering of Interfacial pH by Cation Hydrolysis during CO_2 Electroreduction. *ACS Applied Materials and Interfaces*, 9(33):27377–27382, 2017.

[93] M. H. Shao, P. Liu, and R. R. Adzic. Superoxide anion is the intermediate in the oxygen reduction reaction on platinum electrodes. *Journal of the American Chemical Society*, 128(23):7408–7409, 2006.

[94] X. K. Xue, J. Y. Wang, Q. X. Li, Y. G. Yan, J. H. Liu, and W. B. Cai. Practically modified attenuated total reflection surface-enhanced IR absorption spectroscopy for high-quality frequency-extended detection of surface species at electrodes. *Analytical Chemistry*, 80(1):166–171, 2008.

[95] F. Shi, P. N. Ross, G. A. Somorjai, and K. Komvopoulos. The Chemistry of Electrolyte Reduction on Silicon Electrodes Revealed by in Situ ATR-FTIR Spectroscopy. *Journal of Physical Chemistry C*, 121(27):14476–14483, 2017.

[96] A. J. Bard, L. Faulkner, C. G. Zoski, and J. Leddy. *Electrochemical methods: fundamentals and applications*. John Wiley, 2001.

[97] E. Bertheussen. *Electroreduction of carbon monoxide on copper electrodes*. Phd, Department of Physics, Technical University of Denmark, 2018.

[98] E. Bertheussen, Y. Abghoui, Z. P. Jovanov, A.-S. Varela, I. E. Stephens, and I. Chorkendorff. Quantification of liquid products from the electroreduction of CO_2 and CO using static headspace-gas chromatography and nuclear magnetic resonance spectroscopy. *Catalysis Today*, 288:54–62, 2017.

[99] Z. Jovanov. Towards synthetic fuels via electrocatalysis, 2014.

[100] J. I. Goldstein, D. E. Newbury, J. R. Michael, N. W. Ritchie, J. H. J. Scott, and D. C. Joy. *Scanning electron microscopy and X-ray microanalysis*. Springer New York, 2017.

[101] I. Chorkendorff and J. Niemantsverdriet. *Concepts of modern catalysis and kinetics*. Wiley-VCH,, 2007.

[102] J. Als-Nielsen and D. McMorrow. *Elements of Modern X-ray Physics: Second Edition*. John Wiley and Sons, 2011.

[103] B. L. Henke, E. M. Gullikson, and J. C. Davis. X-ray interactions - photoabsorption, scattering, transmission, and reflection at E=50-30,000 eV, Z=1-92. *Atomic Data and Nuclear Data Tables*, 54(2):181–342, 1993.

[104] M. Farmand, A. T. Landers, J. C. Lin, J. T. Feaster, J. W. Beeman, Y. Ye, E. L. Clark, D. Higgins, J. Yano, R. C. Davis, A. Mehta, T. F. Jaramillo, C. Hahn, and W. S. Drisdell. Electrochemical flow cell enabling: Operando probing of electrocatalyst surfaces by X-ray spectroscopy and diffraction. *Physical Chemistry Chemical Physics*, 21(10):5402–5408, 2019.

[105] S. B. Scott, T. V. Hogg, A. T. Landers, T. Maagaard, E. Bertheussen, J. C. Lin, R. C. Davis, J. W. Beeman, D. Higgins, W. S. Drisdell, C. Hahn, A. Mehta, B. Seger, T. F. Jaramillo, and I. Chorkendorff. Absence of Oxidized Phases in Cu Under CO Reduction Conditions. *ACS Energy Letters*, 4(3):803–804, 2019.

[106] C. Hahn, T. Hatsukade, Y. G. Kim, A. Vailionis, J. H. Baricuatro, D. C. Higgins, S. A. Nitopi, M. P. Soriaga, and T. F. Jaramillo. Engineering Cu surfaces for the electrocatalytic conversion of CO_2: Controlling selectivity toward oxygenates and hydrocarbons. *Proceedings of the National Academy of Sciences of the United States of America*, 114(23):5918–5923, 2017.

[107] P. Atkins and J. De Paula. *Atkins' Physical Chemistry*. Oxford University Press,, 2014.

[108] N. E. Henriksen and F. Y. Hansen. *Theories of Molecular Reaction Dynamics: The Microscopic Foundation of Chemical Kinetics*. Oxford University Press, 2008.

[109] V. P. Tolstoy, I. V. Chernyshova, and V. A. Skryshevsky. *Handbook of Infrared Spectroscopy of Ultrathin Films*. John Wiley & Sons, 2003.

[110] P. R. Griffiths and J. A. De Haseth. *Fourier Transform Infrared Spectrometry: Second Edition*. Wiley, 2006.

[111] M. Osawa. Surface-Enhanced Infrared Absorption. In S. Kawata, editor, *Near-Field Optics and Surface Plasmon Polaritions. Topics in Applied Physics*, volume 81, pages 163–187. Springer, Berlin, 2001.

[112] M. Osawa and M. Ikeda. Surface-enhanced infrared absorption of p-nitrobenzoic acid deposited on silver island films: contributions of electromagnetic and chemical mechanisms. *Journal of Physical Chemistry*, 95(24): 9914–9919, 1991.

[113] M. Osawa, K. Ataka, K. Yoshii, and Y. Nishikawa. Surface-enhanced infrared-spectroscopy - The origin of the absorption enhancement and band selection rule in the infrared-spectra of molecules adsorbed on fine metal particles. *Applied Spectroscopy*, 47(9):1497–1502, 1993.

[114] B. L. Mojet, S. D. Ebbesen, and L. Lefferts. Light at the interface: The potential of attenuated total reflection infrared spectroscopy for understanding heterogeneous catalysis in water. *Chemical Society Reviews*, 39(12):4643–4655, 2010.

[115] F. M. Hoffmann. Infrared reflection-absorption spectroscopy of adsorbed molecules. *Surface Science Reports*, 3(2-3):107–92, 107–192, 1983.

[116] G. Blyholder. Molecular Orbital View of Chemisorbed Carbon Monoxide. *Journal of Physical Chemistry*, 68(10):2772–2777, 1964.

[117] M. J. Weaver and X. P. Gao. In-situ electrochemical surface science. *Annual Review of Physical Chemistry*, 44(1):459–494, 1993.

[118] N. HUSH and J. REIMERS. Vibrational Stark spectroscopy 1. Basic theory and application to the CO stretch. *Journal of Physical Chemistry*, 99(43): 15798–15805, 1995.

[119] D. Lambert. Vibrational Stark effect of adsorbates at electrochemical interfaces. *Electrochimica Acta*, 41(5):623–630, 1996.

[120] S. Holloway and J. Nørskov. Changes in the vibrational frequencies of adsorbed molecules due to an applied electric field. *Journal of Electroanalytical Chemistry*, 161(1):193–198, 1984.

[121] A. Miki, S. Ye, and M. Osawa. Surface-enhanced IR absorption on platinum nanoparticles: An application to real-time monitoring of electrocatalytic reactions. *Chemical Communications*, 2(14):1500–1501, 2002.

[122] A. Miki, S. Ye, T. Senzaki, and M. Osawa. Surface-enhanced infrared study of catalytic electrooxidation of formaldehyde, methyl formate, and dimethoxymethane on platinum electrodes in acidic solution. *Journal of Electroanalytical Chemistry*, 563(1):23–31, 2004.

[123] Y. Katayama, L. Giordano, R. R. Rao, J. Hwang, H. Muroyama, T. Matsui, K. Eguchi, and Y. Shao-Horn. Surface (Electro)chemistry of CO_2 on Pt Surface: An in Situ Surface-Enhanced Infrared Absorption Spectroscopy Study. *Journal of Physical Chemistry C*, 122(23):12341–12349, 2018.

[124] M. H. Shao and R. R. Adzic. Electrooxidation of ethanol on a Pt electrode in acid solutions: In situ ATR-SEIRAS study. *Electrochimica Acta*, 50(12): 2415–2422, 2005.

[125] Y. Okinaka and M. Kato. Electroless deposition of gold. *Modern Electroplating: Fifth Edition*, pages 483–498, 2011.

[126] I. Ledezma-Yanez, E. P. Gallent, M. T. Koper, and F. Calle-Vallejo. Structure-sensitive electroreduction of acetaldehyde to ethanol on copper and its mechanistic implications for CO and CO_2 reduction. *Catalysis Today*, 262: 90–94, 2016.

[127] E. Bertheussen, A. Verdaguer Casadevall, D. Ravasio, J. H. Montoya, D. B. Trimarco, C. Roy, S. Meier, J. Wendland, J. K. Nørskov, I. E. L. Stephens, and I. Chorkendorff. Acetaldehyde as an Intermediate in the Electroreduction of Carbon Monoxide to Ethanol on Oxide-Derived Copper. *Angewandte Chemie*, 128(4):1472–1476, 2016.

[128] Y. Hori, H. Konishi, T. Futamura, A. Murata, O. Koga, H. Sakurai, and K. Oguma. "Deactivation of copper electrode" in electrochemical reduction of CO_2. *Electrochimica Acta*, 50(27):5354–5369, sep 2005.

[129] A. Wuttig and Y. Surendranath. Impurity Ion Complexation Enhances Carbon Dioxide Reduction Catalysis. *ACS Catalysis*, 5(7):4479–4484, 2015.

[130] K. J. Mayrhofer, G. K. Wiberg, and M. Arenz. Impact of glass corrosion on the electrocatalysis on Pt electrodes in alkaline electrolyte. *Journal of the Electrochemical Society*, 155(1):P1–P5, 2008.

[131] K. J. Mayrhofer, A. S. Crampton, G. K. Wiberg, and M. Arenz. Analysis of the impact of individual glass constituents on electrocatalysis on Pt electrodes in alkaline solution. *Journal of the Electrochemical Society*, 155(6): P78–P81, 2008.

[132] R. Subbaraman, N. Danilovic, P. P. Lopes, D. Tripkovic, D. Strmcnik, V. R. Stamenkovic, and N. M. Markovic. Origin of anomalous activities for electrocatalysts in alkaline electrolytes. *Journal of Physical Chemistry C*, 116 (42):22231–22237, 2012.

[133] M. Heinen, Z. Jusys, and R. J. Behm. Ethanol, acetaldehyde and acetic acid adsorption/electrooxidation on a Pt thin film electrode under continuous electrolyte flow: An in situ ATR-FTIRS flow cell study. *Journal of Physical Chemistry C*, 114(21):9850–9864, 2010.

[134] Y. G. Kim, A. Javier, J. H. Baricuatro, and M. P. Soriaga. Regulating the Product Distribution of CO Reduction by the Atomic-Level Structural Modification of the Cu Electrode Surface. *Electrocatalysis*, 7(5):391–399, 2016.

[135] Y. Hori, I. Takahashi, O. Koga, and N. Hoshi. Selective formation of C_2 compounds from electrochemical reduction of CO_2 at a series of copper single crystal electrodes. *Journal of Physical Chemistry B*, 106(1):15–17, 2002.

[136] Y. Hori, I. Takahashi, O. Koga, and N. Hoshi. Electrochemical reduction of carbon dioxide at various series of copper single crystal electrodes. *Journal of Molecular Catalysis A: Chemical*, 199(1-2):39–47, 2003.

[137] K. J. P. Schouten, E. Pérez Gallent, and M. T. M. Koper. Structure sensitivity of the electrochemical reduction of carbon monoxide on copper single crystals. *Acs Catalysis*, 3(6):1292–1295, 2013.

[138] M. G. Samant, M. F. Toney, G. L. Borges, L. Blum, and O. R. Melroy. Grazing incidence X-ray diffraction of lead monolayers at a silver (111) and gold (111) electrode/electrolyte interface. *Journal of Physical Chemistry*, 92(1):220–225, 1988.

[139] R. R. Rao, M. J. Kolb, N. B. Halck, A. F. Pedersen, A. Mehta, H. You, K. A. Stoerzinger, Z. Feng, H. A. Hansen, H. Zhou, L. Giordano, J. Rossmeisl, T. Vegge, I. Chorkendorff, I. Stephens, and Y. Shao-Horn. Towards identifying the active sites on RuO_2(110) in catalyzing oxygen evolution. *Energy and Environmental Science*, 10(12):2626–2637, 2017.

[140] C. A. Lucas and N. M. Marković. *In-situ X-ray Diffraction Studies of the Electrode/Solution Interface*, chapter 1, pages 1–45. John Wiley and Sons, Ltd, 2008.

[141] W. Sheng, S. Kattel, S. Yao, B. Yan, Z. Liang, C. J. Hawxhurst, Q. Wu, and J. G. Chen. Electrochemical reduction of CO_2 to synthesis gas with controlled CO/H_2 ratios. *Energy and Environmental Science*, 10(5):1180–1185, 2017.

[142] A. Eilert, F. S. Roberts, D. Friebel, and A. Nilsson. Formation of Copper Catalysts for CO_2 Reduction with High Ethylene/Methane Product Ratio Investigated with in Situ X-ray Absorption Spectroscopy. *Journal of Physical Chemistry Letters*, 7(8):1466–1470, 2016.

[143] C. Gattinoni and A. Michaelides. Atomistic details of oxide surfaces and surface oxidation: the example of copper and its oxides. *Surface Science Reports*, 70(3):437, 424–447, 2015.

[144] A. S. Varela Gasque, C. G. Schlaup, Z. P. Jovanov, P. Malacrida, S. Horch, I. E. L. Stephens, and I. Chorkendorff. CO_2 Electroreduction on Well-Defined Bimetallic Surfaces: Cu Overlayers on Pt(111) and Pt(211). *Journal of Physical Chemistry C*, 117(40):2020500–20508, 2013.

[145] J. Salimon, R. M. Hernández-Romero, and M. Kalaji. The dynamics of the conversion of linear to bridge bonded CO on Cu. *Journal of Electroanalytical Chemistry*, 538-539:99–108, 2002.

[146] S. Mezzavilla, S. Horch, I. E. L. Stephens, B. Seger, and I. Chorkendorff. Structure Sensitivity in the Electrocatalytic Reduction of CO_2 with Gold Catalysts. *Angewandte Chemie*, 131(12):3814–3818, 2019.

[147] P. P. Olivera, M. Patrito, and H. Sellers. Electronic structure calculations of polyatomic oxyanions adsorbed on metal surfaces. *Interfacial Electrochemistry: Theory: Experiment, and Applications*, pages 63–81, 2017.

[148] D. D. Bode, T. N. Andersen, and H. Eyring. Anion and pH effects on the potentials of zero charge of gold and silver electrodes. *Journal of Physical Chemistry*, 71(4):792–797, 1967.

[149] D. Kolb and J. Schneider. Surface reconstruction in electrochemistry: Au(100)-(5 x 20), Au(111)-(1 x 23) and Au(110)-(1 x 2). *Electrochimica Acta*, 31(31): 929–936, 1985.

[150] K. Ataka, T. Yotsuyanagi, and M. Osawa. Potential-dependent reorientation of water molecules at an electrode/electrolyte interface studied by surface-enhanced infrared absorption spectroscopy. *Journal of Physical Chemistry*, 100 (25):10664–10672, 1996.

[151] K. Engelsmann, W. Lorenz, and E. Schmidt. Underpotential deposition of lead on polycrystalline and single-crystal gold surfaces: Part I. Thermodynamics. *Journal of Electroanalytical Chemistry and Interfacial Electrochemistry*, 114(1):1–10, 1980.

[152] K. Ataka, G. Nishina, W. B. Cai, S. G. Sun, and M. Osawa. Dynamics of the dissolution of an underpotentially deposited Cu layer on Au(111): A combined time-resolved surface-enhanced infrared and chronoamperometric study. *Electrochemistry Communications*, 2(6):417–421, 2000.

[153] T. A. Morhart, B. Unni, M. J. Lardner, and I. J. Burgess. Electrochemical ATR-SEIRAS Using Low-Cost, Micromachined Si Wafers. *Analytical Chemistry*, 89 (21):11818–11824, 2017.

Appendix A

Additional plots for ATR-SEIRAS on Cu

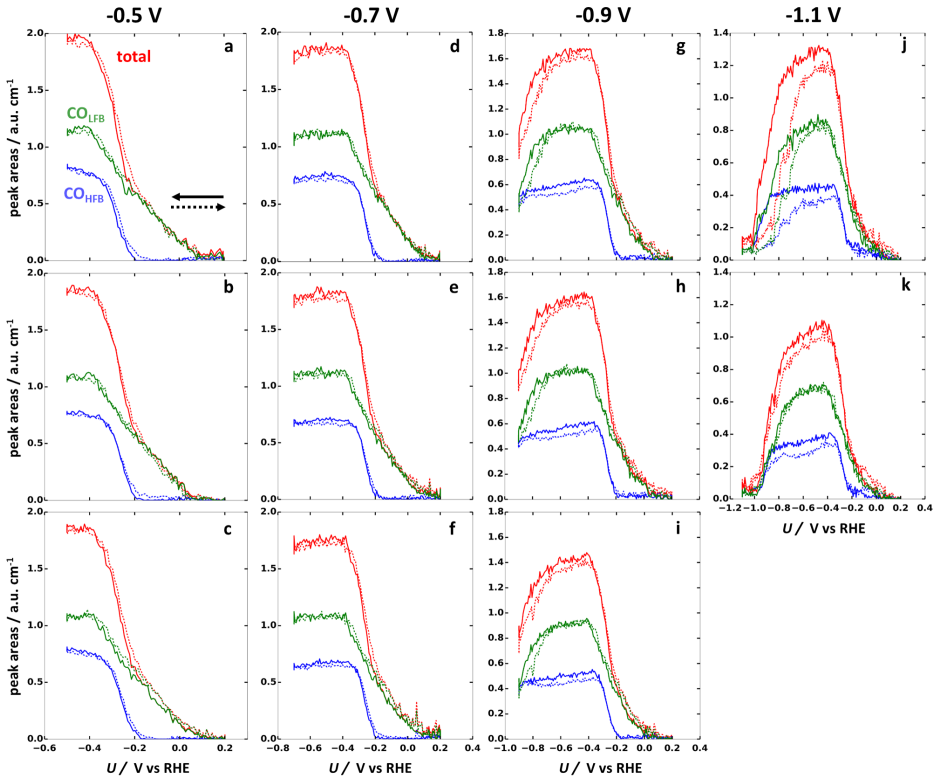

Figure A.1: All integrated peak areas for CO on Cu in CO saturated 0.1 M $KHCO_3$, corresponding to CVs shown in Figure 6.5. Plotted against potential with full line for cathodic and stippled line for anodic branch, respectively. Blue lines indicate the area for the high frequency band, green for the low frequency band, and red the sum. All CVs started at +0.2 V vs RHE and were scanned at 2 mV/s to a cathodic potential of -0.5 (a, b, c), -0.7 (d, e, f), -0.9 (g, h, i) and -1.1 (j, k) V vs RHE. After holding the cathodic potential for 60 s the potential was scanned back at 2 mV/s to +0.2 V. Subfigures are labelled in order they were measured. Note that the y-axis range varies depending on the cathodic turning potential.

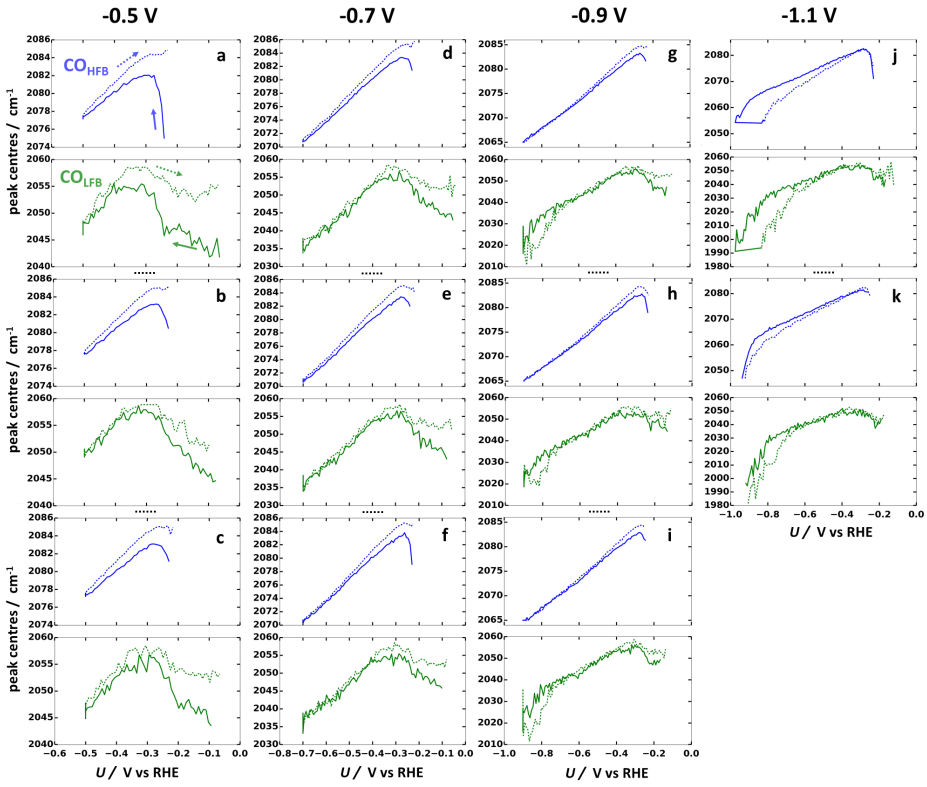

Figure A.2: All integrated peak centres for CO on Cu in CO saturated 0.1 M $KHCO_3$, corresponding to CVs shown in Figure 6.5. Otherwise as in Figure A.1. Only the region where the peak intensity was high enough to give a good fit of the position has been plotted. The criteria are integrated intensities > 0.15 a.u. cm^{-1} for the high frequency band and > 0.30 a.u. cm^{-1} for the low frequency band. For -1.1 V vs RHE these limits were lowered to 0.12 and 0.2 a.u. cm^{-1}, respectively, due to lower total intensity. Note that the y-axis range varies depending on the cathodic turning potential.

Appendix B

Papers

Published papers

In the following, the papers where I have contributed have been included with permission from the publisher. The SI for paper II was also included due to the very compact nature of the main paper and Figure S5 is referred to in the main part of the thesis.

Paper I:
Electroreduction of CO on Polycrystalline Copper at Low Overpotentials
Erlend Bertheussen, Thomas V. Hogg, Albert K. Engstfeld, Younes Abghoui, Ib Chorkendorff and Ifan E.L. Stephens.
ACS Energy Letters 2018, 3, 3, 634-640

Paper II:
Absence of Oxidized Phases in Cu under CO Reduction Conditions
Soren B. Scott, Thomas V. Hogg, Alan T. Landers, Thomas Maagaard, Erlend Bertheussen, John C. Lin, Ryan C. Davis, Jeffrey W. Beeman, Drew Higgins, Walter S. Drisdell, Christopher Hahn, Apurva Mehta, Brian Seger, Thomas F. Jaramillo and Ib Chorkendorff.
ACS Energy Letters 2019, 4, 3, 803-804

Planned papers

It is currently planned to publish papers based on the ATR-SEIRAS sections related to CO reduction on Cu (Section 6.3) and blocking of sites with Pb on Au (Section 6.4.2).

ACS Energy LETTERS

Cite This: ACS Energy Lett. 2018, 3, 634−640

LETTER

Electroreduction of CO on Polycrystalline Copper at Low Overpotentials

Erlend Bertheussen,[¶,†] Thomas V. Hogg,[¶,†] Younes Abghoui,[†,‡] Albert K. Engstfeld,[†,§] Ib Chorkendorff,[*,†] and Ifan E. L. Stephens[*,†,∥]

[†]Section for Surface Physics and Catalysis, Department of Physics, Technical University of Denmark, DK-2800 Kgs. Lyngby, Denmark

[‡]Science Institute and Faculty of Physical Sciences, VR-III, University of Iceland, IS-107 Reykjavik, Iceland

[§]Institute of Surface Chemistry and Catalysis, Ulm University, D-89069 Ulm, Germany

[∥]Department of Materials, Imperial College London, Royal School of Mines, London SW7 2AZ, U.K.

Supporting Information

ABSTRACT: Cu is the only monometallic electrocatalyst to produce highly reduced products from CO_2 selectively because of its intermediate binding of CO. We investigate the performance of polycrystalline Cu for the electroreduction of CO in alkaline media (0.1 M KOH) at low overpotentials (−0.4 to −0.6 V vs RHE). We find that polycrystalline Cu is highly active at these potentials. The overall CO reduction rates are comparable to those of the nanostructured forms of the material, albeit with a distinct product distribution. While nanostructured forms of Cu favor alcohols, polycrystalline Cu produces greater amounts of C_2 and C_3 aldehydes, as well as ethylene.

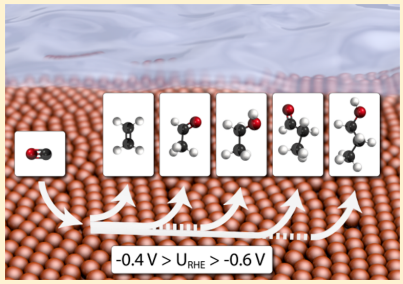

Electrochemical reduction using renewable energy is emerging as a promising means of recycling carbon dioxide (CO_2) from point sources or ambient air into useful chemicals.[1−3] This way, the anthropogenic carbon cycle can be closed and our dependence on fossil energy sources to produce fuels and commodity chemicals can be reduced. The successful implementation of this technology requires development of electrocatalysts that can produce the desired product(s) efficiently and selectively.[1,2] Examples of useful products are energy-rich compounds such as hydrocarbons and oxygenates that can be used either as fuels or commodity chemicals.[1] Multi-carbon (C_{2+}) products are of special interest because of their high energy density.[4] Moreover, unlike C_1 products such as methanol, they are particularly challenging to synthesize via thermally activated CO or CO_2 reduction methods.[5]

Copper is the only pure metal that can convert CO_2 into highly reduced and C−C coupled products in significant amounts.[6,7] This process, however, requires large overpotentials, and a large number of compounds are produced. In order to make CO_2 reduction suitable for large-scale energy conversion, significant improvements are necessary. One approach is to use a tandem system whereby CO_2 is reduced in two stages: (i) convert CO_2 to CO followed by (ii) further reduction of CO to more energy-rich products.[8] Several catalysts, including nanostructured Au,[9−11] Ag,[12] and transition-metal doped nitrogenated carbon,[13−15] are highly selective and moderately active for the first step. For the second step, Cu-based materials are the only catalysts to reduce CO at significant rates and with reasonable selectivity.[16] In particular, works led by Hori[16] and Koper[17] showed that C_{2+} products are favored under more alkaline conditions; subsequent theoretical works suggested that C−C coupling barriers are lower at high pH.[18,19] Moreover, increased surface roughness generally seems to favor the production of C_{2+} products, such as ethylene, from CO_2.[20−24] Here, it is worth pointing out the significant difference in performance between aqueous half-cell measurements and experiments performed in real devices.[1] In aqueous electrolytes, CO_2 and CO reduction is limited by the low solubility of the reactant gas.[4] One means of dealing with this issue is to conduct experiments on gas diffusion electrodes, which are not completely submerged in the electrolyte.[25,26]

Building upon the earlier findings regarding CO reduction on Cu electrodes, Kanan and co-workers showed that oxide-derived, nanostructured copper has a high (geometrically normalized) activity toward CO reduction at low overpotentials in 0.1 M KOH.[8] These electrodes exhibited high selectivity

Received: January 20, 2018
Accepted: February 8, 2018
Published: February 8, 2018

DOI: 10.1021/acsenergylett.8b00092
ACS Energy Lett. 2018, 3, 634−640

toward ethanol, with a maximum Faradaic efficiency of 43% at −0.3 V vs RHE. The authors attributed the activity to a high density of grain boundary surface terminations.[8,27] A study from our own laboratory showed that the CO reduction activity of oxide-derived Cu was strongly correlated to the presence of a site, presumably undercoordinated, with exceptionally strong interaction with CO.[28] Other groups have also reported that stepped or kinked surfaces yield higher proportions of oxygenates, relative to hydrocarbons, from CO_2 or CO reduction.[29−31] This phenomenon is likely related to the more favorable free-energy pathway for aldehyde reduction to alcohols on high-index Cu surfaces than on terraces.[32]

Oxide-derived Cu evidently has a complex surface chemistry;[27,28] moreover, its porous morphology is likely to yield mesoscopic transport effects during CO reduction, especially given the involvement of soluble intermediates such as acetaldehyde.[33−35] On the other hand, the chemistry of CO reduction on polycrystalline Cu should be simpler; on that basis, it could be used as a robust benchmark for activity measurements. To the best of our knowledge, there are only two reports in the literature that quantify the activity and selectivity of planar polycrystalline Cu for CO reduction in 0.1 M KOH.[28,36] Even so, there is significant variability between those two reports, as described in more detail in the Supporting Information (Section S3 and Figure S1). This leads us to the focus of the current investigation, which is to establish the following: *What is the activity of polycrystalline Cu for CO reduction, a viable benchmark for this reaction on copper-based electrodes? How does it compare in terms of activity and Faradaic efficiency to literature data on nanostructured copper materials?* On the basis of our current understanding, we aim to establish the reasons for the fundamental differences in catalytic performance between polycrystalline and nanostructured Cu. Consequently, we investigate CO reduction on polycrystalline copper foils between −0.40 V and −0.59 V vs RHE (all potentials are referred to this scale in the following), i.e., at potentials more positive than previously reported for this material. We report appreciable activity and selectivity to CO reduction across this potential range. We also show that the total CO reduction current density of polycrystalline copper is comparable to that of oxide-derived copper, when normalized to electrochemical surface area (ECSA).

Activity and Product Distribution from CO Reduction on Polycrystalline Cu. We carried out short-term (∼30 min) chronoamperometric CO reduction measurements at three different potentials, i.e., −0.40, −0.50, and −0.59 V vs RHE in CO-saturated 0.1 M KOH electrolyte using a glass H-cell. The resulting Faradaic efficiencies and partial current densities for the individual products are shown in panels a and b of Figure 1, respectively. Within the uncertainty of our measurements, we could account for a 100% balance of charge with products detected, including both H_2 and compounds derived from CO reduction. The Faradaic efficiency toward CO reduction increases from 40% at −0.40 V to 56% at −0.59 V. Consistent with earlier reports on oxide-derived Cu,[8,27,28,33] only C_{2+} products are formed under these conditions. The two major CO reduction products are propionaldehyde (with a maximum Faradaic efficiency of 18% at −0.50 V) and ethylene (30% at −0.59 V). The other CO reduction products are ethanol, 1-propanol, acetaldehyde, and acetate. The rates toward alcohol production are particularly high at the most negative potential, −0.59 V where the concentration of 1-propanol exceeds the detection limit of our analytical equipment. Notably, we

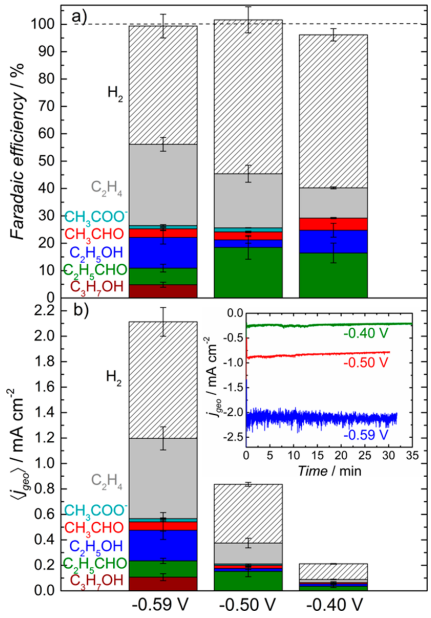

Figure 1. Faradaic efficiency (a) and mean partial current density (b) from chronoamperometric CO reduction on polycrystalline Cu performed in CO-saturated 0.1 M KOH at −0.40, −0.50, and −0.59 V vs RHE. Data represent the average of 3 individual measurements, and error bars indicate ±σ. Inset: Chronoamperometry traces from representative measurements at each potential. Measurements were carried out until a certain charge was reached (0.5 C at −0.40 V, 1.5 C at −0.50 V, and 4.0 C at −0.59 V).

measured significant CO reduction partial current densities, up to 1.2 mA cm^{-2} at −0.59 V.

Another important observation is how the product distribution changes with the applied potential. Among the oxygenated compounds, aldehydes are formed primarily at the more positive potentials, while alcohol formation becomes more prominent at −0.59 V. Several studies, including results from our group, show that acetaldehyde is an intermediate in the production of ethanol.[16,32,33] Hori et al. reported that propionaldehyde could be reduced to 1-propanol on polycrystalline Cu, strongly suggesting that also the C_3 aldehyde is an intermediate in alcohol formation.[16] It seems that applying −0.59 V instead of −0.50 V accelerates aldehyde conversion to alcohols. It is worth noting that aldehydes are challenging to detect in alkaline solutions using routine NMR spectroscopy.[33,37] However, our use of static headspace-gas chromatography (HS-GC) enables us to measure these compounds with high sensitivity.

Comparison with Literature Data for Polycrystalline Cu and Nanostructured Cu. Figure 2 compares the total CO reduction current densities of this work with some results from relevant studies reported in the literature. An interesting comparison can be drawn between the results from the present study and previously published data from oxide-derived Cu and Cu nanoparticles. It seems that nanostructured electrodes reach mass transport limitations for CO reduction at potentials just cathodic of −0.30 to −0.35 V. By extrapolating the first two to three points in the ECSA-normalized data, it seems that these

DOI: 10.1021/acsenergylett.8b00092
ACS Energy Lett. 2018, 3, 634−640

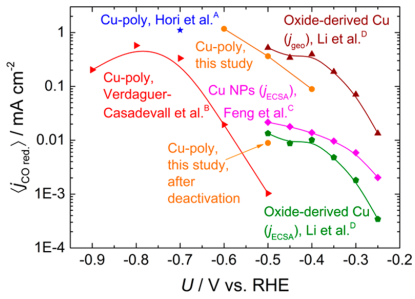

Figure 2. Comparison of mean partial current densities for CO reduction on polycrystalline Cu, oxide-derived Cu, and Cu nanoparticles. Oxide-derived Cu is normalized to both geometric and electrochemically active surface area. The results from the current study are the same as those shown in Figure 1 and are compared with data adapted from (A) Hori et al.,[36] (B) Verdaguer-Casadevall et al.,[28] (C) Feng et al.,[27] and (D) Li et al.[8] The bottom orange point represents the result from a sample after deactivation, for which detailed data are shown in Figure S2. We have summarized the roughness factors we used for the ECSA normalization in Table S2, obtained from each of the relevant studies. We assume that the polycrystalline Cu electrodes have a roughness factor of 1.

lines would roughly coincide with the polycrystalline data from the present work. Thus, according to our data, there is no significant difference between the CO reduction activity of planar polycrystalline Cu and nanostructured oxide-derived Cu: the high current densities of the oxide-derived Cu, when normalized to geometric surface area, are due to the exceptionally large roughness factors of 39 or higher. This important observation shows that nanostructuring is not a prerequisite for high CO reduction activity.

There are significant variations in product distribution between polycrystalline and nanostructured copper electrodes. An example of this is the difference in ethylene production. Polycrystalline copper shows significant selectivity to ethylene at all potentials measured in this study, in particular at −0.5 V and more cathodic. On nanostructured copper, on the other hand, ethylene is not produced in significant amounts, probably because these catalysts are mass transport limited in the region where hydrocarbons are normally produced. At the same time, oxygenates are almost exclusively produced from CO reduction on nanostructured electrodes when not mass transport limited. It has been shown for CO_2 reduction that oxygenates are generally produced at lower overpotentials than hydrocarbons.[38] This points toward the different potential regions accessible on planar and nanostructured surfaces as a likely reason for the variation in oxygenate selectivity. The high ECSA of the nanostructured electrodes allows for measurements at lower overpotentials, because the larger geometric current density allows for adequate product analysis even though the ECSA-normalized current density is low. On the other hand, such electrodes reach mass transport limitations at potentials as positive as −0.35 V, as discussed above. As a result, the potential range accessible to measurements is distinct from planar electrodes. It is also evident that nanostructured oxide-derived Cu yields higher selectivity to energy-rich alcohols than planar polycrystalline Cu.[8,33] We attribute this phenomenon to two effects: (i) oxide-derived Cu has more strong-binding undercoordinated sites, which are more effective at reducing aldehydes to alcohols, as discussed in the introduction, and (ii) the porosity leads to enhanced retention of aldehydes, accelerating their reduction to alcohols. We emphasize that the low ECSA of polycrystalline Cu makes it an unsuitable CO reduction catalyst for commercial purposes. However, we consider it provides an excellent, simple-to-reproduce benchmark. Moreover, it is of critical interest to establish the differences between it and nanostructured forms of Cu in order to design improved catalyst materials.

When the individual studies on polycrystalline copper are compared, it can be seen that they differ significantly from each other. For instance, our present results exhibit significant CO reduction activity for polycrystalline copper between −0.40 and −0.59 V, whereas the results of an earlier collaboration between our group and Kanan and co-workers showed little to no CO reduction activity at potentials between −0.50 and −0.90 V on similar electrodes.[28] We speculate that these differences could be caused, at least partly, by the longer duration of the measurements in that study. They were carried out for 2−3 h, a period in which the electrodes in the current study experience significant deactivation. We mainly attribute this deactivation to poisoning by silicon from the glassware, as discussed in detail below. In Figure 2, we show a data point from a measurement carried out on an electrode that had already been deactivated in argon-purged electrolyte (the chronoamperometry trace and Faradaic efficiency are shown in Figure S2). Its activity is much closer to the data from Verdaguer-Casadevall et al., suggesting that those measurements could have been affected by silicon poisoning. In addition to the studies mentioned above, Koper and co-workers also investigated CO reduction on polycrystalline Cu.[40] They observed formation of ethylene between −0.35 and −0.60 V on polycrystalline Cu, but with insignificant overall current densities. The authors used online electrochemical mass spectrometry (OLEMS) for product analysis: this technique is highly sensitive to gas-phase species; however, it is challenging to use it to yield quantitative measurements of reaction rates. On that basis, we have not included data from this study in Figure 2.

In general, the low ECSA of planar electrodes makes them far more susceptible to poisoning by impurities than their nanostructured counterparts with a more favorable electrode area/electrolyte volume ratio. When studying the intrinsic behavior of low surface area electrocatalysts, we recommend keeping the measurement time as short as possible, so that the effect of any impurities that might be present is minimized. For CO_2/CO reduction measurements, the measurement duration is normally limited by accumulation of liquid products above the detection limits of the analytical equipment used.

Another reason for the discrepancies between the different studies on polycrystalline copper could be differences in initial electrode surface structure. In Figure S3, we show that different batches of copper foils from the same supplier can give significantly different features in cyclic voltammetry curves under inert gas conditions. This is reflected in the CO reduction activity shown in Figure S4, where the foil that exhibits more (100)-like features shows higher CO reduction selectivity, in particular toward ethylene formation. Several groups have shown that the surface orientation of copper electrocatalysts can have a significant effect on CO_2 and CO reduction performance.[29−31,39−43] Thus, we conjecture that the surface orientation of different polycrystalline foils could also vary significantly, hence affecting the catalyst activity.

DOI: 10.1021/acsenergylett.8b00092
ACS Energy Lett. 2018, 3, 634−640

Deactivation for Extended Measurements. Using our current experimental setup, it is challenging to maintain the activity of Cu for extended periods of time. Representative chronoamperometry traces for short-term measurements are shown in the inset of Figure 1b. The high CO reduction activity that we described above is relatively stable over the course of ∼30 min at all three potentials. A minor loss of activity can be observed at −0.40 V and −0.50 V, while the measurements at −0.59 V are completely stable. Significant deactivation occurs on a longer time scale, however, as shown in Figure 3 (current

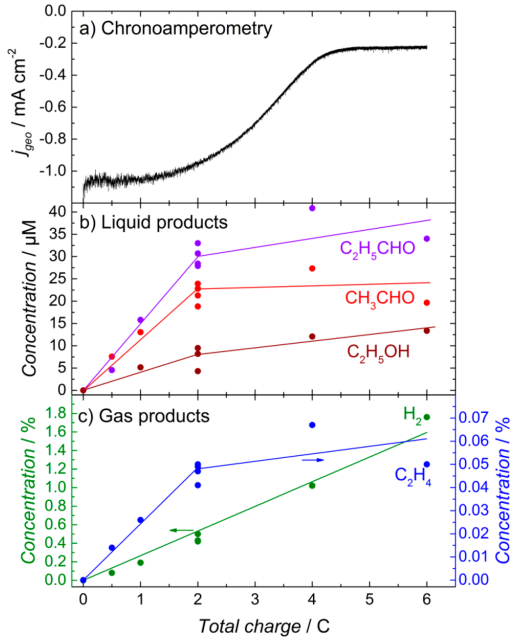

Figure 3. CO reduction measurements at −0.52 V in CO-saturated 0.1 M KOH. (a) Chronoamperometry trace for a measurement stopped at 6 C charge. (b) Concentration of the liquid products ethanol, acetaldehyde, and propionaldehyde as a function of total measurement charge. (c) Concentration of the individual gaseous products as a function of total measurement charge. Note: 1-Propanol and acetate are not shown in panel b. 1-Propanol was not produced in concentrations above our detection limits at this potential, and acetate was measured using NMR spectroscopy, which was not carried out for these measurements. Acetate is a minor product quantified to ∼1% Faradaic efficiency in other measurements. Each data point in panels b and c represents data from an individual measurement. Lines have been added to guide the eye. The corresponding duration of each measurement is shown in Figure S6b.

density as a function of time for the same measurement is shown in Figure S5; total CO reduction partial current density for each point is shown in Figure S6b). For the measurement shown in Figure 3a, the initial current density decreases by almost 80%. At the same time, a strong shift in product distribution can be observed. In panels b and c of Figure 3, the development of product concentration with total measurement charge is shown for liquid and gaseous products, respectively. The H_2 concentration increases linearly with accumulated measurement charge. On the other hand, at the point where the current density starts rapidly decreasing, the concentration of the CO reduction products ethylene, acetaldehyde, propionaldehyde, and ethanol reaches a plateau. The slope of the H_2 concentration would, in principle, be expected to increase when deactivation starts because of an increase in Faradaic efficiency. A minor leakage of H_2 for measurements longer than ∼30 min could be the reason that this is not the case.

The observed catalyst deactivation could be caused by several effects, including (i) changes in the elemental composition of the surface due to accumulation of impurities;[44−48] (ii) the electropolished Cu surface undergoing a structural transformation under reaction conditions;[30,39,49] and/or (iii) self-poisoning of the surface by reaction products/intermediates, as shown previously for other reactions, e.g., by Heinen et al. for the electrooxidation of ethanol.[34] In order to investigate possible impurity deposition of the electrode, we performed X-ray photoelectron spectroscopy (XPS) studies after the CO reduction measurement. In Figure 4, we show XPS spectra of

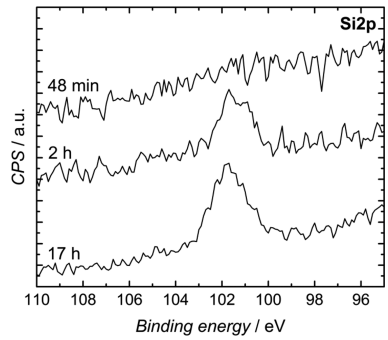

Figure 4. XPS spectra of the Si 2p binding energy region on polycrystalline copper foils after CO reduction at −0.50 V with different durations. Note: Each measurement is carried out on a new CO reduction sample.

the Si 2p region measured on copper electrodes after different electrolysis times. For short-term measurements, where significant deactivation has not yet occurred, little or no Si can be detected on the surface with this technique. For longer measurements, however, the Si 2p line is clearly visible, suggesting that there might be a correlation between the presence of Si and the deactivation. Mayrhofer et al. showed that Pb and Si, derived from glass corrosion under alkaline conditions, can poison reactions such as O_2 reduction on Pt.[44,45] Because we are using glass cells for these measurements, it is a plausible reason for the deactivation we see. Figure S7 shows a survey spectrum of an electrode after long-term CO reduction. No clear lines of other possible metallic contaminants are present.

To investigate whether self-poisoning by aldehydes contributes to the observed deactivation, we added acetaldehyde and propionaldehyde to Ar-saturated 0.1 M KOH and carried out chronoamperometry measurements at −0.50 V. We chose aldehydes for this measurement as a result of our previous observation that acetaldehyde undergoes spontaneous organic reactions in alkaline solution, including polymerization.[33] The resulting trace is displayed in Figure S8. Initially, an increased current density can be observed, suggesting that the aldehydes

DOI: 10.1021/acsenergylett.8b00092
ACS Energy Lett. 2018, 3, 634−640

do not immediately poison the surface. The electrode does, however, start losing activity after ~30 min, similarly to the long-term CO reduction measurement shown in Figure S5. In order to elucidate if restructuring of the electrode under reaction conditions occurs and influences the activity, we also investigated the behavior of the electrode when kept at −0.50 V in Ar-purged electrolyte, before switching to CO. The resulting chronoamperometry trace and the respective product distribution are shown in Figure S2. After an initial activation, the H_2 evolution current starts to deactivate as well. After switching to CO, the initial activity is significantly lower than that of a freshly electropolished electrode. Furthermore, only small amounts of CO reduction products could be detected. These experiments together suggest that self-poisoning by reaction intermediates is not causing the deactivation. They do not, however, conclusively show if silicon poisoning, restructuring, or a combination of both effects is causing it.

In this study, we investigated the activity and product distribution of polycrystalline Cu for the reduction of CO at low overpotentials in alkaline media. We measured more than 50% Faradaic efficiency for CO reduction, primarily due to the formation of C_2 and C_3 aldehydes and alcohols, as well as ethylene. A comparison of data from this work with results reported previously in the literature indicates that polycrystalline Cu can yield CO reduction rates comparable to that of oxide-derived, nanostructured Cu. Even so, oxide-derived Cu favors the production of highly coveted energy-rich alcohols; we attribute this difference to a higher abundance of undercoordinated sites and decreased mass transport within the pores of oxide-derived Cu. In summary, by performing bulk electrolysis measurements using three different analytical chemistry techniques, we demonstrate that planar polycrystalline copper exhibits activity for CO reduction equivalent to that of state-of-the-art nanostructured catalyst materials. The enhanced current densities afforded by nanostructured surfaces are only due to the large surface area. Future studies should focus on improving the *intrinsic activity* of Cu.

EXPERIMENTAL SECTION

A more detailed description of materials used (Section S1) and experimental details (Section S2) can be found in the Supporting Information.

Polycrystalline copper electrodes were cut to a size of 5 × 10 mm, and a piece of copper wire was attached. The electrodes were electropolished in 30% phosphoric acid and rinsed thoroughly with Milli-Q water. The procedure was carried out immediately before the electrode was mounted in the custom-made H-cell. The electrolyte was purged with CO for 15 min at 30 sccm. The ohmic resistance was measured using electrochemical impedance spectroscopy. 85% of the Ohmic drop was compensated for in the EC-Lab software, and postmeasurement correction was applied to account for the final 15%. A Hg/Hg_2SO_4 reference electrode was used for all measurements, converted into the RHE scale by calibration against the onset of H_2 evolution/H_2 oxidation on a Pt electrode. CO reduction was carried out in batch measurements. Chronoamperometry was carried out until a certain amount of charge was passed. For short-term measurements the values for total measurement charge were 0.5 C at −0.40 V, 1.5 C at −0.50 V, and 4.0 C at −0.59 V. The average current from a measurement was used in later analyses. After chronoamperometry, 250 μL of the gas mixture was injected in the GC. Liquid product analysis was performed using HS-GC and NMR spectroscopy following the protocols from a previous publication.[37] XPS was performed using an Al Kα X-ray source. An Ar flood gun was used for sample charge neutralization.

ASSOCIATED CONTENT

Supporting Information

The Supporting Information is available free of charge on the ACS Publications website at DOI: 10.1021/acsenergylett.8b00092.

Materials; detailed experimental methods; existing literature regarding CO reduction on polycrystalline Cu; prereduction in Ar; roughness factors; cyclic voltammograms and product distribution measured on two different batches of Cu foils; chronoamperometry trace and charge dependence of long-term measurements; XPS survey spectrum; aldehyde reduction; tabulated values for CO reduction activity and product distribution (PDF)

AUTHOR INFORMATION

Corresponding Authors

*E-mail: ibchork@fysik.dtu.dk.

*E-mail: i.stephens@imperial.ac.uk.

ORCID

Ib Chorkendorff: 0000-0003-2738-0325

Ifan E. L. Stephens: 0000-0003-2157-492X

Author Contributions

¶E.B. and T.V.H. contributed equally to this work.

Notes

The authors declare no competing financial interest.

ACKNOWLEDGMENTS

This work was funded by the Villum Foundation V-SUSTAIN grant 9455 to the Villum Center for the Science of Sustainable Fuels and Chemicals. Y.A. received funding from The Icelandic Research Fund; A.K.E. received funding from the People Program (Marie Curie Actions) of the European Union's Seventh Framework Program (FP7/2007-2013) under REA Grant Agreement No. 609405 (COFUNDPostdocDTU) [information available on web site]. We thank Jakob Kibsgaard for producing the abstract and table of contents graphic.

REFERENCES

(1) Whipple, D. T.; Kenis, P. J. A. Prospects of CO_2 Utilization via Direct Heterogeneous Electrochemical Reduction. *J. Phys. Chem. Lett.* **2010**, *1*, 3451−3458.

(2) Seh, Z. W.; Kibsgaard, J.; Dickens, C. F.; Chorkendorff, I.; Nørskov, J. K.; Jaramillo, T. F. Combining Theory and Experiment in Electrocatalysis: Insights into Materials Design. *Science* **2017**, *355*, eaad4998.

(3) Hori, Y. Electrochemical CO_2 Reduction on Metal Electrodes. In *Modern Aspects of Electrochemistry*; Vayenas, C. G., White, R. E., Gamboa-Aldeco, M. E., Eds.; Springer: New York, 2008; Vol. *42*, pp 89−189.

(4) *CRC Handbook of Chemistry and Physics*, 97th ed.; Haynes, W. M., Ed.; CRC Press/Taylor & Francis: Boca Raton, FL, 2016.

(5) Medford, A. J.; Lausche, A. C.; Abild-Pedersen, F.; Temel, B.; Schjødt, N. C.; Nørskov, J. K.; Studt, F. Activity and Selectivity Trends in Synthesis Gas Conversion to Higher Alcohols. *Top. Catal.* **2014**, *57*, 135−142.

(6) Hori, Y.; Wakebe, H.; Tsukamoto, T.; Koga, O. Electrocatalytic Process of CO Selectivity in Electrochemical Reduction of CO_2 at

DOI: 10.1021/acsenergylett.8b00092
ACS Energy Lett. 2018, 3, 634−640

Metal Electrodes in Aqueous Media. *Electrochim. Acta* **1994**, *39*, 1833−1839.
(7) Bagger, A.; Ju, W.; Varela, A. S.; Strasser, P.; Rossmeisl, J. Electrochemical CO_2 Reduction: A Classification Problem. *ChemPhysChem* **2017**, *18*, 3266−3273.
(8) Li, C. W.; Ciston, J.; Kanan, M. W. Electroreduction of Carbon Monoxide to Liquid Fuel on Oxide-Derived Nanocrystalline Copper. *Nature* **2014**, *508*, 504−507.
(9) Zhu, W.; Michalsky, R.; Metin, Ö.; Lv, H.; Guo, S.; Wright, C. J.; Sun, X.; Peterson, A. A.; Sun, S. Monodisperse Au Nanoparticles for Selective Electrocatalytic Reduction of CO_2 to CO. *J. Am. Chem. Soc.* **2013**, *135*, 16833−16836.
(10) Zhu, W.; Zhang, Y.-J.; Zhang, H.; Lv, H.; Li, Q.; Michalsky, R.; Peterson, A. A.; Sun, S. Active and Selective Conversion of CO_2 to CO on Ultrathin Au Nanowires. *J. Am. Chem. Soc.* **2014**, *136*, 16132−16135.
(11) Chen, Y.; Li, C. W.; Kanan, M. W. Aqueous CO_2 Reduction at Very Low Overpotential on Oxide-Derived Au Nanoparticles. *J. Am. Chem. Soc.* **2012**, *134*, 19969−19972.
(12) Mistry, H.; Choi, Y.-W.; Bagger, A.; Scholten, F.; Bonifacio, C. S.; Sinev, I.; Divins, N. J.; Zegkinoglou, I.; Jeon, H. S.; Kisslinger, K.; et al. Enhanced Carbon Dioxide Electroreduction to Carbon Monoxide over Defect-Rich Plasma-Activated Silver Catalysts. *Angew. Chem., Int. Ed.* **2017**, *56*, 11394−11398.
(13) Varela, A. S.; Ranjbar Sahraie, N.; Steinberg, J.; Ju, W.; Oh, H. S.; Strasser, P. Metal-Doped Nitrogenated Carbon as an Efficient Catalyst for Direct CO_2 Electroreduction to CO and Hydrocarbons. *Angew. Chem., Int. Ed.* **2015**, *54*, 10758−10762.
(14) Bagger, A.; Ju, W.; Varela, A. S.; Strasser, P.; Rossmeisl, J. Single Site Porphyrine-Like Structures Advantages over Metals for Selective Electrochemical CO_2 reduction. *Catal. Today* **2017**, *288*, 74−78.
(15) Ju, W.; Bagger, A.; Hao, G. P.; Varela, A. S.; Sinev, I.; Bon, V.; Roldan Cuenya, B.; Kaskel, S.; Rossmeisl, J.; Strasser, P. Understanding Activity and Selectivity of Metal-Nitrogen-Doped Carbon Catalysts for Electrochemical Reduction of CO_2. *Nat. Commun.* **2017**, *8*, 944.
(16) Hori, Y.; Takahashi, R.; Yoshinami, Y.; Murata, A. Electrochemical Reduction of CO at a Copper Electrode. *J. Phys. Chem. B* **1997**, *101*, 7075−7081.
(17) Schouten, K. J. P.; Kwon, Y.; van der Ham, C. J. M.; Qin, Z.; Koper, M. T. M. A New Mechanism for the Selectivity to C_1 and C_2 Species in the Electrochemical Reduction of Carbon Dioxide on Copper Electrodes. *Chem. Sci.* **2011**, *2*, 1902.
(18) Calle-Vallejo, F.; Koper, M. T. M. Theoretical Considerations on the Electroreduction of CO to C_2 Species on Cu(100) Electrodes. *Angew. Chem., Int. Ed.* **2013**, *52*, 7282−7285.
(19) Montoya, J. H.; Shi, C.; Chan, K.; Nørskov, J. K. Theoretical Insights into a CO Dimerization Mechanism in CO_2 Electroreduction. *J. Phys. Chem. Lett.* **2015**, *6*, 2032−2037.
(20) Tang, W.; Peterson, A. A.; Varela, A. S.; Jovanov, Z. P.; Bech, L.; Durand, W. J.; Dahl, S.; Nørskov, J. K.; Chorkendorff, I. The Importance of Surface Morphology in Controlling the Selectivity of Polycrystalline Copper for CO_2 Electroreduction. *Phys. Chem. Chem. Phys.* **2012**, *14*, 76−81.
(21) Roberts, F. S.; Kuhl, K. P.; Nilsson, A. High Selectivity for Ethylene from Carbon Dioxide Reduction over Copper Nanocube Electrocatalysts. *Angew. Chem., Int. Ed.* **2015**, *54*, 5179−5182.
(22) Mistry, H.; Varela, A. S.; Bonifacio, C. S.; Zegkinoglou, I.; Sinev, I.; Choi, Y.-W.; Kisslinger, K.; Stach, E. A.; Yang, J. C.; Strasser, P.; et al. Highly Selective Plasma-Activated Copper Catalysts for Carbon Dioxide Reduction To Ethylene. *Nat. Commun.* **2016**, *7*, 12123.
(23) Kim, D.; Lee, S.; Ocon, J. D.; Jeong, B.; Lee, J. K.; Lee, J. Insights into an Autonomously Formed Oxygen-Evacuated Cu_2O Electrode for the Selective Production of C_2H_4 from CO_2. *Phys. Chem. Chem. Phys.* **2015**, *17*, 824−830.
(24) Ren, D.; Deng, Y.; Handoko, A. D.; Chen, C. S.; Malkhandi, S.; Yeo, B. S. Selective Electrochemical Reduction of Carbon Dioxide to Ethylene and Ethanol on Copper(I) Oxide Catalysts. *ACS Catal.* **2015**, *5*, 2814−2821.
(25) Ma, S.; Sadakiyo, M.; Luo, R.; Heima, M.; Yamauchi, M.; Kenis, P. J. A. One-Step Electrosynthesis of Ethylene and Ethanol from CO_2 in an Alkaline Electrolyzer. *J. Power Sources* **2016**, *301*, 219−228.
(26) Reller, C.; Krause, R.; Volkova, E.; Schmid, B.; Neubauer, S.; Rucki, A.; Schuster, M.; Schmid, G. Selective Electroreduction of CO_2 toward Ethylene on Nano Dendritic Copper Catalysts at High Current Density. *Adv. Energy Mater.* **2017**, *7*, 1602114.
(27) Feng, X.; Jiang, K.; Fan, S.; Kanan, M. W. A Direct Grain-Boundary-Activity Correlation for CO Electroreduction on Cu Nanoparticles. *ACS Cent. Sci.* **2016**, *2*, 169−174.
(28) Verdaguer-Casadevall, A.; Li, C. W.; Johansson, T. P.; Scott, S. B.; McKeown, J. T.; Kumar, M.; Stephens, I. E. L.; Kanan, M. W.; Chorkendorff, I. Probing the Active Surface Sites for CO Reduction on Oxide-Derived Copper Electrocatalysts. *J. Am. Chem. Soc.* **2015**, *137*, 9808−9811.
(29) Hori, Y.; Takahashi, I.; Koga, O.; Hoshi, N. Electrochemical Reduction of Carbon Dioxide at Various Series of Copper Single Crystal Electrodes. *J. Mol. Catal. A: Chem.* **2003**, *199*, 39−47.
(30) Kim, Y. G.; Javier, A.; Baricuatro, J. H.; Soriaga, M. P. Regulating the Product Distribution of CO Reduction by the Atomic-Level Structural Modification of the Cu Electrode Surface. *Electrocatalysis* **2016**, *7*, 391−399.
(31) Hahn, C.; Hatsukade, T.; Kim, Y. G.; Vailionis, A.; Baricuatro, J. H.; Higgins, D. C.; Nitopi, S. A.; Soriaga, M. P.; Jaramillo, T. F. Engineering Cu surfaces for the electrocatalytic conversion of CO_2: Controlling selectivity toward oxygenates and hydrocarbons. *Proc. Natl. Acad. Sci. U. S. A.* **2017**, *114*, 5918−5923.
(32) Ledezma-Yanez, I.; Gallent, E. P.; Koper, M. T. M.; Calle-Vallejo, F. Structure-Sensitive Electroreduction of Acetaldehyde to Ethanol on Copper and its Mechanistic Implications for CO and CO_2 reduction. *Catal. Today* **2016**, *262*, 90−94.
(33) Bertheussen, E.; Verdaguer-Casadevall, A.; Ravasio, D.; Montoya, J. H.; Trimarco, D. B.; Roy, C.; Meier, S.; Wendland, J.; Nørskov, J. K.; Stephens, I. E. L.; et al. Acetaldehyde as an Intermediate in the Electroreduction of Carbon Monoxide to Ethanol on Oxide-Derived Copper. *Angew. Chem., Int. Ed.* **2016**, *55*, 1450−1454.
(34) Heinen, M.; Jusys, Z.; Behm, R. J. Ethanol, Acetaldehyde and Acetic Acid Adsorption/Electrooxidation on a Pt Thin Film Electrode: An in Situ ATR-FTIRS Flow-Cell Study. *J. Phys. Chem. C* **2010**, *114*, 9850−9864.
(35) Hall, A. S.; Yoon, Y.; Wuttig, A.; Surendranath, Y. Mesostructure-Induced Selectivity in CO_2 Reduction Catalysis. *J. Am. Chem. Soc.* **2015**, *137*, 14834−14837.
(36) Hori, Y.; Murata, A.; Takahashi, R.; Suzuki, S. Electroreduction of CO to CH_4 and C_2H_4 at a Copper Electrode in Aqueous Solutions at Ambient Temperature and Pressure. *J. Am. Chem. Soc.* **1987**, *109*, 5022−5023.
(37) Bertheussen, E.; Abghoui, Y.; Jovanov, Z. P.; Varela, A. S.; Stephens, I. E. L.; Chorkendorff, I. Quantification of Liquid Products from the Electroreduction of CO_2 and CO using Static Headspace-Gas Chromatography and Nuclear Magnetic Resonance Spectroscopy. *Catal. Today* **2017**, *288*, 54−62.
(38) Kuhl, K. P.; Cave, E. R.; Abram, D. N.; Jaramillo, T. F. New Insights into the Electrochemical Reduction of Carbon Dioxide on Metallic Copper Surfaces. *Energy Environ. Sci.* **2012**, *5*, 7050−7059.
(39) Kim, Y. G.; Javier, A.; Baricuatro, J. H.; Torelli, D. A.; Cummins, K. D.; Tsang, C. F.; Hemminger, J. C.; Soriaga, M. P. Surface Reconstruction of Pure-Cu Single-Crystal Electrodes under CO-Reduction Potentials in Alkaline Solutions: A Study by Seriatim ECSTM-DEMS. *J. Electroanal. Chem.* **2016**, *780*, 290−295.
(40) Schouten, K. J. P.; Qin, Z.; Pérez Gallent, E.; Koper, M. T. M. Two Pathways for the Formation of Ethylene in CO Reduction on Single-Crystal Copper Electrodes. *J. Am. Chem. Soc.* **2012**, *134*, 9864−9867.
(41) Schouten, K. J. P.; Gallent, E. P.; Koper, M. T. M. Structure Sensitivity of the Electrochemical Reduction of Carbon Monoxide on Copper Single Crystals. *ACS Catal.* **2013**, *3*, 1292−1295.

DOI: 10.1021/acsenergylett.8b00092
ACS Energy Lett. 2018, 3, 634−640

(42) Roberts, F. S.; Kuhl, K. P.; Nilsson, A. Electroreduction of Carbon Monoxide over a Copper Nanocube Catalyst: Surface Structure and pH Dependence on Selectivity. *ChemCatChem* **2016**, *8*, 1119−1124.
(43) Le Duff, C. S.; Lawrence, M. J.; Rodriguez, P. *Angew. Chem., Int. Ed.* **2017**, *56*, 12919−12924.
(44) Mayrhofer, K. J. J.; Crampton, A. S.; Wiberg, G. K. H.; Arenz, M. Analysis of the Impact of Individual Glass Constituents on Electrocatalysis on Pt Electrodes in Alkaline Solution. *J. Electrochem. Soc.* **2008**, *155*, P78−P81.
(45) Mayrhofer, K. J. J.; Wiberg, G. K. H.; Arenz, M. Impact of Glass Corrosion on the Electrocatalysis on Pt Electrodes in Alkaline Electrolyte. *J. Electrochem. Soc.* **2008**, *155*, P1−P5.
(46) Hori, Y.; Konishi, H.; Futamura, T.; Murata, A.; Koga, O.; Sakurai, H.; Oguma, K. Deactivation of Copper Electrode in Electrochemical Reduction of CO_2. *Electrochim. Acta* **2005**, *50*, 5354−5369.
(47) Wuttig, A.; Surendranath, Y. Impurity Ion Complexation Enhances Carbon Dioxide Reduction Catalysis. *ACS Catal.* **2015**, *5*, 4479−4484.
(48) Subbaraman, R.; Danilovic, N.; Lopes, P. P.; Tripkovic, D.; Strmcnik, D.; Stamenkovic, V. R.; Markovic, N. M. Origin of Anomalous Activities for Electrocatalysts in Alkaline Electrolytes. *J. Phys. Chem. C* **2012**, *116*, 22231−22237.
(49) Kim, Y. G.; Baricuatro, J. H.; Javier, A.; Gregoire, J. M.; Soriaga, M. P. The Evolution of the Polycrystalline Copper Surface, First to Cu(111) and Then to Cu(100), at a Fixed CO_2RR Potential: A Study by Operando EC-STM. *Langmuir* **2014**, *30*, 15053−15056.

DOI: 10.1021/acsenergylett.8b00092
ACS Energy Lett. 2018, 3, 634−640

ACS Energy LETTERS

Cite This: ACS Energy Lett. 2019, 4, 803−804

http://pubs.acs.org/journal/aelccp

ENERGY EXPRESS

Absence of Oxidized Phases in Cu under CO Reduction Conditions

Soren B. Scott,[†] Thomas V. Hogg,[†] Alan T. Landers,[‡,¶] Thomas Maagaard,[†] Erlend Bertheussen,[†] John C. Lin,[‡,§] Ryan C. Davis,[∥] Jeffrey W. Beeman,[⊥,#] Drew Higgins,[‡,§] Walter S. Drisdell,[⊥,#] Christopher Hahn,[‡,§] Apurva Mehta,[∥] Brian Seger,[†] Thomas F. Jaramillo,*[,‡,§] and Ib Chorkendorff*[,†]

[†]Section for Surface Physics and Catalysis, Department of Physics, Technical University of Denmark, 2800 Kgs Lyngby, Denmark
[‡]Center for Interface Science and Catalysis & [∥]Stanford Synchrotron Radiation Lightsource, SLAC National Accelerator Laboratory, Menlo Park, California 94025, United States
[¶]Department of Chemistry & [§]Department of Chemical Engineering, Stanford University, Stanford, California 94305, United States
[⊥]Joint Center for Artifcial Photosynthesis & [#]Chemical Sciences Division, Lawrence Berkeley National Laboratory, Berkeley, California 94720, United States

Supporting Information

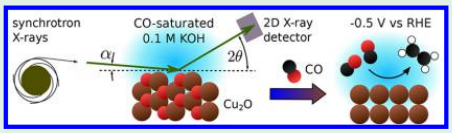

ABSTRACT: By live-monitoring Cu and Cu_2O Bragg peaks from the surface of a polycrystalline Cu electrode while scanning from open-circuit potential to CO reduction potentials, we show that the near-surface region is fully converted to the metallic phase at approximately +0.3 V vs RHE.

Copper can catalyze the electrochemical reduction of CO_2 and CO to multicarbon fuels with significant activity and Faradaic efficiency,[1,2] and copper-based gas-diffusion electrodes for reduction of CO_2 and CO to ethylene in alkaline electrolyte are approaching technological viability.[3,4] However, uncertainty about the atomic structure of the electrode surface and near-surface region under reaction conditions remains a challenge to the development of more active and selective electrodes materials.

Importantly, the presence of oxygen is a matter of debate. Despite the high equilibrium potentials for reduction of bulk oxidized phases of copper (U°_{RHE} > 0.4 V; see Table S1), several studies have reported signs that oxygen is present near the surface of copper electrodes under reaction conditions (U°_{RHE} < 0 V),[5,6] and DFT calculations have indicated that subsurface oxygen may promote CO_2 and CO reduction activity.[6,7] Other experiments and calculations have indicated that subsurface oxygen is not stable under the cathodic reaction conditions,[8−10] and recent comparisons have shown that the intrinsic CO and CO_2 reduction activity on copper-based electrodes does not depend on the initial oxidation state.[2,11]

We used in situ grazing incidence X-ray diffraction (GIXRD) with synchrotron radiation to probe the structure of a polycrystalline copper thin film under CO reduction conditions in 0.1 M KOH (pH ≈ 13) using a three-electrode setup with a flow cell and techniques described in the SI and in detail elsewhere.[14] By varying the incident angle (α), GIXRD diffractograms were taken at probe depths of ∼2.5 nm (α = 0.15°) and ∼20 nm (α = 0.20°). Product quantification has been described elsewhere for polycrystalline copper under the same CO reduction conditions.[2]

Figure 1a shows typical GIXRD diffractograms in CO-saturated electrolyte, taken at the surface-sensitive incident angle of α = 0.15°, before (+0.65 V vs RHE) and after (−0.4 V vs RHE) reduction. The first potential is near the measured open-circuit potential (OCP, typically ∼0.7 V vs RHE; see Figure S1), and CO reduction is significant at the latter potential.[2] The broad $Cu_2O(111)$ peak centered at 2θ = 16.9° in the prereduction diffractogram, attributed to the native oxide formed while the sample is exposed to air and/or at OCP, disappears in the postreduction diffractogram. That peak's large width indicates that the oxide phase is less crystalline than the metallic phase (∼5 nm crystallites compared to ∼15 nm; see Figure S2). No peaks for other oxidized Cu phases such as CuO or $Cu(OH)_2$ were observed. Results are similar in Ar-saturated electrolyte (Figure S3). The high pH likely plays a role in the formation of long-range order in the Cu_2O phase at OCP, as Cu_2O diffraction peaks were not observed at OCP at lower pH.[14]

Figure 1b shows the live reduction of a fresh sample in Ar-saturated electrolyte (see Figure S4 for CO). The $Cu_2O(111)$ peak disappears and the Cu(111) peak becomes more intense at approximately t = 40 s, when the potential is between 0.4 and 0.3 V vs RHE. The reduction of electrodes in Ar and CO are compared in Figure 1c. For both samples, the $Cu_2O(111)$ peak disappears and the Cu(111) peak grows to maximum intensity between 0.4 and 0.3 V vs RHE, just cathodic of the standard reduction potential of Cu_2O (Table S1). The abrupt increase of

Received: January 23, 2019
Accepted: February 20, 2019
Published: February 20, 2019

DOI: 10.1021/acsenergylett.9b00172
ACS Energy Lett. 2019, 4, 803−804

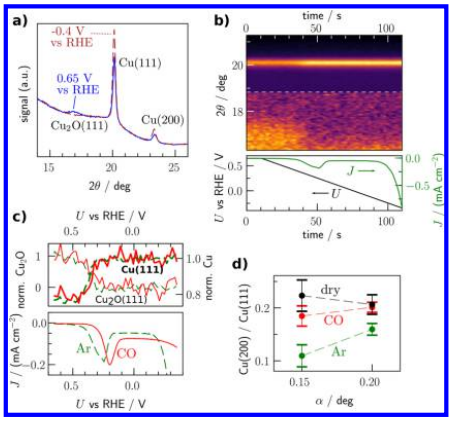

Figure 1. In situ GIXRD of polycrystalline Cu electrodes. (a) Diffractograms at incident angle α = 0.15° of a Cu sample in CO-saturated 0.1 M KOH. (b) Live monitoring of diffraction signal during reduction of a sample in Ar-saturated electrolyte. (c) Normalized integrated Cu(111) and Cu_2O(111) Bragg peaks during reduction of samples in Ar-saturated or CO-saturated electrolyte. (d) Ratio of the integrated Cu(200) and Cu(111) peaks for dry samples and reduced samples (−0.4 or −0.5 V vs RHE) in Ar- or CO-saturated electrolyte as a function of incident angle. Points and error bars represent means and standard deviations, respectively.

the Cu(111) peak to its maximum intensity by +0.3 V vs RHE rules out a significant content of any oxidized phase at more cathodic potentials within the attenuation depth of 2.5 nm (~12 monolayers), as the presense of such a phase, crystalline or amorphous, would reduce the intensity of the Cu(111) peak. The delay in the cathodic current wave with respect to the change in XRD peak intensity for the sample reduced in CO-saturated electrolyte might indicate an electrochemical reduction mechanism in which CO acts as a chemical reductant, as CO is known to reduce copper oxides in thermal catalysis.[15]

Figure 1d shows the Cu(200)/Cu(111) intensity ratio, which can be influenced by surface faceting (Figure S5). While this ratio is similar in Ar and CO prior to reduction (Figure S6), at α = 0.15° the ratio increases after reduction for samples in CO-saturated electrolyte. The ratios converge at α = 0.20°, confirming that the difference is due to a surface phenomenon. The results are consistent with the STM observation of polycrystalline Cu electrodes that reconstruct first to (111) and then to (100)[12] and provides evidence for the CO-promoted reconstruction to (100)-like surfaces. This reconstruction helps explain why polycrystalline Cu electrodes show high selectivity for CO reduction to ethylene, similar to stepped (100) surfaces.[1] Small shifts of peak centers ($\Delta 2\theta \approx -0.02°$) were also observed during the reduction (Figure S6), possibly reflecting hydrogen-induced expansion.[13]

In this study, we used in situ GIXRD to examine changes in the surface composition and morphology of polycrystalline copper under CO reduction conditions. The Cu_2O(111) diffraction peak disappears during the cathodic scan at about 0.3 V vs RHE while the Cu(111) peak simultaneously increases to its maximum intensity, with no further increase at more cathodic potentials, demonstrating that the oxide is fully reduced to the metallic phase at potentials relevant to CO reduction. Compared to other studies that also show the reduction of oxidized copper phases prior to the onset of CO or CO_2 reduction by means of in situ X-ray absorption spectroscopy[16] and Raman spectroscopy,[10] our results stand out for the high time resolution and the surface sensitivity enabled by the grazing incidence configuration. We also provide preliminary GIXRD evidence of preferential surface faceting guided by electrochemical environment, in agreement with STM studies.[12] Taken together, these results help explain why the intrinsic CO reduction activity of polycrystalline copper-based electrodes is largely invariant with the structure or oxidation state of the precursor.[2] Surface roughening caused by these faceting changes and undercoordinated sites present during the reconstruction may also contribute to copper's CO reduction activity.

■ ASSOCIATED CONTENT

Supporting Information

The Supporting Information is available free of charge on the ACS Publications website at DOI: 10.1021/acsenergylett.9b00172.

Experimental details and additional data (PDF)

■ AUTHOR INFORMATION

Corresponding Authors

*E-mail: jaramillo@stanford.edu.

*E-mail: ibchork@fysik.dtu.dk.

Notes

The authors declare no competing financial interest.

■ ACKNOWLEDGMENTS

The Center for Surface Physics and Catalysis is funded by the Villum Foundation V-SUSTAIN Grant 9455. Part of this work was performed by the Joint Center for Artificial Photosynthesis, a DOE Energy Innovation Hub, supported through the Office of Science of the U.S. Department of Energy (DOE), under Award No. DE-SC0004993. Part of this work was performed at the Stanford Nano Shared Facilities and the Stanford Nanofabrication Facility, supported by the National Science Foundation under Award ECCS-1542152. X-ray data were collected at Stanford Synchrotron Radiation Lightsource, SLAC, which is supported by the DOE Office of Basic Energy Sciences under Contract No. DE-AC02-76SF00515. S.B.S. acknowledges the Danish Ministry for Higher Education and Science for an EliteForsk travel grant.

■ REFERENCES

(1) Hori, Y. In *Modern Aspects of Electrochemistry*; 2008; Vol. *42*, pp 89−189. .

(2) Bertheussen, E.; et al. *ACS Energy Lett.* **2018**, *3* (3), 634.

(3) Han, L.; et al. *ACS Energy Lett.* **2018**, *3* (4), 855−860.

(4) Dinh, C.-T.; et al. *Science* **2018**, *360* (6390), 783.

(5) Mistry, H.; et al. *Nat. Commun.* **2016**, *7*, 12123.

(6) Eilert, A.; et al. *J. Phys. Chem. Lett.* **2017**, *8* (1), 285.

(7) Favaro, M; et al. *Proc. Natl. Acad. Sci. U. S. A.* **2017**, *114* (26), 6706.

(8) Lum, Y.; et al. *Angew. Chem., Int. Ed.* **2018**, *57* (2), 551.

(9) Garza, A. J. *J. Phys. Chem. Lett.* **2018**, *9* (3), 601.

(10) Mandal, L.; et al. *ACS Appl. Mater. Interfaces* **2018**, *10* (10), 8574.

(11) Clark, E. L.; et al. *ACS Catal.* **2018**, *8* (7), 6560.

(12) Kim, Y.-G.; et al. *J. Electroanal. Chem.* **2016**, *780* (1), 290.

(13) Huynh, T. M. T.; et al. *ChemElectroChem* **2014**, *1* (8), 1271.

(14) Farmand, M. *Phys. Chem. Chem. Phys.* 2019, in press; DOI: 10.1039/C8CP07423B.

(15) Goldstein, E. A.; et al. *Proc. Combust. Inst.* **2011**, *33* (2), 2803.

(16) Eilert, A.; et al. *J. Phys. Chem. Lett.* **2016**, *7* (8), 1466.

DOI: 10.1021/acsenergylett.9b00172
ACS Energy Lett. 2019, 4, 803−804

Supporting Information for: Absence of Oxidized Phases in Cu under CO Reduction Conditions

Soren B. Scott[1], Thomas V. Hogg[1], Alan T. Landers[2,3], Thomas Maagaard[1], Erlend Bertheussen[1], John C. Lin[2,4], Ryan C. Davis[5], Jeffrey W. Beeman[6,7], Drew Higgins[2,4], Walter S. Drisdell[6,7], Christopher Hahn[2,4], Apurva Mehta[5], Brian Seger[1], Thomas F. Jaramillo[2,4,*], and Ib Chorkendorff[1,**]

[1]SurfCat Section for Surface Physics and Catalysis, Department of Physics, Technical University of Denmark, 2800 Kgs Lyngby, Denmark
[2]SUNCAT Center for Interface Science and Catalysis, SLAC National Accelerator Laboratory, Menlo Park, CA 94025, USA
[3]Department of Chemistry, Stanford University, Stanford, CA 94305, USA
[4]Department of Chemical Engineering, Stanford University, Stanford, CA 94305, USA
[5]Stanford Synchrotron Radiation Lightsource, SLAC National Accelerator Laboratory, Menlo Park, CA 94025, USA
[6]Joint Center for Artifcial Photosynthesis, Lawrence Berkeley National Laboratory, Berkeley, CA 94720, USA
[7]Chemical Sciences Division, Lawrence Berkeley National Laboratory, Berkeley, CA 94720, USA
[*]jaramillo@stanford.edu
[**]ibchork@fysik.dtu.dk

February 18, 2019

Contents

1 Standard potentials and Experimental details

Oxide reduction potentials

Half-reaction	U°_{RHE} / V
$CuO + 2\,(H^+ + e^-) \longrightarrow Cu + H_2O$	0.56
$Cu(OH)_2 + 2\,(H^+ + e^-) \longrightarrow 2\,Cu + 2\,H_2O$	0.53
$Cu_2O + 2\,(H^+ + e^-) \longrightarrow 2\,Cu + H_2O$	0.46
$2\,CO + 6\,(H^+ + e^-) \longrightarrow CH_3CHO_{(aq)} + H_2O$	0.19
$2\,CO + 8\,(H^+ + e^-) \longrightarrow CH_3CH_2OH_{(aq)} + H_2O$	0.19
$2\,CO + 8\,(H^+ + e^-) \longrightarrow C_2H_{4(g)} + 2\,H_2O$	0.17

Table 1: Standard potentials for select half-reactions, calculated with thermochemistry data from NIST[1] and the Langes Handbook of Chemistry[2]

Standard reduction potentials for reduction of oxidized copper phases are shown together with standard reduction potentials for conversion of CO to important products in Table 1. The CO reduction potentials are all significantly more cathodic than those for the formation of metallic copper from oxidized precursors. Operating potentials for CO and CO_2 reduction are typically much more cathodic, e.g., -0.5 V vs RHE.

Setup

Figure S1a and b are schematic diagrams of the setup, and Figure S1c is a photograph of the setup.

Samples were 50 nm polycrystalline films deposited by electron-beam evaporation on a 3 mm by 10 mm degenerately doped Si(100) substrate after deposition of 3 nm Cr. The 3 nm Cr layer functions as a sticking layer and prevents the epitaxial growth of Cu on Si(100) otherwise observed[3]. Samples were prepared 1-2 weeks before use, during which time they were exposed to air. The samples were incorporated into custom-designed flow cells for *in-situ* X-ray measurements, described in more detail elsewhere[4], which enable high electrolyte flow rate while limiting the electrolyte layer to a 200 μm - tall channel bound above by a Polyimide (Kapton) window and below by the sample (working electrode). The counter electrodes consisted of two gold or platinum wires parallel to the working electrode. A Ag/AgCl reference electrode was connected to the cell via a Lugin capillary. Electrolyte flowed at 15 ml/min in a loop containing: (1) the flow cell, (2) an auxiliary cell for gas sparging, (3) an auxiliary cell containing Chelex gel to remove metal impurities[5] and a Ti mesh to hold the Chelex in place, and (4) an HPLC pump. The auxiliary cells were made from polycarbonate and were filled nearly to the top with electrolyte. The high electrolyte flow rate and the chelex bed are intended to prevent the redeposition on the working electrode of any material dissolved from the counter electrode.

The electrolyte was 0.1 M KOH made from TraceSELECT KOH (≥99.995 %) from Honeywell Fluka and millipore H_2O. The reference electrode was calibrated with respect to the reversible hydrogen electrode (RHE) by immersing a platinum working electrode in the same electrolyte, saturating the electrolyte with H_2, cycling the potential of the platinum electrode to clean its surface, and then measuring its open-circuit potential (OCP) against the reference electrode. Ar and CO were level 5.0 purity from Airgas and Matheson, respectively. The gases were bubbled at 20-40 ml/min through a humidifier cell containing electrolyte before reaching the sparging cell. A known problem when working with CO is that it forms volatile nickel carbonyls over time when sitting in stainless steel gas lines[6]. To avoid introducing these into our electrolyte, we flowed the CO for 30 minutes to exhaust before beginning to bubble it through the humidifier and sparging cells.

GIXRD was carried out at SSRL beamline 2-1, equipped with a Pilatus100K-S 2D X-ray detector. The photon energy was 17 keV. A BioLogic SP-300 potentiostat was used to control the working electrode potential. X-ray and electrochemical data acquisition were synchronized using electronic triggers. By varying the incident angle (α), GIXRD diffractograms were taken at probe depths of ≈2.5 nm ($\alpha = 0.15°$) and ≈20 nm ($\alpha = 0.20°$)[7]. Since the exit angle is much larger than the incident angle, the probe depth is approximately equal to the attenuation length, which is calculated for a single passage of x-rays through the material.

Conventional 1-D diffractograms were calculated from the 2D images by binning detector pixels according to 2θ and dividing by the incident beam intensity. Linear backgrounds were subtracted when integrating peaks, and a Gaussian fit was used to calculate peak centers and widths. The 2θ values were corrected for refraction effects. All data analysis was done with the homemade `EC_Xray` python package (see Section 7).

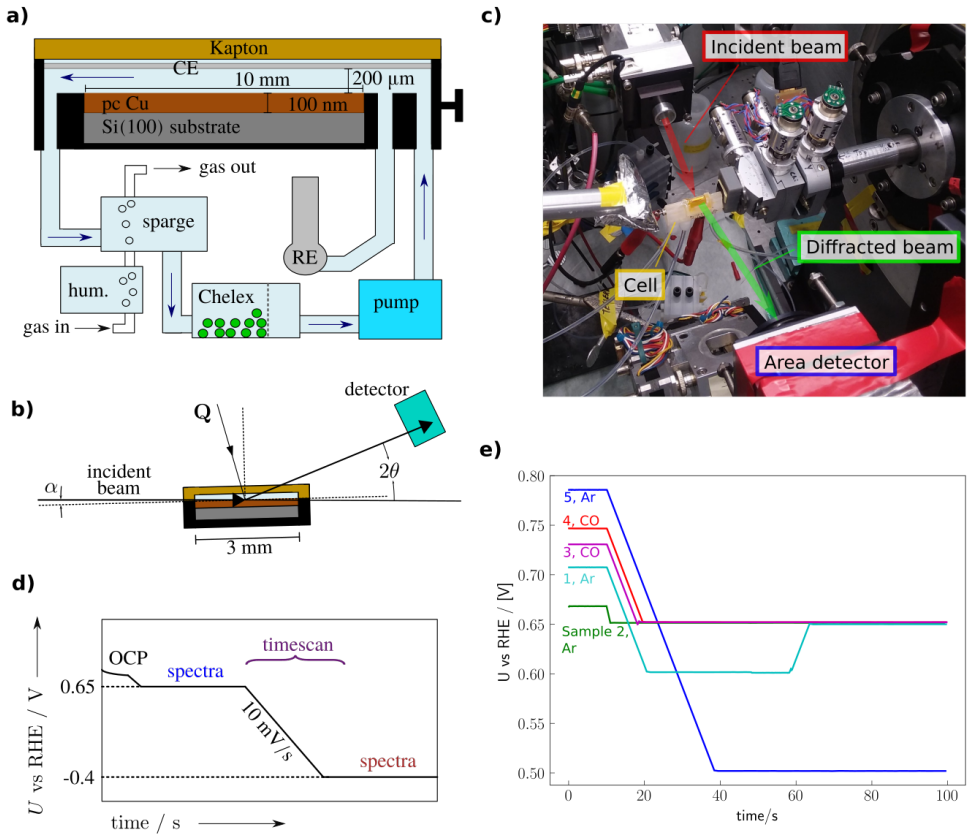

Figure S1: **Experimental setup and procedure.** a) Schematic diagram of the cell and flow system. b) Grazing-incidence x-ray diffraction geometry. c) Photograph of setup. d) Conceptual diagram of experimental procedure. e) Actual potential profile starting OCP and going to the pre-reduction potential where the first set of in-situ diffractograms were taken.

Experimental procedure and samples

Figure S1d is a diagram of the experimental procedure. A fresh sample in a new flow cell was used each time. Ar- or CO- saturated electrolyte was introduced after the dry sample was aligned and GIXRD diffractograms of the dry sample were collected. As a well-defined pre-reduction condition, the samples were held at a constant potential, typically 0.65 V vs RHE, which was slightly cathodic of the measured open-circuit potential (OCP) between 0.65 and 0.8 V vs RHE. The OCV (potential at t=0) and pre-reduction potential (potential at t=100 s) for each of the five samples studied are shown in Figure S1e.

The potential was then swept at 10 mV/s to -0.4 or -0.5 V vs RHE, potentials relevant for CO reduction[8], before taking additional GIXRD diffractograms. Employing an area detector provides the unique advantage that multiple diffraction peaks can be monitored simultaneously. With the detector centered at $2\theta = 18.5°$, we were able to monitor both the Cu(111) peak (Bragg reflection at $2\theta = 20.1°$) and the Cu_2O(111) peak ($2\theta = 16.9°$) as a function of time while the potential was scanned at 10 mV/s from 0.65 to -0.4 or -0.5 V vs RHE, thus capturing the reduction of the native oxide in real time.

Measurements from the five samples are used at various points in the main-text. Here is an overview.

- Sample 3 (CO) used in main-text Figure 1a
- Sample 2 (Ar) used in main-text Figure 1b
- Samples 2 (Ar) and 4 (CO) used in main-text Figure 1c
- All five samples used for main-text Figure 1d (mean and standard deviations are from five diffractograms for dry, three for Ar, and two for CO).

2 Crystallite size of Cu and Cu_2O: Peak fitting

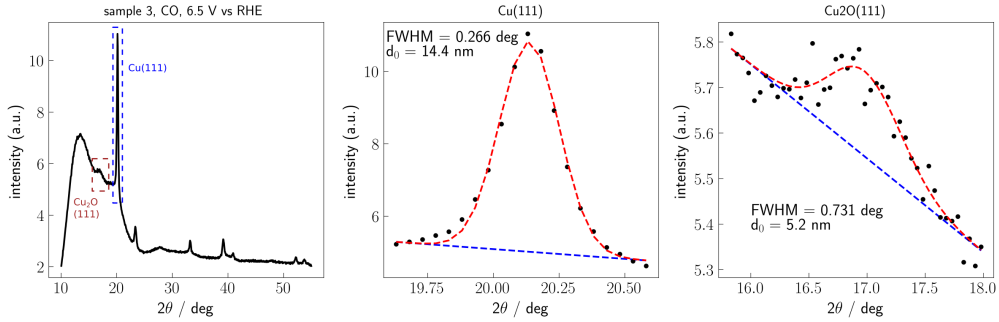

Figure S2: Background subtraction and peak fitting of typical spectrum, incident angle of 0.15°.

Figure S2 shows examples of backgrounds (blue) and Gaussian peak fits (red) for the $Cu_2O(111)$ and Cu(111) peaks in a GIXRD spectrum. The spacing of the data points is determined by the bin-size when adding up the number of counts in each of the 2D detectors pixels, as implemented in the `Pilatus` class of the `EC_Xray` python package (available at http://github.com/ScottSoren).

A linear background was calculated using three endpoints on either side of the 2θ interval including the peak. All peak integrals were calculated by trapazoidal integration of the difference between the measured datapoints and the background ($I - I_{bg}$).

For peak centers and widths, the data points, minus this background, were fit by finding the values of h, θ_0, and σ minimizing the square error of Equation 1.

$$I - I_{bg} = h \exp\left(-\frac{(2\theta - 2\theta_0)^2}{2\sigma^2}\right), \tag{1}$$

where

$$h = \text{height} \tag{2}$$
$$2\theta_0 = \text{center, and} \tag{3}$$
$$\sigma = \text{width}. \tag{4}$$

The python function `scipy.curvefit` was used for the optimization. The implementation is in the `Peak` class of the `EC_Xray` python package.

Scherrer's Equation,

$$d_0 = \frac{\kappa\lambda}{\text{FWHM} \cdot \cos(\theta)}, \tag{5}$$

can be used to calculate characteristic crystallite size (d_0) from the peak broadness, measured as it's full width at half maximum (FWHM), in radians. κ, the 'shape factor', is taken to be 0.9. FWHM for a Gaussian peak is related to the standard deviation σ by

$$\text{FWHM} = 2\sqrt{2\log(2)}\sigma. \tag{6}$$

The FWHM for the fitted Gaussian peaks in Figure S2 are 0.262° and 0.855°, respectively, for the Cu(111) and $Cu_2O(111)$ peaks. This corresponds, by the Scherrer equation, to characteristic crystallite sizes of 14.5 and 4.5 nm, respectively. Thus, both the metal and oxide phases on the surface at open-circuit potential are crystalline, though the crystallites are smaller in the oxide phase.

3 Grazing incidence x-ray diffractograms for all samples

Figure S3 shows the XRD spectra, when available, at $\alpha = 0.15°$ (attenuation length ≈2.5 nm) and at $\alpha = 0.20°$ (attenuation length ≈20 nm), for each sample as-deposited in air (black), in electrolyte prior to reduction (blue), and in electrolyte after reduction (brown, dotted). Missing scans were skipped or lost due to experimental mistakes. The very broad and asymmetrical peak centered around $2\theta = 13°$ is due to diffraction by the electrolyte. Other broad background features, including those centered around $2\theta = 27°$ and 38° are attributed to the substrate. The locations of the fcc copper peaks are indicated in the top x-axis. This study focuses on the Cu_2O(111), Cu(111), and Cu(100) peaks. The centers of these peaks, calculated using the respective bulk fcc lattice constants and Braggs equation for an X-ray energy of 17 keV, are at 2θ=16.9°, 20.15°, and 22.3°, respectively. The inset to each plot shows a zoom-in on this region, with these calculated peak locations shown by vertical lines (blue line for Cu2O and brown dotted lines for Cu).

Samples 1, 2, and 5 were reduced in Ar-saturated electrolyte, whereas samples 3 and 4 were reduced in CO-saturated electrolyte

These spectra show a great amount of variability in background size and shape, and in peak intensity. For this reason, we do not use the absolute intensity of the spectra for anything. We instead focus on peak ratios, and on peak changes observed in-situ.

The Cu2O peak at $2\theta = 16.9°$ is observed to varying degrees in the pre-reduction spectra, and is gone in all of the post-reduction spectra. This may indicate that the crystallinity or thickness of the native oxide layer depends on the time spent at OCP.

Sample 2 shows a broad peak at 2θ=17.8°. This matches the calculated 2θ value for Au(111) of 17.82°, and the peak is attributed to Au dissolved from the counter electrode deposited onto the working electrode surface at cathodic potential. There is no sign of this peak during the timescan (Figure S4), indicating that most of the deposition occurred over time at -0.5 V vs RHE. The electrolyte was completely exchanged for fresh electrolyte after this observation, and Au was not observed on subsequent samples.

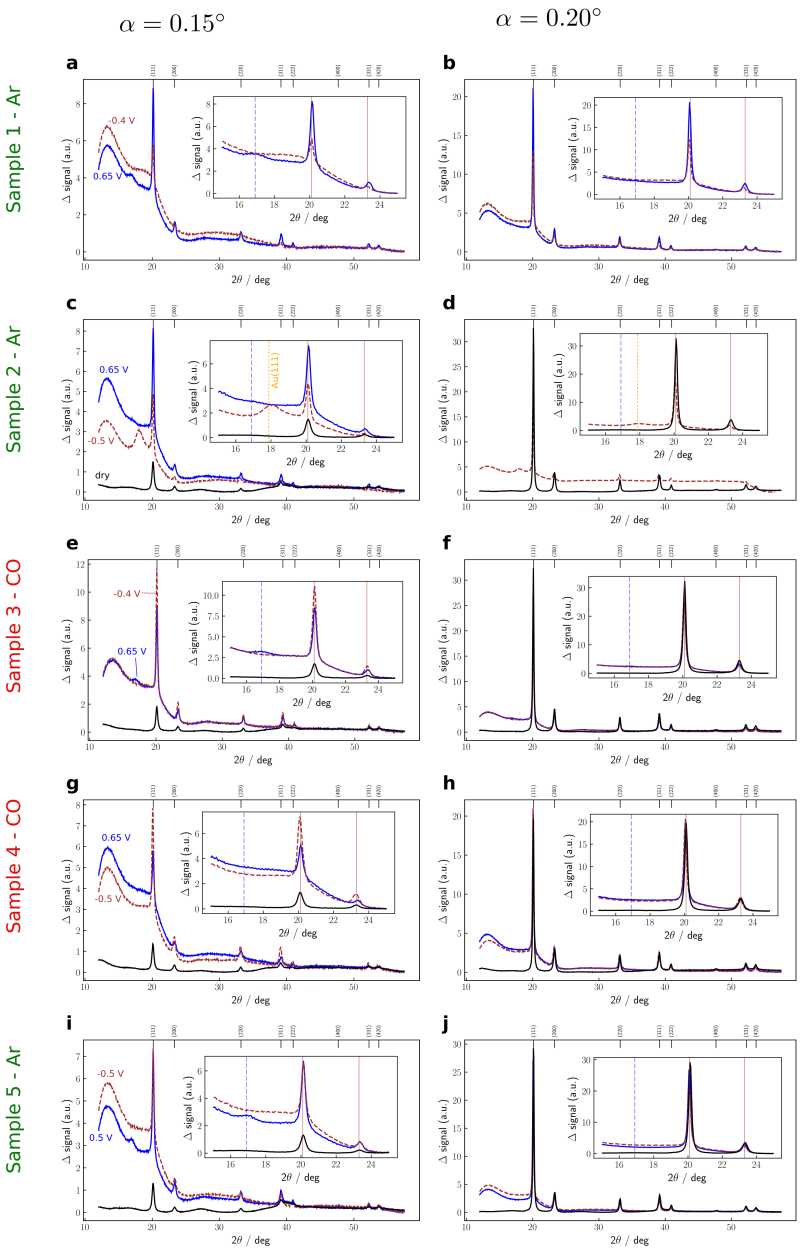

Figure S3: **Diffractograms.** Dry (black), pre-reduction (blue), and post-reduction (red) grazing-incidence diffractograms for all samples. The inset shows a zoom-in on the region of interest, including vertical lines for the calculated centers of the $Cu_2O(111)$, Cu(111), and Cu(200) Bragg peaks at $2\theta = 16.9°$, 20.1°, and 22.3°, respectively. The diffractograms in a, c, e, g, and i are for an incident angle of $\alpha = 0.15°$, and the corresponding diffractograms in b, d, f, h, and j are for $\alpha = 0.20°$. The sample number and gas saturating the electrolyte are indicated to the left of each row of panels.

4 Oxide reduction timescans for all samples

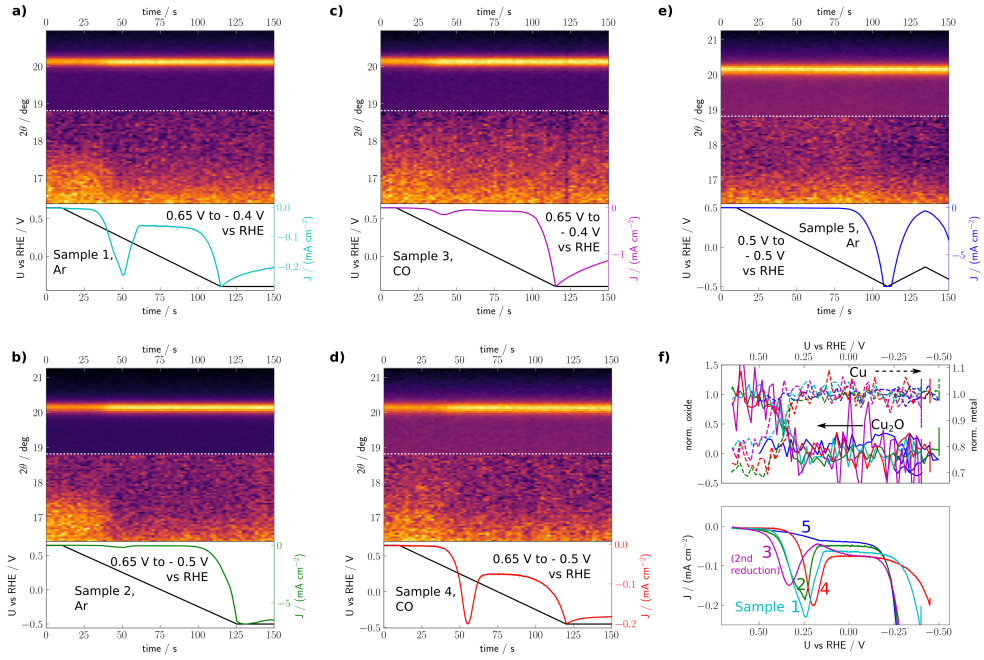

Figure S4: **Oxide reduction timescans** a-e), Diffraction signal during reduction of the native oxides. XRD data and electrochemistry data are co-plotted. The color normalization is split at 18.8° so that both diffraction peaks are visible. f), reduction waves co-plotted on potential axis. All at an incident angle of 0.15°.

A cathodic potential scan with GIXRD timescan is shown for each of the samples. For samples 1, 2, 4, and 5, it is the first sweep to a cathodic potential. For sample 3, it is the second sweep to a cathodic potential, after spectra were taken at -0.4 V vs RHE, and the potential was then increased to 0.65 V vs RHE again and held for two hours.

A single detector was used. It is only the color normalization that is split at 18.8° when plotting the result, so that both diffraction peaks are clearly visible.

In samples 1-4, the cathodic scan starts at 0.65 V vs RHE after a potential hold at 0.65 V vs RHE. This potential was chosen to stabilize the native oxide of the sample while taking pre-reduction spectra. It is slightly cathodic of the open-circuit voltage, indicating that the sample will not further oxidize significantly (though the presence of residual dissolved O_2 in the electrolyte may lead to a gradual oxidation anyway), but not cathodic enough to reduce the native oxide. In each of these scans, a $Cu_2O(111)$ peak centered at $2\theta = 16.9°$ is observed, and disappears during the reductive scan. The oxide peak is faintest for sample 3, indicating that the surface oxide formed electrochemically is thinner or and/or less crystalline than the native oxide formed in air. In each case, the metal Cu(111) peak increased by about 20% in intensity at the same time as the oxide peak disappeared.

When the potential was instead held at 0.5 V vs RHE (sample 5), the oxide peak was not observed. Neither did the metal peak increase in intensity. This is in contrast to the GIXRD spectrum in Figure S3i, where the sample shows a clear Cu_2O peak. We conclude that the oxide reduced slowly at this potential, such that the surface oxide was still present when the spectrum was taken, but disappeared before the start of the timescan.

Figure S4f shows the intensity of the oxide (solid traces) and metal peaks (dotted traces) plotted against potential for each of the samples. The electrochemical current is plotted on the same potential axis in the lower panel. These have been normalized to the final area of the metal peak and the initial area of the oxide peak, respectively. The exception is sample 5, for which the oxide peak has instead been normalized to the initial area of Sample 1's oxide peak.

Interestingly, all of the oxide peaks disappear at the same potential (within the noise), whereas the position of the cathodic electrochemical reduction wave varies. It is earliest (most anodic) in the electrochemically grown oxide (sample 3), and latest (most cathodic) for sample 4. Drift in the RHE potential of the reference electrode (either due to the pH of the electrolyte or the reference electrode itself) may play a role, but cannot explain the changing alignment of the reduction wave and the change in GIXRD peak intensity. We are rather confident in the alignment of the two datasets, since we used a TTL trigger to synchronize the potentiostat and X-ray data acquisition. The increase of the metal peak seems intermediate, varying between samples but not by as much as the electrochemical reduction wave. This may provide information on the reduction mechanism, but further studies are needed.

The current denisity at cathodic potentials varies significantly between samples. The current density of sample 1($\approx -0.2^{\mathrm{mA}}/_{\mathrm{cm}^2}$ at -0.4 V vs RHE in Ar), and sample 4 ($\approx -0.18^{\mathrm{mA}}/_{\mathrm{cm}^2}$ at -0.5 V vs RHE in CO) are consistent with current densities reported previously for polycrystalline copper electrodes in 0.1 M KOH[8]. The current density of the other samples is significantly higher. One possible explanation is redeposition of material from the counter electrode. This was in fact observed for Sample 2, for which an Au(111) Bragg peak is observed after a ≈1 hour at -0.5 V vs RHE (Figure S3) and attributed to dissolution and redeposition of material from the Au counter electrode. For Sample 3, a Platinum counter electrode was used. While no platinum is detected, even small amounts of platinum redeposition could dominate the current density due to platinums high HER activity.

The conclusions of this article the lack of oxidized Cu phases at potentials relevant for CO reduction, and the CO-promoted restructuring of the surface were consistent across samples whether or not possible CE material deposition was evidenced through heightened current density. Therefore, it does not impact the conclusions of this work. However, it shows that the dissolution and redeposition of counter electrode material is one challenge to be overcome in further developing this technique to a fully in-operando technique. A possible solution would be to have an external counter electrode, connected through an idex tube and glass frit, as was done with the reference electrode.

5 GIXRD and faceting

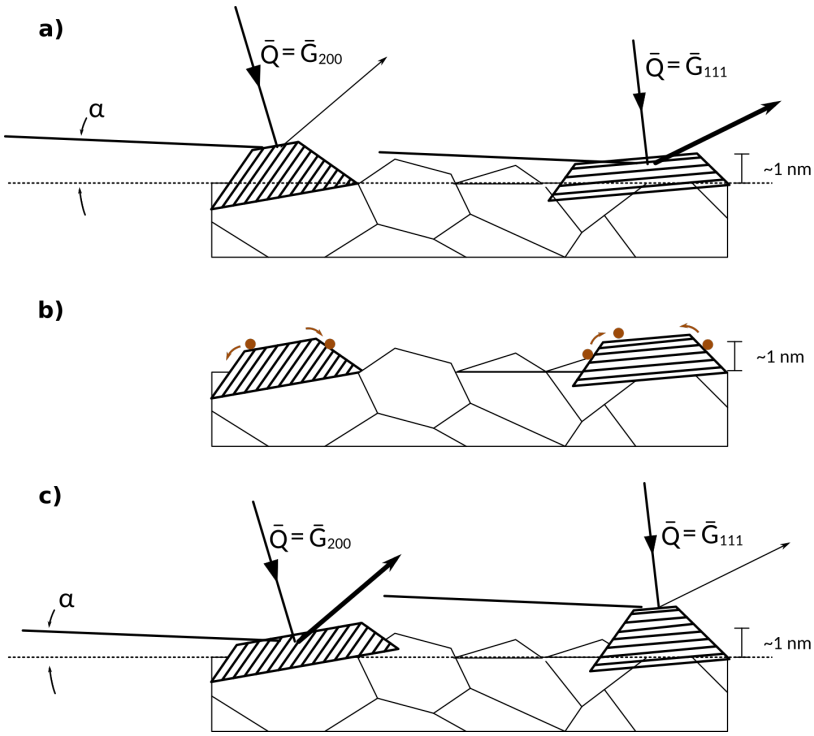

Figure S5: **GIXRD and faceting: Conceptual diagram.** Two crystallites have reciprocal lattice vectors satisfying the Laue condition for the $\mathbf{G}_{200}$ and $\mathbf{G}_{111}$ reciprocal lattice vectors, respectively. They are highlighted with lines representing the orientation of the (111) lattice planes. a) Initially, the (111) surface is preferred, causing crystallites for which the $\mathbf{G}_{111}$ is close to the macroscopic surface normal to have a large, exposed, flat surface. This includes the crystallite satisfying the Laue condition for $\mathbf{G}_{111}$, since θ_{111} is much less than 90°, leading to an intense (111) grazing-incidence diffraction peak. b) Over time, the (100) surface is preferred by the electrochemical environment, leading to atomic migration increasing the exposed (100) surface. c) This favors the exposed facets for which $\mathbf{G}_{200}$ is near the macroscopic surface normal, increasing the relative intensity of the (200) diffraction peak. All angles are exaggerated.

As shown in main-text Figure 1d, there is a change in the ratio of the areas of various peaks with electrochemical conditions. Specifically, the Cu(200)/Cu(111) ratio appears lower in electrochemical environment than for the dry samples, but this ratio grows after reduction for the samples in CO-saturated electrolyte. The ratio only differs significantly between measurements for an incident angle of $\alpha = 0.15°$, below the critical angle for total external reflection, and not at $\alpha = 0.20°$, above the critical angle.

We interpret the changing peak ratio to represent a changing ratio of surface facets on the electrode. Figure S5 shows how a changing ratio of surface facets would change the ratio of peaks as seen in GIXRD of a polycrystalline electrode at an angle below the critical angle.

We consider a local area of the polycrystalline electrodes. In order for a crystallite to produce a diffraction signal for a peak hkl, it must be oriented such that the Laue condition $\mathbf{Q} = \mathbf{G}_{hkl}$ is satisfied. In other words, the normal to the planes hkl must be in the plane defined by the incident beam and the detector, and make an angle $(\frac{\pi}{2} - \theta_{hkl})$ with the incident beam, or an angle $(\theta_{hkl} - \alpha)$ with the macroscopic surface normal. For most crystallites, this condition will not be satisfied for any diffraction planes. In the local area considered

here, the condition is satisfied by two crystallites: For the leftmost crystallite, $\mathbf{Q} = \mathbf{G}_{200}$ at a diffracted beam angle of $2\theta_{200}$, and for the rightmost crystallite, $\mathbf{Q} = \mathbf{G}_{111}$ at a diffracted beam angle of $2\theta_{111}$. These two crystallites are indicated in Figure S5 by stripes, which in both cases indicate the direction of the 111 planes.

We imagine that, initially, the 111 surface of the electrode is favored (Figure S5a). This means that the rightmost crystal, for which the 111 surface is close to the surface normal (about $\theta_{111} \approx 10^\circ$ from the surface normal), will be relatively long and flat, exposing more of the 111 surface. The leftmost crystal, for which it is instead the 100 surface that is close to the surface normal, will be short and flat. Thus, the incident x-rays will penetrate a larger portion of the crystallite on the right than on the left, and the 111 peak will be more intense in the GIXRD spectrum than the 200.

Now we imagine that a change in electrochemical environment favors the 100 surface facet. We do not imagine that crystallites rotate to favor this surface, since the dislodging of an entire crystallite would require too much energy. Instead, we imagine that atoms, if sufficiently mobile, migrate to surfaces of higher free energy (the less-favored surfaces). This increases the area of the favored surface facet, as indicated in Figure S5b.

Now, the situation is reversed. The left-most crystallite, for which the 100 surface lies near the macroscopic surface normal, has a larger exposed surface area than the right-most crystallite. Because of the small penetration depth, it also contributes a larger intensity to the total GIXRD spectrum. The 200 diffraction peak has now increased in intensity relative to the 111 diffraction peak, which is the observed effect.

This illustration depends on the assumption that, for the crystallites satisfying the Laue condition for the (hkl) diffraction, the reciprocal lattice vector $\mathbf{G}_{hkl}$ is close to the macroscopic surface normal. In other words, it depends on $(\theta_{hkl} - \alpha)$ being small. Since α is small, this means θ_{hkl} should be small. We therefore only analyze the ratio of the first two Cu diffraction peaks, 111 and 200, for which the calculated diffraction angles are $\theta_{111} = 10.1^\circ$ and $\theta_{200} = 11.7^\circ$.

Furthermore, we do not attempt to quantify the effect, as a quantitative analysis of this model is beyond the scope of the present work.

6 Peak widths, centers, and areas

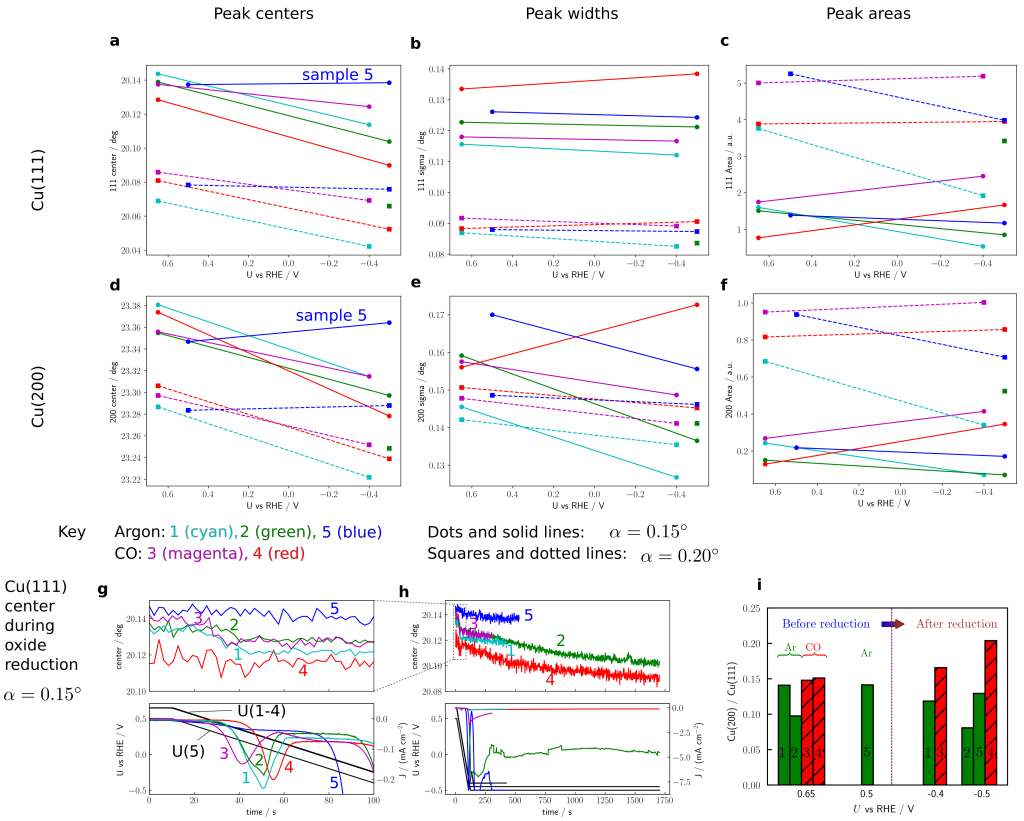

Figure S6: Cu(111) and Cu(200) areas, widths, and centers. In (a-h), sample numbers are indicated by color. In (i), sample numbers are are written on the bars to make it clear which pre-reduction ratio corresponds to which post-reduction ratio.

Figure S6a-f compares the Cu(111) (a-c) and Cu(200) (d-f) peak areas (a, d), centers (b, e) and widths (c, f) and each of the five samples at each of the two incident angles. This is in contrast to the ratio of the 200 and 111 peak areas, examined in main-text Figure 3. No significant trends stand out to us, except for the peak centers, which move towards smaller angles after reduction for all samples except for sample 5. Sample 5 differs from the other samples in that it was held at 0.5 V vs RHE rather than 0.65 V vs RHE before the initial sweep to cathodic potentials, and the native oxide gradually reduced at 0.5 V vs RHE (figure S2).

Thus, for each of the samples where the native oxide was reduced in-situ, the peaks shifted to slightly smaller angles. The shift, of $\approx 0.02°$ for the 111 peak and $\approx 0.04°$ for the 200 peak, corresponds to a lattice expansion on the order of 0.01%. It is consistent for the two incident angles, indicating that, if it is indeed a lattice expansion, it is not only the surface but extends tens of nanometers into the material. Note that the peak shift is smaller than the 2θ bin width of $0.05°$ used for spectrum calculation from the raw data, but the use of a gaussian fit makes possible location of the peak center to a higher accuracy than the spacing between spectrum points.

To figure out when this expansion takes place, we also calculated the peak centers during the timescans of the samples. Only the 111 peak was in the window monitered during the timescans. A small shift, on the

order 0.01°, half of the total change, is observed at the moment that the native oxide is reduced. For samples 2 and 4, the timescan was continued during the cathodic potential hold, revealing that the rest of the shift in peak center occurs slowly during the potential hold (Figure S6h).

We consider hydrogen intercalation in the Cu lattice to be a likely explanation. However, the change is very small, and more studies are needed to rule out e.g., drift in detector position or refraction effects.

Figure S6c and f show the integrated intensities of the Cu(111) and Cu(100) GIXRD peaks taken at an incident angle of $\alpha = 0.15°$ for samples before and after reduction. Changes in absolute peak area might represent changes in e.g., sample alignment, and so we instead focus on the relative intensities of peaks. In Figure S6i, the ratio of the Cu(200) to Cu(111) peaks before and after reduction is shown for each of the five sample tested. The Cu(200)/Cu(111) ratio increases for the samples reduced in CO, but not for the samples reduced in Ar. This indicates that Cu surfaces tend to favor (100)-like facets under CO reduction conditions.

7 `EC_Xray` python package

All of the data analysis in this article was performed using the the `EC_Xray` python package, available at https://github.com/ScottSoren/EC_Xray.

This package provides an object-oriented interface for analyzing and plotting diffraction data output by SSRL's SPEC program. It also enables smooth combination of the diffraction data with electrochemistry data output by Biologic's EC-Lab software.

Two tutorials are available at https://github.com/ScottSoren/Tutorials/tree/master/EC_Xray_tutorials. They are prepared as a Jupyter Notebooks, and also included as pdf's.

The Diffractogram tutorial shows how the `Pilatus` class (for storing and analyzing images from 2-D X-ray detectors, including transformation to spherical coordinates) and `ScanImages` class are used together to calculate, analyze, and plot 1-D diffractograms. See https://github.com/ScottSoren/Tutorials/blob/master/EC_Xray_tutorials/Diffractogram.pdf.

The Electrochemical Scan tutorial shows how electrochemistry data is imported and plotted, and how the `ScanImages` class can be used to combine the electrochemistry data with diffraction data, synchronize according to a trigger system, and plot and analyze the combined dataset. See https://github.com/ScottSoren/Tutorials/blob/master/EC_Xray_tutorials/Electrochemical_scan.pdf

References

[1] P.J. Mallard and W.G. Linstrom, editors. *NIST Chemistry WebBook, NIST Standard Reference Database Number 69*. National Institute of Standards and Technology, Gaithersburg MD, 20899.

[2] John A Dean. *Langes Handbook of Chemistry*. McGraw-Hill, Inc, fifteenth edition, 1999.

[3] Christopher Hahn, Toru Hatsukade, Youn-Geun Kim, Arturas Vailionis, Jack H. Baricuatro, Drew C. Higgins, Stephanie A. Nitopi, Manuel P. Soriaga, and Thomas F. Jaramillo. Engineering Cu surfaces for the electrocatalytic conversion of CO_2 : Controlling selectivity toward oxygenates and hydrocarbons. *Proceedings of the National Academy of Sciences*, 114(23):5918–5923, June 2017.

[4] Maryam Farmand, Alan T Landers, John Lin, Jeremy T Feaster, Jeffrey W Beeman, Yifan Ye, Ezra L Clark, Drew Higgins, Junko Yano, Ryan Davis, Apurva Mehta, Thomas Jaramillo, Christopher Hahn, and Walter S Drisdell. Electrochemical Flow Cell Enabling Operando Probing of Electrocatalyst Surfaces By X-Ray Spectroscopy and Diffraction. *Physical Chemistry Chemical Physics*, in press. DOI: 10.1039/C8CP07423B, 2019.

[5] Anna Wuttig and Yogesh Surendranath. Impurity Ion Complexation Enhances Carbon Dioxide Reduction Catalysis. *ACS Catalysis*, 5(7):4479–4484, nov 2015.

[6] J. Nerlov, S. Sckerl, J. Wambach, and I. Chorkendorff. Methanol Synthesis from CO_2, CO and H_2 over Cu(100) and Cu(100) Modified by Ni and Co. *Applied Catalysis A: General*, 191(1-2):97–109, 2000.

[7] B.L. Henke, E.M. Gullikson, and J.C. Davis. X-Ray Interactions: Photoabsorption, Scattering, Transmission, and Reflection at E = 50-30,000 eV, Z = 1-92. *Atomic Data and Nuclear Data Tables*, 54(2):181–342, jul 1993.

[8] Erlend Bertheussen, Thomas V. Hogg, Younes Abghoui, Albert K. Engstfeld, Ib Chorkendorff, and Ifan E. L. Stephens. Electroreduction of CO on Polycrystalline Copper at Low Overpotentials. *ACS Energy Letters*, 3(3):634–640, mar 2018.